

## Why All the Fury over Furin?

Essam Eldin A. Osman, Alnawaz Rehemtulla, and Nouri Neamati\*

Cite This: *J. Med. Chem.* 2022, 65, 2747–2784

Read Online

ACCESS |



Metrics &amp; More

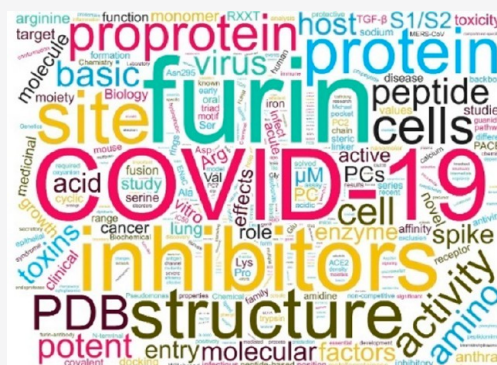


Article Recommendations



Supporting Information

**ABSTRACT:** Analysis of the SARS-CoV-2 sequence revealed a multibasic furin cleavage site at the S1/S2 boundary of the spike protein distinguishing this virus from SARS-CoV. Furin, the best-characterized member of the mammalian proprotein convertases, is an ubiquitously expressed single pass type 1 transmembrane protein. Cleavage of SARS-CoV-2 spike protein by furin promotes viral entry into lung cells. While furin knockout is embryonically lethal, its knockout in differentiated somatic cells is not, thus furin provides an exciting therapeutic target for viral pathogens including SARS-CoV-2 and bacterial infections. Several peptide-based and small-molecule inhibitors of furin have been recently reported, and select cocrystal structures have been solved, paving the way for further optimization and selection of clinical candidates. This perspective highlights furin structure, substrates, recent inhibitors, and crystal structures with emphasis on furin's role in SARS-CoV-2 infection, where the current data strongly suggest its inhibition as a promising therapeutic intervention for SARS-CoV-2.



### INTRODUCTION

Since the beginning of the new millennium, three coronaviruses (CoVs) have crossed the species barrier to cause outbreaks of deadly pneumonia in humans: severe acute respiratory syndrome coronavirus (SARS-CoV) in 2002, Middle East respiratory syndrome coronavirus (MERS-CoV) in 2012, and the novel SARS-CoV-2 in 2019.<sup>1–3</sup> These zoonotic pathogens belong to the betacoronavirus genus.<sup>3</sup> Other coronaviruses infecting humans include alphacoronaviruses HCoV-NL63 and HCoV-229E and betacoronaviruses HCoV-OC43 and HCoV-HKU1 that are endemic in humans causing upper respiratory tract infections with common cold symptoms.<sup>4</sup> SARS-CoV infected around 8000 individuals causing about 770 deaths and MERS-CoV was detected in a total of 2494 individuals claiming 858 lives.<sup>5,6</sup> On the other hand, SARS-CoV-2 has resulted in >180 million infections and >4 million deaths worldwide as of July 9, 2021.<sup>7</sup> These three highly pathogenic viruses are believed to originate in bats and were shown to be spilled over to humans via species jumping through some intermediate host.<sup>8</sup> Dromedary camels and palm civets represent the intermediate hosts for zoonotic transmission of MERS-CoV and SARS-CoV.<sup>9</sup> SARS-CoV-2 intermediate host remains unknown though some researchers hypothesize that pangolin may act as SARS-CoV-2 intermediate host.<sup>10</sup> Future zoonotic transmission events are expected to continue based on the recurrent spillovers of coronaviruses in humans coupled with the fact that bats harbor the largest number of known coronaviruses.<sup>11,12</sup> While most of COVID-19 cases are mild or even asymptomatic, an excessive immune response characterized as a “cytokine storm” may

contribute in some COVID-19 cases to the development of pulmonary edema, acute respiratory distress syndrome (ARDS), systemic inflammation, multiple organ damage, and excessive blood coagulation that may lead to life-threatening conditions in severe cases.<sup>13–16</sup> To date, there are no effective therapies against any of these coronaviruses. Several vaccines based on various technologies have recently been authorized for emergency use against COVID-19.<sup>17</sup> The current data suggest that these vaccines are very safe and efficacious. However, the effectiveness of these vaccines in patients with impaired immune systems and the degree of protection conferred are still unknown, and the protective effect of the vaccination on a global level is not expected to be achievable in the near future. Additionally, the development of variants, some of which may evade vaccine-derived immunity, is also of concern. Thus, effective antiviral drugs are still needed, and ultimately, in case of new emerging coronavirus pandemics, the availability of such treatments would constitute a powerful antiviral armory, independent of immunity. Tremendous research effort is ongoing to identify and validate potential targets that could be exploited for novel therapeutics to treat SARS-CoV-2 infection. Therapeutic targets related to viral entry into the host cells and/or its replication are among the

**Special Issue:** COVID-19**Received:** March 21, 2021**Published:** August 2, 2021

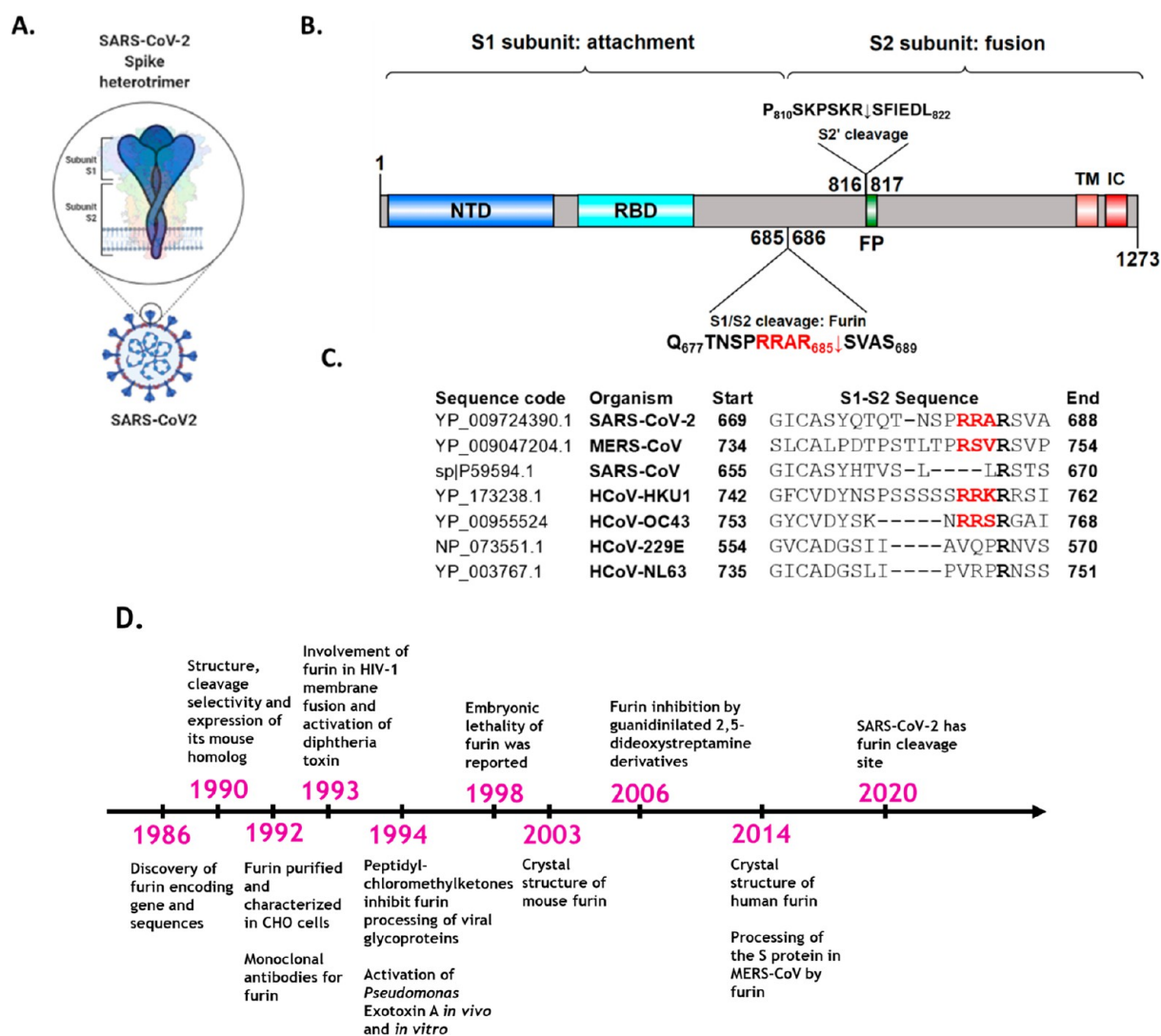


**Figure 1.** (A) Schematic diagram of SARS-CoV-2. (B) Domain structure of SARS-CoV-2 Spike protein: N-terminal domain (NTD), receptor-binding domain (RBD), fusion peptide (FP); transmembrane domain (TM); intracellular domain (IC), and S1/S2 and S2' protease cleavage sites are highlighted. (C) Alignment of SARS-CoV-2 S1/S2 furin cleavage site with other human coronaviruses. A conserved arginine residue (Arg685 in SARS-CoV-2) and the sequences of the basic furin cleavage sites are bold. (D) Timeline of furin-related discoveries.

most extensively explored strategies to develop inhibitors.<sup>18,19</sup> For entry into host cells, CoVs need to bind to cell surface receptors, subsequently enter endosomes, and eventually fuse viral and lysosomal membranes.<sup>18,20</sup> Entry of CoVs into host cells is mediated by its transmembrane spike glycoprotein (S) that forms homotrimers on the viral cell surface (Figure 1).<sup>18,21–23</sup> The S glycoprotein is comprised of two functional subunits: S1 and S2. While distinct receptor-binding domains (RBD) within the S1 subunit are used by different CoVs to recognize a variety of attachment and entry receptors in the host cells, the S2 subunit harbors the membrane fusion machinery of the viral and host cellular membranes.<sup>22</sup> The boundary between S1 and S2 subunits of the viral S glycoprotein needs to be proteolytically cleaved, and this results in what is known as the “prefusion conformation” where the cleaved subunits remain noncovalently bound.<sup>22</sup> In all CoVs, subsequent cleavage of the S glycoprotein by host proteases at a site (S2') located upstream to the fusion peptide has been proposed to result in extensive irreversible conformational changes that ultimately activate the S2 subunit for membrane fusion.<sup>18,19,21–26</sup> MERS-CoV S domain A (S<sub>A</sub>)

recognizes nonacetylated sialosides attachment receptors to promote subsequent binding of the S domain B (S<sub>B</sub>) to dipeptidyl-peptidase 4 (DDP4) as an entry receptor, whereas both SARS-CoV and SARS-CoV-2 interact with angiotensin-converting enzyme 2 (ACE2) via S<sub>B</sub> to enter host cells.<sup>18,19,23</sup> The spike protein of MERS-CoV was previously shown to be activated by a two-step sequential process: cleavage at the S1/S2 site by the host serine protease furin in infected cells that is required for subsequent surface serine protease TMPRSS2-mediated cleavage at the S2' site.<sup>27</sup> While SARS-CoV entry into the host cells does not require proteolytic cleavage by furin at S1/S2 boundary, TMPRSS2 and other host proteases (e.g., lysosomal cathepsins B/L) are among the host proteases that process its S protein probably at S2' in lung cells.<sup>28,29</sup> TMPRSS2 is a type II transmembrane serine protease that cleaves at single arginine or lysine residues, at the so-called monobasic cleavage sites.<sup>30,31</sup> This enzyme is widely expressed in the epithelial cells of the respiratory, urogenital, and gastrointestinal tracts but with no definite physiological role.<sup>31</sup> TMPRSS2-deficient mice lack a distinct phenotype suggesting functional redundancy.<sup>32</sup> TMPRSS2 was previously identified

to cleave the surface glycoprotein HA of human influenza A viruses and activate the fusion proteins of a number of other respiratory viruses, as well as human parainfluenza viruses, and CoVs, including SARS-CoV and MERS-CoV *in vitro*.<sup>24,33</sup> On the other hand, furin, the best-characterized member of the mammalian proprotein convertases, is an ubiquitously expressed multidomain calcium-dependent single pass type 1 transmembrane protein.<sup>34–36</sup> Furin can proteolytically cleave a large array of >400 substrates including bacterial toxins and viral coat proteins during their transport along the secretory pathway at multibasic motifs of the preferred consensus sequence Arg-X-Arg/Lys-Arg↓ (R-X-R/K-R↓).<sup>34–36</sup> Sequence analysis of SARS-CoV-2 revealed a furin cleavage site (FCS) in its S glycoprotein at the boundary between the S1/S2 subunits (Q<sub>677</sub>TNSPRRRAR↓SVAS<sub>689</sub>).<sup>23,25,26</sup> In addition to SARS-CoV-2 and MERS-CoV, furin cleavage sequences were found in human coronaviruses OC43 and HKU1 but not in SARS-CoV and other related group 2b betacoronaviruses (Figure 1).<sup>23,26</sup> Analysis of thousands of SARS-CoV-2 sequences derived from COVID-19 patients showed low frequencies of natural mutants that harbor deletions at the FCS suggesting selective pressure to conserve FCS for *in vivo* transmission, yet not necessarily *in vitro* depending on the characteristics of the cell line.<sup>37–39</sup> The origin of the furin cleavage site in SARS-CoV-2 is a point of active research since its closest relatives, the bat isolate RaTG13 or the pangolin coronavirus, lack this site.<sup>10,23,25,26,40</sup> Ongoing research suggests that the furin cleavage site within the spike protein of SARS-CoV-2 may provide “gain-of-function”, at least in part, for the fusion of the virus and host cell membranes upon entry into the host cell (infectivity) compared to other lineage B human betacoronaviruses.<sup>25,26,41</sup> Furin cleavage at the S1/S2 boundary appears critical to expose the RBD within the spike, facilitating its binding to ACE2 and the secondary cleavage of the S2' site, facilitating membrane fusion. Similar to MERS-CoV, precleavage by furin at the S1/S2 site in SARS-CoV-2 was shown to be mandatory for TMPRSS2 subsequent cleavage, which in turn is essential for viral entry into lung cells.<sup>26,37,41</sup> Activation by TMPRSS2 was suggested to be critical for robust spread of SARS-CoV-2 in the lung since it enables the endosome-independent virus entry and protects the virus from the antiviral activity of the interferon-induced transmembrane (IFITM) proteins, reducing SARS-CoV-2 sensitivity to innate immune restriction.<sup>37,42</sup> Thus, FCS seems to endow SARS-CoV-2 with a selective advantage in lung cells and primary human airway epithelial cells, but impairs replication in Vero E6, a cell line used for passaging SARS-CoV-2 that normally does not have high expression levels of TMPRSS2.<sup>37</sup> Correlating with the efficient cell entry of SARS-CoV-2 compared to SARS-CoV S protein, the RBD within its S protein was shown to bind with *higher* affinity to human ACE2.<sup>18,21</sup> Paradoxically, the full length SARS-CoV-2 spike was reported to have comparable or *lower* binding affinity for ACE2 compared to that of SARS-CoV spike.<sup>18</sup> Furthermore, SARS-CoV-2 RBD was suggested to be less exposed than SARS-CoV.<sup>18</sup> The high binding affinity of the RBD to ACE2, furin preactivation of the S protein, and hidden RBD in the spike cumulatively contribute to efficient SARS-CoV-2 cell entry and the potential to evade immune surveillance.<sup>18</sup>

Interestingly, the C-terminal polybasic R<sub>682</sub>RAR<sub>685</sub> sequence on the S1 subunit, generated by furin-mediated cleavage of the full-length precursor S glycoprotein, was shown to allow the virus to bind the transmembrane neuropilin-1 receptors acting

as entry cofactors, enhancing infectivity.<sup>43</sup> In addition to exploiting furin to gain entry into the host cell, SARS-CoV-2 may utilize the endogenous furin to cleave the S protein in the trans-Golgi network (TGN) right after virion assembly (virulence).<sup>44</sup> Moreover, the insertion of amino acids at the S1/S2 furin cleavage site of SARS-CoV-2 was suggested to create three potential unique N-acetylgalactosamine (GalNAc) O-glycosylation sites not predicted for the S protein of the bat or pangolin coronavirus.<sup>1</sup> Up to 20 different GalNAc transferases with different partially overlapping substrate specificities can catalyze the attachment of GalNAc to serine and threonine residues, and elongated O-glycan chains are subsequently created by other glycosyltransferases.<sup>45,46</sup> Since sites of O-glycosylation are cell-type dependent and would affect processing of the virus, this might affect cell tropism and consequently the virulence of SARS-CoV-2.<sup>26,47</sup> Human furin gene was discovered and sequenced in 1986, followed by its mouse homologue in 1990 (Figure 1).<sup>48,49</sup> In 1992, furin was purified and characterized in CHO cells, and monoclonal antibodies were produced to better study its function.<sup>50,51</sup> In 1993, the involvement of furin in HIV-1 membrane fusion and activation of diphtheria toxin was described.<sup>52–54</sup> Homology model of the catalytic domain of furin was created, and the covalent peptidylchloromethylketone inhibitors were shown to inhibit processing of viral glycoproteins in 1994.<sup>55,56</sup> The embryonic lethality of furin was reported in 1998, and the crystal structure of mouse furin homologue was solved in 2003.<sup>57,58</sup> The identification of the nonpeptide guanidinated 2,5-dideoxystreptamine inhibitors of furin was a significant discovery in 2006.<sup>59</sup> Eight years later, the first crystal structure of human furin was solved, and its involvement in processing of the S protein in MERS-CoV was reported.<sup>60</sup> Recently, the discovery of a furin cleavage site in SARS-CoV-2 in 2020 focused a spotlight on this enzyme (Figure 1). Herein, we review furin structure, function, substrates, recent inhibitors, and crystal structures with emphasis on furin's role in SARS-CoV-2 infection.

## ■ FURIN

Furin (EC: 3.4.21.75), also known as dibasic-processing enzyme, paired basic amino acid residue-cleaving enzyme (PACE), and proprotein convertase subtilisin/kexin 3 (PCSK3), is a 794 amino acid calcium-dependent ubiquitous proprotein convertase (PC).<sup>34,36,61–63</sup> Proprotein convertases are a group of multidomain mammalian endoproteases that feature a catalytic subtilisin-like serine protease domain.<sup>64</sup> Furin is encoded by the *FURIN* gene (also known as *FUR*, *PACE*, and *PCSK3*) located in the upstream region of the oncogene *FES* on chromosome 15 (*chr15:90,868,588–90,883,458* (GRCh38/hg38)) and hence was named *FUR* (*FES* Upstream Region), and the transcribed protein is named furin.<sup>65</sup> The PC family is comprised of 9 members (Supplemental Table 1).<sup>64</sup> Furin and six other members of the family, PC2, PC1/3, PC4, paired basic amino acid cleaving enzyme 4 (PACE4), PCS5/6, and PC7, are capable of cleaving proproteins having the general (Arg/Lys)<sub>n</sub>(Arg/Lys)↓ (R/K)<sub>n</sub>(R/K)↓ consensus motif (*n* = 0, 2, 4, and 6, X represents any amino acid, and “↓” indicates the scissile peptide bond).<sup>66,67</sup> Furin preferentially recognizes Arg-X-Arg/Lys-Arg↓-X as its highly sequence-specific substrate cleavage consensus motif.<sup>34</sup> Proprotein convertase subtilisin/kexin type 9 serine protease (PCSK9) and PC site-1 protease (S1P) also known as PCSK8 represent PC members with



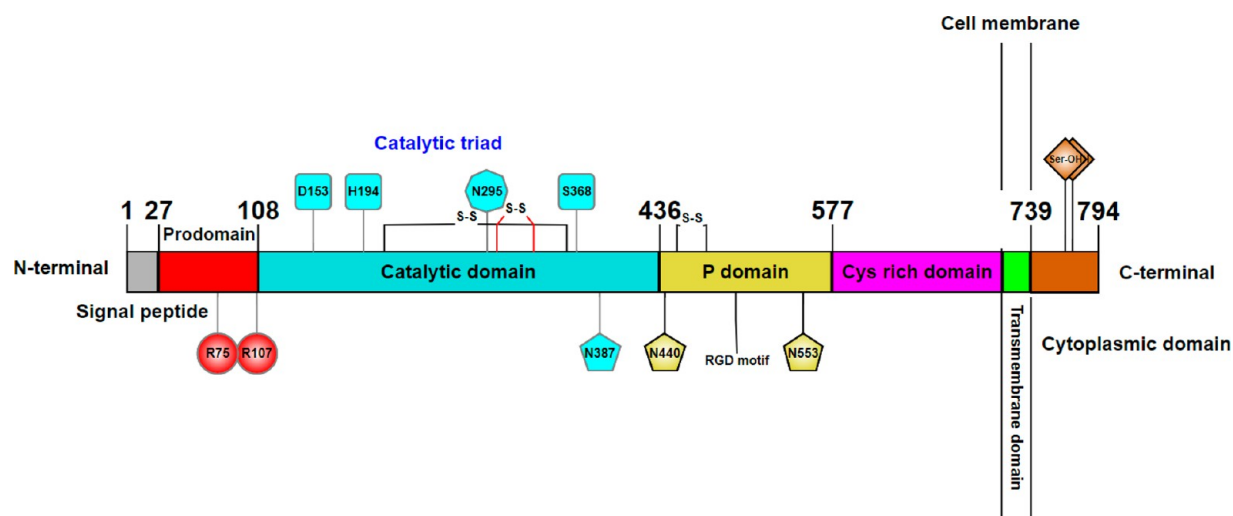


**Figure 2.** Domain structure of furin showing signal peptide (gray), prodomain (red), catalytic domain (cyan), P domain (gold), CRD (pink), transmembrane domain (green), and cytoplasmic domain (brown). Select residues are featured and colored according to their respective domain. Autocatalytic cleavage sites: Arg75 and Arg107 (circles); catalytic triad: Asp153, His194, and Ser368 (square); oxyanion hole: Asn295 (hexagon) and Asn387; potential glycosylation sites: Asn440 and Asn553 (pentagon); post-translational phosphorylation sites: Ser773 and Ser775 (rhomboidal). The image was created using Illustrator for Biological Sequences, IBS.<sup>82</sup>

nonbasic cleavage motifs.<sup>64</sup> The ubiquitously expressed S1P preferentially cleaves following the branched hydrophobic amino acids leucine, valine, or isoleucine, and secreted PCSK9 exists as an enzymatically inactive zymogen with its inhibitory propeptide and is implicated in cholesterol homeostasis.<sup>64</sup> Furin shuttles from the endoplasmic reticulum (ER) to the TGN through the endosomal system. An initial autocatalytic processing event takes place in the ER, whereas the second autocatalytic event takes place in the TGN, to produce the catalytically competent enzyme.<sup>34,57,68</sup> Furin mRNA is highly expressed in many tissues including liver, lung, placenta, and salivary gland (GTEx Analysis Release V8 dbGaP Accession phs000424.v8.p2). The protein expression is ubiquitous, and neuroendocrine, liver, gut, and brain are among the top tissues where furin is highly expressed (Supplemental Figure 1). Furin-like PCs, PACE4, PCS5, and PC7, are also widely expressed, whereas the expression of other PCs is more restricted.<sup>69,70</sup> PC members differ in the length and structure of their C-terminal cytoplasmic tails that contain variable intrinsic sorting signaling sequences guiding the trafficking and residences of the PC protein within the secretory pathways. Furin, PCSB, and PC7 recycle between the TGN and the cell surface, whereas PACE4, PCSA, and PCSK9 are mainly found on cell surface structure.<sup>69,70</sup> Only furin, PACE4, PCS/6, PC7, and S1P are reported to be involved in catalytic protein activation events of viral infections.<sup>69</sup> Consistent with the wide or ubiquitous expression of these PCs, they are responsible for most of the processing events within the constitutive secretory pathway and endosomes. PC knockout mice show variable phenotypes (Supplemental Table 1).<sup>69</sup> Thus, each PC member seems to fulfill some unique processing events and/or functions *in vivo*.<sup>64</sup> Nevertheless, a certain degree of functional redundancy, complementarity, or nonreciprocal functions appears to exist between these PCs during adulthood.<sup>64</sup> For excellent detailed reviews about PC family members and their structures and substrate specificities, see refs 64, 69, 71, and 72.

**Furin Structure.** Furin is a single polypeptide comprising an N-terminal signal peptide, inhibitory prodomain, catalytic endopeptidase domain, P domain, and cysteine-rich domain

(CRD) and C-terminal cytoplasmic domain (Figure 2).<sup>34</sup> The 81 amino acid prodomain acts as an intramolecular chaperone guiding proper folding, activation, and transport of furin. Asp153, His194, and Ser368 residues within the catalytic domain of furin form the catalytic triad that is highly conserved in the subtilisin-like family of proteins including all PC family members.<sup>68,73,74</sup> As seen with most proteases, two H-bonds are formed from the enzyme's residues to the oxyanion of the substrate. In furin, the action of the catalytic triad is complemented by the side chain amide of Asn295 and the backbone amino of the active site Ser368 serving as an oxyanion hole (Figures 2 and 3).<sup>74</sup> The catalytic domains of the other PCs are 54–70% identical in amino acid sequence to furin.<sup>34</sup> The activity of the catalytic domain is regulated by the P domain through pH modulation and calcium-dependent

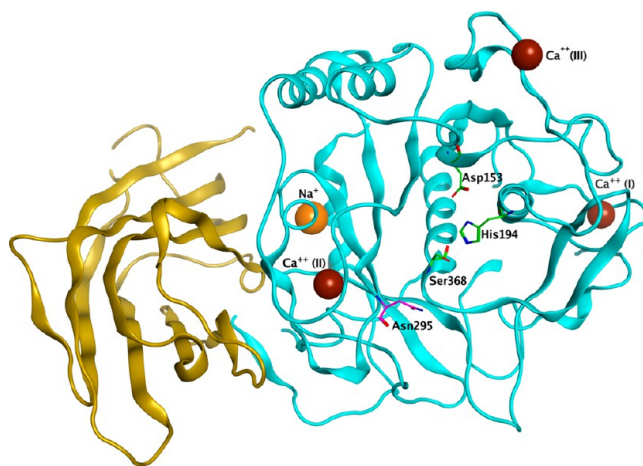


**Figure 3.** 3D structure of the catalytic and P domains of furin (apoprotein PDB: 5JXG).<sup>74</sup> The catalytic and P domains are shown in cyan and gold, respectively. Asp153, His194, and Ser368 (catalytic triad) are shown in green stick representation, and Asn295 (oxyanion hole) is in magenta. The three calcium and a sodium ion are shown as brown and orange spheres, respectively.

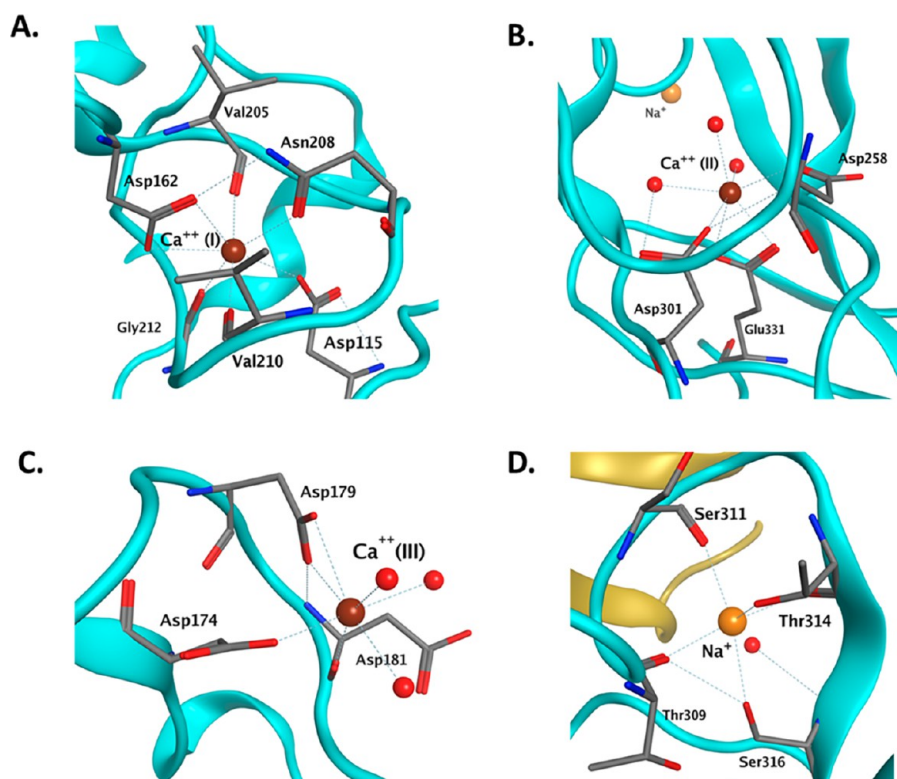


**Figure 4.** Three calcium binding sites (A–C) and sodium binding site (D) in the unliganded furin structure (PDB: 5JXG).<sup>74</sup> Amino acids are in stick display. Water molecules, calcium, and sodium ions are shown in red, brown, and gold spheres, respectively.

autoproteolytic processing.<sup>34,69,75</sup> The P domain, a domain of ~150 residues located immediately downstream of the catalytic domain, is a distinctive characteristic of members of the PC family.<sup>76</sup> Interestingly, the P domain appears to be named as such because it is essential for the proteolytic activity of furin.<sup>57,75,76</sup> Moreover, the P domain contains an Arg498-Gly499-Asp500 (RGD) integrin binding motif that appears to be essential for enzymatic activity (Figure 2).<sup>73</sup> The C-terminal of the P domain is thought to be at or close to the conserved Thr573, marking the point of sequence divergence among the PCs.<sup>73</sup> Furin, PCS, and PACE4 contain a conserved cysteine-rich domain that functions as an anchor to cell surface and interacts with the tissue inhibitors of metalloproteinases (TIMPs).<sup>69,74,77</sup> Furin and TIMPs have regulatory functions on an increasing number of important matrix metalloproteinases (MMPs), and their interactions appear to be involved in controlling the remodeling of extracellular matrix in a number of disease conditions such as cancer and atherosclerosis.<sup>78–80</sup> The transmembrane domain anchors the cytoplasmic domains of furin, PCSB, PC7, and SIP in the membrane structure of the constitutive exocytic pathway.<sup>69</sup> Finally, the cytoplasmic domain of furin allows for both efficient internalization from the plasma membrane and rapid trafficking from the plasma membrane to the TGN.<sup>34</sup> A multistep, compartment-specific pair of cleavages in the prodomain is crucial for the proper folding of furin's catalytic site to yield the functionally active enzyme.<sup>34,81</sup> Furin cleaves its own prodomain twice at sequences in a manner consistent with the consensus motif of the cleavage site.<sup>34</sup> First, in the neutral pH medium of the ER, a rapid cut ( $t_{1/2} = 10$  min) is made after Arg107 is located in the consensus furin cleavage site (R<sub>104</sub>TKR<sub>107</sub>↓), at the border of the catalytic domain.<sup>34</sup> The excised propeptide remains noncovalently associated with furin and functions as

an autoinhibitor.<sup>34</sup> The autoinhibition is lifted when the second intramolecular cleavage occurs within the mildly acidic TGN/endosomal system.<sup>34</sup> This second slower cut ( $t_{1/2} \approx 105$  min) takes place following Arg75 in the prodomain sequence (R<sub>70</sub>GVTKR<sub>75</sub>↓) during trafficking of the propeptide-furin complex.<sup>34</sup> Upon release of its prodomain fragment, the endoprotease activity of furin is unmasked, enabling functional processing of substrates in a *trans* fashion.<sup>34</sup> Furin is active at a broad pH range; between pH 5 and 8 furin retains >50% of its enzymatic activity, depending on the substrate to be processed.<sup>34</sup>

The three-dimensional (3D) structure of the unliganded form of the catalytic and P domains of furin (PDB: 5JXG) (Figure 3) shows a similar arrangement to bacterial subtilisin, where the catalytic domain core consists of a highly twisted  $\beta$ -sheet composed of eight  $\beta$ -strands, seven of which are parallel (C $\beta$ 1–C $\beta$ 7) and one is antiparallel (C $\beta$ 8) that is flanked by a total of seven helices, five adjacent (C $\alpha$ 2–C $\alpha$ 6) and two peripheral (C $\alpha$ 1 and C $\alpha$ 7), and by two  $\beta$ -hairpin loops (Figure 3).<sup>60,74</sup> The P domain is organized as a separate eight-stranded  $\beta$ -sandwich with a jellyroll-like  $\beta$ -barrel structure (Figure 3) with  $\beta$ -strands P $\beta$ 1a (448–453), P $\beta$ 1b (459–460), P $\beta$ 8 (561–573), P $\beta$ 3 (483–495), and P $\beta$ 6 (528–536) and opposing  $\beta$ -strands P $\beta$ 2 (464–471)–P $\beta$ 7 (545–553), P $\beta$ 4 (501–506) and P $\beta$ 5 (512–516).<sup>60</sup> The P domain plays a major role in the stabilization of the catalytic domain, which alone appears to be thermodynamically unstable, by virtue of the interaction of P $\beta$ 5 and P $\beta$ 6 strands at the edge of the P domain with various large loops in the catalytic domain including C $\beta$ 5–C $\alpha$ 4, C $\beta$ 6–C $\beta$ 7, C $\beta$ 7–C $\beta$ 8, and C $\beta$ 11–C $\beta$ 12.<sup>57,75,76</sup> This is mediated via a large hydrophobic surface as well as a number of electrostatic salt bridge interactions.<sup>57</sup>

Furin activity is strictly  $\text{Ca}^{2+}$ -dependent, and three calcium ions are bound per subunit.<sup>60,74</sup> Although  $\text{Ca}^{2+}$  is not involved in the catalytic cycle per se, all PCs require calcium for their enzymatic activity by influencing the active-site geometry.<sup>60,74</sup> The three calcium ions are located within the catalytic domain where  $\text{Ca}^{2+}$  (I) is coordinated to the side chains of Asp115, Asp162, Asn208, and to the backbone oxygens of Val205, Val210, and Gly212.  $\text{Ca}^{2+}$  (II) is coordinated to Asp258, Asp301, and Glu331 and  $\text{Ca}^{2+}$  (III) to Asp174, Asp179, and Asp181 (Figure 4).

Only  $\text{Ca}^{2+}$  (II) and  $\text{Ca}^{2+}$  (III) ions are removed by addition of the strong metal chelator EDTA, suggesting different affinities of the three calcium binding sites with decreasing affinities in the order of  $\text{Ca}^{2+}$  (I) >  $\text{Ca}^{2+}$  (II) >  $\text{Ca}^{2+}$  (III).<sup>74</sup> Near the active site cleft, a  $\text{Na}^+$  binding site was identified where  $\text{Na}^+$  ion is bound to the oxygen atoms of Thr309, Ser311, Thr314, and Ser316 (Figure 4). Other structural features of furin include three disulfide bonds, two within the catalytic domain: Cys211 to Cys360 and Cys303 to Cys333 and one within the P domain (Cys450 to Cys474) (Figure 2).<sup>60</sup> Disulfide bonds within the catalytic domain are required for compartment-specific folding events based on mutagenesis studies.<sup>83</sup> Within furin's cytoplasmic domain, two post-translational phosphorylation sites at Ser773 and Ser775 together with a cluster of acidic amino acids ( $\text{S}_{773}\text{DSEED}_{779}$ ) are essential for its intracellular trafficking and localization to the TGN through modulation of its phosphorylation state by casein kinase II (CKII) (Figure 2).<sup>84</sup> Mass spectrometric analysis showed that furin exists in di-, mono-, and non-phosphorylated forms in cells.<sup>84</sup> Moreover, furin has three potential glycosylation sites at Asn387, Asn440, and Asn553 and one predicted ubiquitination site at Lys748.<sup>85</sup> Many structural features of furin's active site are reminiscent of typical trypsin-like proteases. For example, the spatial restrictions at and around the catalytic Ser368, the deep S1 pocket with affinity for basic amino acid side chains at P1, the  $\beta$ -strand of the enzyme (Ser253-Gly255 in furin vs. Ser214-Gly216 in trypsin), with antiparallel  $\beta$ -sheet-like H-bonds with the peptide substrate and a typical hydrophobic tryptophan (Trp254 in furin vs Trp215 in trypsin) at its center.<sup>74</sup> Furin seems to exist in a so-called "off-state" that is incompatible with substrate binding.<sup>74</sup> Ligand binding triggers the transition from "off-state" to "on-state" and appears to be a prerequisite for preferential recognition of the four-residue basic sequence motif of furin substrates by the enzyme.<sup>74</sup> The active site of the enzyme contains an extended narrow canyon shaped substrate binding groove that is lined up with many negatively charged residues.<sup>60,74</sup> The highly acidic character of the substrate binding site explains the high binding affinity of positively charged substrates and inhibitors.<sup>60,74,86,87</sup>

**Furin Knockout and Mutations.** Previous mouse knockout studies with different PCs show variable phenotypes (Supplemental Table 1).<sup>69</sup> Germ-line furin knockout mouse studies validated an important role for furin in embryonic development with embryonic lethality occurring between day 10.5 and 11.5 due to failure of ventral closure, loss of axial rotation, and absence of chorioallantoic fusion.<sup>58</sup> Deletion of furin in endothelial cells resulted in cardiovascular defects, including septal and valvular defects potentially linked to impaired processing of transforming growth factor- $\beta$  (TGF- $\beta$ ).<sup>88</sup> Contrary to its embryonic lethality, furin knockout in the liver of adult mice was not lethal, and typical substrates of furin were still being processed even though with reduced efficiency,

suggesting possible redundancy among the PCs during adulthood.<sup>87</sup> Moreover, conditional deletion of furin in T cells allowed for normal development of these cells but caused functional impairment of regulatory and effector T cells as a consequence of diminished TGF- $\beta$  signaling.<sup>89</sup> The aforementioned observations implicate the crucial role of furin in TGF- $\beta$  biology and the potential therapeutic use of furin inhibitors for TGF- $\beta$ -dependent diseases. Previous mutagenesis studies showed that V72R or R75A prodomain mutants resulted in the loss of catalytic activity and impaired the propeptide second cleavage and removal.<sup>81</sup> While V72R showed abnormal accumulation in the early secretory pathway, the R75A mutant showed normal trafficking to the Golgi apparatus.<sup>81</sup> The catalytic domain D153N mutation also results in the loss of propeptide first cleavage, loss of catalytic activity, and abnormal accumulation in the early secretory pathway.<sup>81,90</sup> The two disulfide bonds within the P domain appear to be required for compartment-specific folding.<sup>83</sup> Thus, the C211S and C360S mutants were found to be localized to a post-ER compartment, with at least some of each mutant protein moving into the Golgi apparatus.<sup>83</sup> The C303S and C333S mutants localize in the ER and exhibit no autocatalytic propeptide excision.<sup>83</sup> Finally, mutation of either of the two phosphorylation sites Ser773 or Ser775 to alanine slightly reduces phosphorylation of furin.<sup>84</sup> Complete loss of phosphorylation and abnormal accumulation in the early secretory pathway was reported for the double mutants S773A and S775A, whereas double phosphomimetic mutants S773D and S775D increased localization in early endosomes.<sup>84</sup> Furin as a therapeutic target in SARS-CoV-2 has the potential advantage of a low probability of compensating mutations that may be expected with viral targets such as RNA-dependent RNA polymerase (RdRp) or the viral proteases: 3-chymotrypsin-like protease (3CLpro) and papain-like protease (PLpro).

## ■ SARS-COV-2 INFECTION AND FURIN

**Furin and Viral Infections.** Furin and furin-like PCs process a variety of viral proteins required for viral entry and propagation.<sup>69,91,92</sup> For example, HIV-1 surface protein gp160 cleavage into gp120 and gp41 is required for the formation of the envelope complex necessary for the virulence of HIV-1.<sup>54,93</sup> The surface proteins of highly pathogenic H5N1 and H7N1 avian influenza viruses have also been implicated as potential substrates for PCs.<sup>35,94</sup> Furthermore, furin catalyzes pre-membrane protein cleavage of various flaviviruses including dengue, West Nile, or Zika virus as well as the E2-E3 cleavage of the Chikungunya virus.<sup>95–97</sup> Interestingly, despite the previous reports describing the perfect furin cleavage site in the glycoprotein of Ebola virus, the furin proteolytic cleavage seems dispensable for viral spread and pathogenesis since the effect of furin inhibition is weak or nearly negligible for its propagation.<sup>98–102</sup>

**Furin Is Critical for SARS-CoV-2 Infection.** Several studies have suggested a critical role for the furin cleavage site in SARS-CoV-2 using mutated pseudotype viruses ablating the ability of the S protein to mediate cell–cell and virus–cell fusion in a variety of cell lines including Vero E6, HEK293, or Calu-3. Exchange of the S1/S2 site of SARS-CoV-2 against those of SARS-CoV and RaTG13 or deletion of the multibasic motif abrogate furin cleavage in vesicular stomatitis virus (VSV) pseudoparticles bearing S proteins.<sup>26</sup> Interestingly, a mutant with an optimized FCS featuring an alanine to lysine



exchange and an additional arginine residue at the S1/S2 site (Q<sub>677</sub>TNSRRRKR↓SVAS<sub>689</sub>) showed no increase in cleavability.<sup>26</sup> Fluorescence resonance energy transfer (FRET) substrates were used to study the cleavage of SARS-CoV-2 S1/S2 site by furin in an enzyme kinetic assay.<sup>30</sup> In agreement with the previous finding, FRET substrate with an optimized furin recognition site, where Ala was modified to Lys at the P2 position, was cleaved with similar efficiency compared to the wild-type sequence whereas exchange of Ala with Arg relatively enhanced cleavability by furin *in vitro*.<sup>30</sup> Formation of multinucleated giant cells (syncytia) increased in SARS-CoV-2 spike mutant (Q<sub>677</sub>TNSRRRKR↓SVAS<sub>689</sub>), suggesting that optimized S1/S2 sites in viral variants might show augmented cell–cell spread and altered pathogenicity.<sup>26</sup> Syncytia formation by SARS-CoV-2 increased in the presence of TMPRSS2 or trypsin, whereas deletion of the multibasic consensus motif in the spike protein of SARS-CoV-2 resulted in failure in syncytia formation even in the presence of trypsin or TMPRSS2.<sup>26</sup> As seen with MERS-CoV, processing of SARS-CoV-2 S protein was blocked in a concentration-dependent manner in the presence of covalent peptidomimetic furin inhibitor.<sup>26</sup> Blockade of SARS-CoV-2 S cleavage at the S1/S2 site abrogates entry into the TMPRSS2<sup>(+)</sup> Calu-3 human lung cell line with insufficient cathepsin B/L-dependent S protein activation pathway, but has no effect on virus entry into TMPRSS2<sup>(-)</sup> cathepsin B/L-dependent Vero E6 cells.<sup>26</sup> In another study, SARS-CoV-2 S protein was shown to be cleaved by endogenous furin in HEK293 cells transiently transfected with a plasmid encoding SARS-CoV-2 S protein.<sup>30</sup> Western blot analysis showed that both the uncleaved S protein and the S2 subunit were detected in the absence of a reversible peptidomimetic furin inhibitor, indicating that S is cleaved by endogenous proteases at the S1/S2 site in HEK293 cells.<sup>30</sup> Contrarily, S cleavage was efficiently prevented in the presence of furin inhibitor but not in the presence of the trypsin-like serine protease inhibitor aprotinin.<sup>30</sup> Interestingly, HEK293 cells transiently expressing TMPRSS2 showed two S cleavage products correlating with S and S2' in the absence of furin inhibitor.<sup>30</sup> The amount of S2' protein in transient TMPRSS2-expressing cells was similar in furin inhibitor treated and untreated cells, suggesting that only TMPRSS2 is responsible for S cleavage at the S2' site.<sup>30</sup> Furthermore, spread of SARS-CoV-2 infection in Calu-3 human airway cells was efficiently inhibited in a dose-dependent manner by either aprotinin, TMPRSS2, or furin inhibitors but not by the cathepsin inhibitor E64D, indicating that SARS-CoV-2 activation in these cells is independent of endosomal cathepsins.<sup>30</sup> Similar results were observed in human airway organoids (hAOs), where FCS within SARS-CoV-2 S protein was found to increase infectivity. Compared to SARS-CoV, SARS-CoV-2 had faster entry into Calu-3 cells with more frequent syncytia formation in hAOs.<sup>103</sup> Moreover, the FCS increased entry speed and plasma membrane serine protease usage relative to cathepsin-mediated endosomal entry.<sup>103</sup> While these studies point to the critical role of the “furin cleavage site” for viral infection, the exclusive proteolytic cleavage at S1/S2 site by furin cannot be robustly concluded since both of the used furin inhibitors may act nonspecifically on other furin-like PC members, especially in the case of the covalent inhibitor. Using the murine leukemia virus (MLV) pseudotyping system, Western blot analysis showed that SARS-CoV-2 S protein was entirely processed at the S1/S2 site during biosynthesis in HEK293 cells, presumably by furin in

the Golgi compartment, contrary to SARS-CoV S protein, which was incorporated into pseudovirions largely uncleaved.<sup>23</sup> A mutant of the S protein lacking the four amino acid residue insertion and the furin cleavage site (Q<sub>677</sub>TILRYSVAS<sub>685</sub>) that preserves only the conserved Arg685 in the wild-type SARS-CoV-2 S sequence (Q<sub>677</sub>TNSPRRRARYSVAS<sub>689</sub>) showed higher transduction efficiency in Vero E6 cells, whereas an opposite trend was observed in hACE2-expressing BHK cells.<sup>23</sup> This study speculated that FCS contributes putatively to expanded tropism and/or enhanced transmission of SARS-CoV-2 based on the ubiquitous expression of furin and other PCs.<sup>23</sup> Engineered SARS-CoV-2 mutants lacking the furin cleavage site ( $\Delta$ PRRA) showed faster kinetics and improved fitness in Vero E6 cells with diminished spike protein proteolytic processing compared to wild-type SARS-CoV-2.<sup>104</sup> On the other hand, the  $\Delta$ PRRA mutant showed reduced replication in Calu-3 cells, and attenuated replication was evident in hamster and K18-hACE2 transgenic mouse models of SARS-CoV-2.<sup>104</sup> However,  $\Delta$ PRRA replication was not completely ablated, and substantial tissue damage was observed in both models.<sup>104</sup> Importantly, protection against rechallenge with the wild-type SARS-CoV-2 was conferred by  $\Delta$ PRRA mutant.<sup>104</sup> Furthermore, mutagenesis, protease inhibition, and furin targeting small interfering RNA (siRNA) were used to confirm that furin preactivation enhances entry of replication-deficient lentiviruses pseudotyped with SARS-CoV-2 S protein into different types of ACE2-expressing cell lines, including Calu-3 lung epithelial and MRC-5 fibroblast cell lines.<sup>18</sup> Interestingly, the S molecules on the packaged SARS-CoV-2 pseudoviruses were still cleaved in the presence of an inhibitor of MMPs that was used to rule out the possibility that furin-dependent activation of MMPs is responsible for the indirect activation of SARS-CoV-2 S during packaging of the pseudoviruses.<sup>18</sup> The importance of furin as the sole protease responsible for S1/S2 cleavage was assessed in an interesting paper where CRISPR-Cas9 knockout of furin resulted in substantial reduction of S1/S2 cleavage and diminished production of infectious SARS-CoV-2.<sup>105</sup> However, loss of furin only reduced TMPRSS2-dependent cell–cell fusion, in either donor or acceptor cells, compared to mutation of the multibasic site that abolished syncytia formation completely.<sup>105</sup> Other studies suggested a less important role for furin or furin cleavage site in SARS-CoV-2 infection. The fusogenic capacity of the S protein, in the presence or absence of exogenous trypsin or human airway trypsin-like protease (HAT), was tested by transfer of both S and green fluorescent protein genes into HEK293T cells to mimic viral fusion.<sup>106</sup> The wild-type SARS-CoV-2 S protein and its nonfunctional FCS mutants could both effectively mediate cell–cell fusion in trypsin or HAT concentration-dependent manner.<sup>106</sup> It is worth mentioning that only high concentrations of trypsin were capable of entirely recovering the fusogenic capacity of SARS-CoV-2 S without FCS. The study inferred that the potent fusogenic activity of SARS-CoV-2-S may be attributed to structure and characteristics of the S protein rather than the presence of FCS. Moreover, the authors concluded that FCS may not be as critical as previously thought for the high fusion capacity of SARS-CoV-2 in human airways, where HAT is abundant; however, the ability of SARS-CoV-2 without FCS to infect target cells with high efficiency in human airway still needs more *in vitro* and *in vivo* evidence. In a retrospective study, 103 strains of SARS-CoV-2 with various DNA mutations were identified by analysis of 45828 SARS-CoV-2

genome sequences in the GISAID database as of June 13, 2020.<sup>107</sup> This analysis found 18 unique nonsynonymous point mutations, one deletion, and six gains of premature stop codon that may affect the furin cleavage site.<sup>107</sup> Since all the mutations were identified from live viral strains in COVID-19 patients, the furin cleavage site was suggested not to be required for SARS-CoV-2 entry to human cells *in vivo*.<sup>107</sup> These mutants were speculated to represent a subgroup of SARS-CoV-2 with diminished cellular tropism and transmissibility and were suggested to be experimentally tested as potential live-attenuated vaccine candidates.<sup>107</sup> Another study utilized SARS-CoV-2 MLV pseudoparticles decorated with SARS-CoV-2 viral envelope protein to study viral infectivity in Calu-3 and Vero E6 cell lines as models of early and late viral entry, respectively.<sup>108</sup> The pseudoparticles were engineered to harbor a luciferase reporter that drives the cells to produce quantifiable luciferase upon successful infection. Treatment of HEK293 cells with a furin covalent inhibitor, to prevent S1/S2 cleavage during biosynthesis, produced pseudoparticles with uncleaved S protein that were 30-fold more infectious than their cleaved counterparts in Vero E6 cells, where late acting cathepsin L is operating. Contrarily, these particles were less infective in Calu-3 cells, supporting the importance of prior proteolytic S1/S2 cleavage for subsequent S2' activation via the early acting TMPRSS2 in Calu-3 cells. A 2-fold increase in infection of pseudoparticles with uncleaved S protein in Calu-3 cells, but not in Vero E6 cells, was observed upon treatment of these cells with exogenous furin. Moreover, pseudoparticles produced in the presence of  $\alpha$ 1-PDX, a more selective furin inhibitor, failed to recapitulate the high level of enhancement provided by dec-RVKR-CMK at all tested inhibitor concentrations in Vero E6 cells.<sup>108</sup> Based on these findings, the authors suggested that furin may not be the only protease processing the S1/S2 site since dec-RVKR-CMK is capable of inhibiting other nonfurin PCs.<sup>108</sup> Because SARS-CoV-2 may use several cellular proteases as entry activators, inhibition of furin and TMPRSS2 or possibly other proteases might be necessary for achieving satisfactory therapeutic outcome.<sup>18</sup> Unlike TMPRSS2, furin is involved in more crucial pathways, and long-term inhibition of this enzyme might be associated with side effects. However, short-term treatment with furin inhibitors is well tolerated. Unfortunately, the results of a double blind randomized controlled clinical trial on the TMPRSS2 inhibitor camostat showed that it has no beneficial effect over a placebo in terms of time to clinical improvement, progression to intensive care unit (ICU) admission, or mortality.<sup>109</sup>

**Furin Processes Select Human Targets Related to COVID-19.** Several human targets related to COVID-19 pathogenesis are among furin substrates. The tribasic octamer peptide (R<sub>683</sub>RAR↓SVAS<sub>689</sub>) in SARS-CoV-2 S1/S2 cleavage site was found to be conserved among 10,956 of 10,967 circulating strains deposited at GISAID (<https://www.gisaid.org/>) as of April 28, 2020.<sup>110,111</sup> An interesting report identified striking mimicry between this cleavage site and an identical furin cleavable peptide (R<sub>201</sub>RAR↓SVAS<sub>208</sub>) on the human epithelial sodium channel  $\alpha$ -subunit (ENaC- $\alpha$ ).<sup>110</sup> This furin cleavage site of ENaC is thought to be critical for its activation.<sup>112</sup> ENaC functions to regulate the homeostasis of sodium ions (Na<sup>+</sup>) and water, and ENaC's expression levels are controlled by aldosterone and the associated renin-angiotensin-aldosterone system (RAAS).<sup>113</sup> ENaC is known to play an important role in controlling fluid reabsorption at

the air–liquid interface in the distal lung airways.<sup>113,114</sup> Analysis of single cell RNA-seq from 66 studies showed a significant overlap between expression of ENaC- $\alpha$  and the viral receptor ACE2 in cells linked to the cardiovascular-renal-pulmonary pathogenesis in COVID-19.<sup>110</sup> Accordingly, human ENaC activation may be compromised in SARS-CoV-2 infected cells, by SARS-CoV-2 exploiting host furin for its own activation.<sup>110</sup> Consequently, low ENaC activity on the surface of the airways may result in compromised fluid reabsorption, an important lung pathology in COVID-19 patients with ARDS.<sup>110</sup> Thus, inhibiting furin may reduce both SARS-CoV-2 and ENaC proteolytic cleavage by furin. If this is the case, then a direct activator of ENaC may be needed to be combined with furin inhibitors. Interestingly, ENaC activation by a small molecule known as S3969 did not require cleavage by furin.<sup>115</sup> Data from previous CoVs infections, such as SARS-CoV or MERS-CoV, and emerging data from the COVID-19 pandemic suggest that there could be substantial fibrotic consequences following SARS-CoV-2 infection.<sup>116,117</sup> In this context, furin may aggravate SARS-CoV-2 pathogenesis through the TGF- $\beta$  signaling pathway. Some viral components of SARS-CoV such as papain-like protease (PLpro) were previously demonstrated to upregulate the production of TGF- $\beta$  through Egr-1-dependent activation of TGF- $\beta$ 1 promoter via the ROS/p38 MAPK/STAT3 pathway.<sup>118,119</sup> Furthermore, N-protein of SARS-CoV was reported to modulate TGF- $\beta$  signaling through interaction with smad3, blocking apoptosis of SARS-CoV infected cells and thus promoting lung fibrosis.<sup>120</sup> Additionally, ACE2 expression is downregulated by SARS-CoV infection, and ACE2 was reported as a negative regulator of lung fibrosis through negative regulation of the local Ang-II levels.<sup>121</sup> Ang-II itself could also stimulate the production and secretion of TGF- $\beta$  in lung tissue, and an “autocrine loop” between Ang-II and TGF- $\beta$  was described where TGF- $\beta$  can also regulate the level of Ang-II.<sup>121</sup> Many severe cases of COVID-19 exhibit thrombotic and coagulation abnormalities promoting a hypercoagulable state and consequently increasing the rates of thrombotic and thromboembolic events.<sup>122</sup> A substantial proportion of COVID-19 patients have altered iron metabolism, lymphopenia, and multiple organ involvement.<sup>123,124</sup> Extremely low serum iron was a predictor of mortality, and alterations of iron metabolism were associated with hypoxemia in severe COVID-19 patients in the ICU.<sup>124–126</sup> During immune activation, release of cytokines such as interleukin-6 (IL-6) and bone morphogenetic protein-6 (BMP-6) into the serum activates hepcidin antimicrobial peptide (HAMP) gene expression, increasing the concentration of hepcidin which is the key regulator of iron homeostasis in humans.<sup>127–129</sup> Hepcidin lowers serum iron levels by inhibiting iron export from various tissues by triggering endocytosis of ferroportin that modulates iron storing in hepatocytes in the liver, recycling by macrophages in the spleen, and absorption by enterocytes in the duodenum.<sup>130,131</sup> Hepcidin is released as a precursor prepropeptide of 84 amino acids that is processed by two sequential cleavages: first at the signal sequence and second at the pro-region to produce the 25 amino acids mature peptide where proteolytic activation by furin at the consensus sequence (QRRRRR↓DTHF) takes place.<sup>130,132,133</sup> Chemical or siRNA-mediated inhibition of furin prevents hepcidin maturation but not its secretion from the cell.<sup>133</sup> High hepcidin during systemic inflammation reduces serum iron and consequently impairs hemoglobin synthesis and red blood cell production,



**Table 1. List of Select Bacterial Toxins Validated Experimentally As Furin Substrates and Their Corresponding Cleavage Sites<sup>a</sup>**

NCBI protein ID	description	substrate from	P1 no.	P6-P2P1P1'P2'	furin protein from	experiment <sup>b</sup>	refs
17380160	protective antigen	<i>Bacillus anthracis</i>	196	NSRKKRST	human	A	36
9955819	shiga toxin subunit A	<i>Shigella dysenteriae</i>	273	ASRVARMA	mouse	A, B	157
12231043	exotoxin A	<i>Pseudomonas aeruginosa</i>	304	RHRQPRGW	mouse	A, C	159
118949	diphtheria toxin	<i>Corynebacterium diphtheriae</i>	225	GNRVRRSV	mouse	B	52
113485	aerolysin	<i>Aeromonas hydrophila</i>	445	KVRRARSV	human	A, B	160
913139	$\alpha$ -toxin	<i>Clostridium septicum</i>	398	KRRGKRSV	human	A	161

<sup>a</sup>Data retrieved from Furin database.<sup>162</sup> <sup>b</sup>A: Substrate is cleaved with purified furin *in vitro*. B: Substrate is cleaved in furin-expressing cell lines but not cleaved in furin-deficient cell lines. C: The amount of substrate and cleaved product measured after coexpression of furin and substrate.

leading to anemia or inflammation.<sup>134</sup> Moreover, low iron levels may affect the immune function and hypoxia sensing.<sup>134,135</sup> For example, in a cohort of 111 COVID-19 patients, iron concentrations were below normal range in >90% of patients, and hepcidin levels were significantly increased in about 60% of patients.<sup>134</sup> Elevated hepcidin levels and higher concentrations of markers of inflammation and cell damage were more prevalent in older patients, especially males compared to females. The majority of hospitalized COVID-19 patients were hypoferric and had inflammation-dependent hepcidin upregulation.<sup>134</sup> Importantly, hepcidin was the most important predictor of death among other recognized predictors. Further studies are necessary to verify whether targeting the hepcidin either directly or indirectly through furin inhibition may influence COVID-19 prognosis. Finally, since multiple coagulation factors, including factor VIII, factor IX, and von Willebrand factor are furin substrates and require cleavage by furin for functional activation, the association between COVID-19 infection and defects in coagulation is a research area that needs to be addressed.

**Furin Overexpression May Be Linked to COVID-19 Comorbidities.** Several chronic comorbidities with increased death rates in COVID-19 patients including cancer, cardiovascular diseases, hypertension, type 2 diabetes, and lung disorders are overlapping with increased furin gene expression (Supplemental Figure 2).<sup>136,137</sup> High expression of furin and other PCs is correlated with several cancers including lung carcinoma,<sup>138</sup> breast cancer,<sup>139</sup> and head and neck carcinoma.<sup>140</sup> PCs are upregulated, and in some instances, elevated PC expression levels are correlated with enhanced migration and invasiveness, proliferation, metastasis, angiogenesis probably via activation of metalloproteinases, growth and angiogenic factors, and their receptors.<sup>66,92,141–143</sup> A recent study showed that furin was significantly associated with all-cause mortality and recurrent cardiovascular events in acute myocardial infarction patients independent of conventional risk factors and established markers.<sup>144</sup> Moreover, furin participates in the initiation and progression of atherosclerosis via regulation of lipid and cholesterol metabolism, inflammatory response, blood pressure, and the formation of atherosclerotic lesions.<sup>145–147</sup> Interestingly, vascular remodeling and atherosclerotic lesion progression is reduced by furin systemic inhibition in mice.<sup>148</sup> High plasma furin concentration is significantly correlated with pronounced dysmetabolic phenotype and elevated risk of diabetes mellitus and premature mortality.<sup>149</sup> Collectively, we believe that furin inhibition has a great potential as a therapeutic intervention for SARS-CoV-2 mainly through inhibition of viral entry and reduced pathogenesis.

## ■ FURIN AND BACTERIAL TOXINS

The role of furin in processing several bacterial toxins is well documented (Table 1).<sup>34,92</sup> For instance, furin proteolytically processes the protective antigen (PA) of the anthrax toxin at the cell surface.<sup>150</sup> The anthrax toxin secreted by bacillus anthracis encompasses three protein molecules: two toxic proteins namely lethal factor (LF) and edema factor (EF) and PA to activate immune protection against anthrax.<sup>151</sup> Following binding of PA protein to the host anthrax toxin receptor (ATR),<sup>152</sup> PA is cleaved by furin at the cell surface to a cell-associated 63 kDa PA (PA63) and a free 20 kDa PA (PA20).<sup>36,151,153,154</sup> The cell-associated PA63 protein forms heptamers that bind to either LF or EF and are internalized into early endosomes.<sup>153</sup> The acidic pH of the early endosomes catalyzes the formation of membrane channels by the PA heptamers that shuttle the toxic factors into the cytosol, resulting in anthrax toxicity manifested as edema, systemic shock, and death.<sup>153</sup> In the absence of furin, anthrax toxin fails to assemble and is rendered nonlethal.<sup>154</sup> Furin is also involved in the early endosomal activation of other bacterial toxins, including *Pseudomonas* exotoxin A (PEA), shiga toxin (ST), shiga-like toxin-1 (ST-1), and diphtheria toxin (DT).<sup>52,155,156</sup> All these toxins are A/B-type toxins that contain an active domain (A) and a binding domain (B) that are joined by a furin cleavage site near the C-terminal.<sup>156,157</sup> Following receptor binding, each toxin is endocytosed into early endosomes, where it is cleaved by furin.<sup>34</sup> The acidic pH medium of the early endosomal compartments is crucial for cleavage of ST, ST-1, and PEA by furin, but not for DT.<sup>34</sup> Inhibition of furin protects cells from shiga and other bacterial toxins.<sup>158</sup>

## ■ FURIN SUBSTRATES

Furin has >400 predicted protein substrates featuring the Arg-X-Arg/Lys-Arg↓-X sequence motif, including extracellular matrix proteins such as ADAM metalloproteinases,<sup>163,164</sup> bone morphogenetic protein 1 (BMP-1),<sup>165</sup> collagen,<sup>166</sup> fibronectin,<sup>167</sup> and integrins.<sup>168–170</sup> Furin can process several signaling peptides, hormones, and growth factors such as endothelin 1,<sup>171,172</sup> growth hormone releasing hormone,<sup>173</sup> insulin-like growth factor 1,<sup>174</sup> natriuretic peptide precursors,<sup>175,176</sup> platelet-derived growth factor polypeptides,<sup>177</sup> transforming growth factor beta (TGF- $\beta$ ),<sup>178,179</sup> parathyroid hormone,<sup>180</sup> and vascular endothelial growth factors C and D.<sup>181,182</sup> The substrates also include serum proteins, such as albumin,<sup>183</sup> coagulation factors IX and X,<sup>184</sup> complement component 3,<sup>185</sup> and von Willebrand factor,<sup>185</sup> transmembrane receptors, such as insulin receptor,<sup>186</sup> met proto-oncogene (hepatocyte growth factor receptor),<sup>187</sup> notch 1 receptor,<sup>188</sup> and low density lipoprotein related receptor,<sup>189</sup> the membrane

Table 2. Analysis of Favored and Disfavored Residues<sup>a</sup> in Furin Substrates from Three Different Studies<sup>193–195</sup>

P	Multiplexed oligonucleotide-peptide cleavage assay <sup>193</sup>	FRET decapeptides study <sup>194</sup>	<i>in silico</i> study <sup>195</sup>
P6	-	Ser and His	Ala, Pro or Asp
P5	Met	basic amino acids	Gly, Ala, Leu, Trp, His or Asn
P4	-	Arg	-
P3	Ser, Lys, Arg, Gln, Val or Leu	No clear preference	Gln or Glu
P2	Arg or Lys	Arg or Lys	Arg or Lys
P1	Arg >>> Lys	Arg	-
P1'	Ala, Ser, Glu or Asp Val, Pro or Cys	Ser	Ser Gly or Pro
P2'	Ile Gly	Val	Ala or Val Trp
P3'	Asp or Pro Val	Ala, Ser, Leu or Asp	Ser, Asp or Arg Gly or Glu
P4'	Ala, Pro, Asp or Glu Pro		Ala, Pro Asp or Glu Gly, Thr or Lys

<sup>a</sup>Favored residues are depicted in green, and disfavored are in red.

bound nonvoltage-gated sodium channel alpha ENaC- $\alpha$ , and others.<sup>112</sup> Furin's proteolytic processing of these substrates has been linked to multiple normal physiological and pathogenic processes, such as viral infection, bacterial toxin activation, cancer,<sup>190–192</sup> neurodegenerative disorders, diabetes, and atherosclerosis. The furin database (Furin DB), freely available online at <http://www.nuolan.net/substrates.html>, describes a total of 164 experimentally validated furin substrates of mammalian, bacterial, and viral origins and cleavage sites, experimental methods, and references to their original publications and associated drugs targeting furin substrates.<sup>162</sup>

The relative efficiency of furin and other PC members in cleaving over 100 decapeptide sequences was studied by Remacle et al. to aid in the design of effective inhibitors of the individual PCs (Table 2).<sup>193</sup> While only positively charged Arg and Lys are allowed at P1 position, Lys is associated with low hydrolysis efficiency in all PCs.<sup>193</sup> In contrast to other tested PCs, PC2 strongly prefers the presence of Lys instead of Arg at P2. The P2 Val increases the activity of PC4, PC5/6, and PACE4 but not furin, PC2, and PC7. The presence of Ser, Lys, Arg, and Gln dominates the P3 position of the substrates. Arg, Val, and Leu are favorable for multiple PCs except PC2, which has preference for Glu at the P3 site of the substrate. The efficient substrates frequently feature Ala, Ser, and Glu or Asp at the P1' position. Glu selectivity increases the activity of the PCs other than PC2, and Thr and Arg at P1' increase the sensitivity of the substrate to PC2 proteolysis. The P2' Ile is likely to stimulate the proteolysis of the peptides by the PCs. Asp or Pro at P3' has a stimulatory effect on the activity of PCs except PC2. The P4' Met enhances the peptide cleavage by PC4, PC5/6, PC7, and PACE4 but not by furin and PC2. Decreased efficiency of PC proteolysis is correlated with Val or Pro and Cys at P1', Gly at P2', Val at P3', Pro at P4', and Met at P5 in the substrate sequences. Furin substrate requirements were also explored using synthetic FRET decapeptides (Table 2).<sup>194</sup> Preferences were detected for substrates with Ser at P1', Val at P2', Ala, Ser, Leu, and Asp are almost equally frequent at P3', basic amino acids at P5, Ser and His at P6, and no clear tendency at P3.<sup>194</sup> Moreover, an *in silico* study demonstrated that the presence of the multibasic consensus motif alone is insufficient to determine furin proteolysis.<sup>195</sup> Substrates with Gln or Glu at the P3, Gly, Ala, Leu, Trp, His, or Asn at P5, and

Ala, Pro, or Asp at P6 have negative effects on cleavage efficiency. At P1', Ser was the most frequent residue, and Gly and Pro reduced the efficiency. While Ala or Val is predominantly found at the P2', Trp at P2' is correlated with the less efficient substrates. Ser, Asp, or Arg at P3' and Ala, Pro, Asp, or Glu at P4' characterize good substrates, while Gly or Glu at P3' and Gly, Thr, or Lys at P4' are not well tolerated by furin (Table 2).<sup>195</sup>

## ■ SUBSTRATE BINDING SITE OF FURIN AND THE MECHANISM OF PROTEASE ACTION

The amino acid residues that flank the cleavage site (scissile bond) in protein and peptide substrates will be referred to as P1 (binding S1 subsite in furin) and P1' (binding S1' subsite in furin). The amino acid that is N-terminal to the scissile bond is designated P1, and the amino acid that is C-terminal to the scissile bond are labeled P1', P2', and so on. As mentioned previously, the active site of furin contains an extended canyon shaped substrate binding groove which contains several negatively charged acidic residues: Asp258 and Asp306 (surrounding the S1 subsite); Asp154 and Asp191 (S2 subsite); Glu236 and Glu264 (S4 subsite); Glu257 and Asp264 (S5 subsite); and Glu230 and Asp233 (S6 subsite) (Figure 5).<sup>86</sup> It is worth mentioning that there are no acidic residues in the vicinity of the P3 amino acid of the peptide substrate. While no basic residues are present between the S5

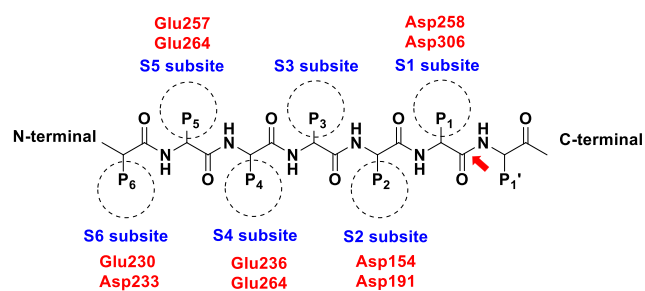


**Figure 5.** Schematic representation of furin substrates (P6–P1') and the acidic amino acids at each receptor subsite (S6–S1). The red arrow indicates the scissile bond cleaved by the catalytic triad.

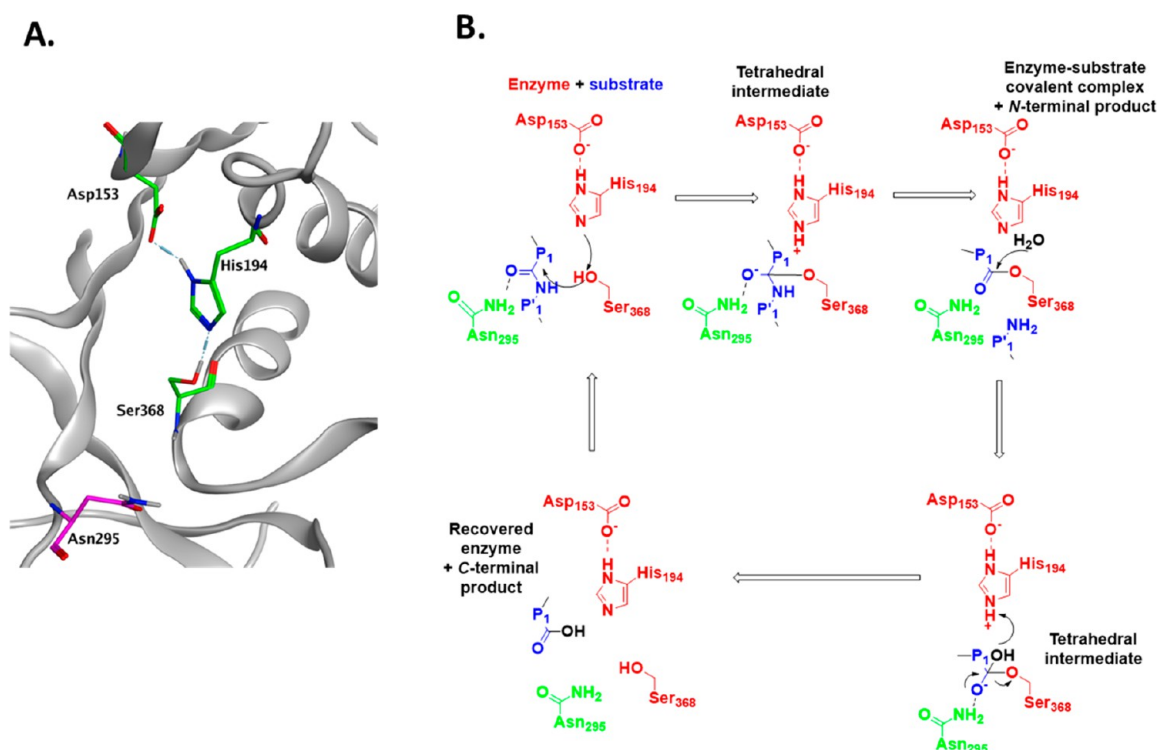


**Figure 6.** (A) 3D arrangement of the catalytic triad (green) and the oxyanion hole of furin (magenta). (B) 2D diagram of the proposed mechanism of proteolytic catalysis by furin. Catalytic triad residues are shown in red, oxyanion hole forming amino acid Asn295 in green, and the substrate in blue. The backbone amino of Ser368 contributes to the oxyanion hole.

and S1 subsites, basic residues Arg193, Arg197, and His364 are found only on the outer edge of the S1' subsite. The highly acidic character of the substrate binding site explains the high inhibitory potency of positively charged substrates and inhibitors.<sup>86</sup>

Mechanistically, the catalytic triad forms a charge-relay network to activate Ser368 as a nucleophile to attack the protein substrates with the Arg-X-Arg/Lys-Arg↓-X sequence motif at the scissile peptide bond. The formed covalent hemiketal intermediate is then hydrolyzed to release the product, and the free enzyme is regenerated. In furin, Asp153 is H-bonded with His194, probably increasing the  $pK_a$  of its imidazole nitrogen and thus allowing His194 to act as a powerful general base that activates the Ser368 nucleophile.<sup>74,196–198</sup> An oxyanion hole formed by the side chain Asn295 and the backbone amino of Ser368 stabilizes the charge build-up on the tetrahedral intermediates.<sup>74,196,197</sup> The histidine base aids the first leaving group by donating a proton and also activates the hydrolytic water molecule by abstracting a proton as the remaining  $\text{OH}^-$  attacks the acyl-enzyme intermediate (Figure 6). The chemical reaction catalyzed by furin normally involves limited conformational changes at the active site residues, unlikely to perturb remote substrate-binding subsites of the enzyme.<sup>74</sup> Typically, all residues determining specificity are located N-terminal to the scissile peptide bond within the extended substrate binding site.<sup>74</sup> The C-terminal segment is more loosely bound and may dissociate readily after hydrolysis.<sup>74</sup> Furin and furin-like PC enzymes are extensively investigated as drug targets.<sup>71,94</sup> Reported inhibitors include peptide-derived compounds,<sup>199–201</sup> peptidomimetic,<sup>202–206</sup> and nonpeptidic small-molecule compounds.<sup>59,207–209</sup>

## ■ FURIN INHIBITORS

In this section, we will focus on the most recent furin inhibitors. For earlier reviews, please refer to refs 210 and 211. Currently, there are no furin inhibitors under clinical development, and the progress of several potent inhibitors into preclinical candidates was hampered by their high molecular weights, low cell permeability, low cellular activity, lack of selectivity, metabolic and chemical instability, and cellular toxicity. However, there is a renewed interest in developing potent and selective furin inhibitors for the treatment of SARS CoV-2 infection. Availability of promising lead compounds and several cocrystal structures will guide the medicinal chemistry campaigns to develop candidates for clinical investigation.

### Peptide-Based and Peptidomimetic Inhibitors of Furin. Acyclic Peptidomimetic Furin Inhibitors.

Polyarginines and polylysines were among the first peptides reported to inhibit furin.<sup>201</sup> These peptides were identified by positional scanning of amidated and acetylated synthetic L- and D-hexapeptide combinatorial libraries.<sup>201</sup> The incorporation of the decarboxylated P1 arginine mimetics as 4-amidino-benzylamide (4-amba) group at the C-terminal of the inhibitor, phenylacetyl residues bearing basic guanidinomethyl or aminomethyl groups at the N-terminal residue P5 and different natural and unnatural amino acid residues such as *tert*-butyl glycine commonly known as *tert*-leucine (Tle) at P3 made a great contribution to the field.<sup>94,202,203,212</sup> Peptidomimetic inhibitors with a phenylacetyl-Arg-Val-Arg-4amba core structure are among the most potent noncovalent inhibitors reported so far.<sup>60,212</sup> Variation of the P5 residue correlates with significant changes in  $K_i$  values. One of the most potent noncovalent furin inhibitors reported is the tetrabasic peptidomimetic 1, 4-(guanidinomethyl) phenylacetyl-Arg-Tle-



Arg-4-amba (MI-1148), ( $K_i = 5.5$  pM) (Figure 7). Its P3 valine congener, 2 (MI-0701), displayed similar potency ( $K_i = 7.6$

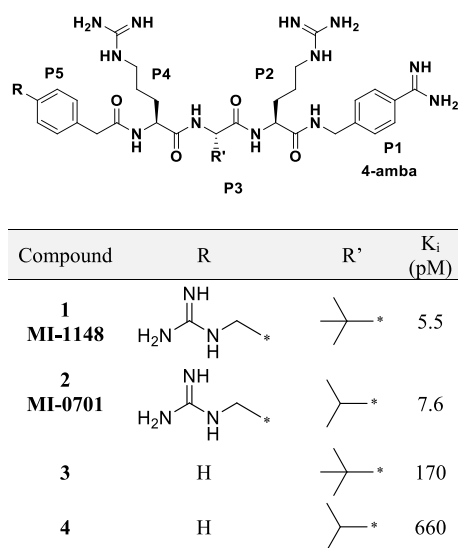


**Figure 7.** Structures of peptide-based furin inhibitors 1–4 and their  $K_i$  values.<sup>60,212</sup>

pM). The P5 des-guanidinomethyl derivative, 3 ( $K_i$  of 170 pM) and the phenylacetamido-RVR-amba 4 with P3 valine and P5 des-guanidinomethyl ( $K_i$  of 660 pM) were less potent than 1. The crystal structures of furin in complex with 1 and 4 were previously solved (PDB: 4RYD and 4OMD, respectively).<sup>60,212</sup> The 4-amba moiety in the deep well-defined S1 pocket of furin, the unnatural bulky Tle as P3 residue and the 4-(guanidinomethyl)phenylacetamido as P5 residue contributed to the picomolar affinity of compound 1.<sup>212,213</sup>

Within the S1 pocket, the 4-amba formed charged H-bond interactions with the side chain carboxylate of Asp306 and two H-bonds to the backbone oxygens of Pro256 and Ala292

(Figures 8 and 9).<sup>60,212</sup> The guanidine moiety of P2 arginine is engaged in direct interactions with Asp154 and water-mediated interaction to Asp192. Val or Tle at P3 are anchored to Gly255 by two strong  $\beta$ -sheet-like H-bonds. Surprisingly, replacement of Tle with the less branched Leu, Val, or penicillamine at P3 was generally correlated with lower potency in this series of inhibitors. No clear explanation for this difference in activity is evident since the side chains of these residues at P3 are pointed out to the solvent front and not engaged in any interactions with the enzyme (Figure 10). Intramolecular contacts of the Tle or Ile were suggested to stabilize the  $\beta$ -sheet-like backbone conformation of the bound inhibitor or a more favorable conformation in solution.<sup>212</sup> At P4, Asp264, Glu236, and Tyr308 contribute to the binding interactions with the basic arginine residue. 4-(Guanidinomethyl)phenylacetamido (P5) interacts with the side chain of Glu236, the backbone oxygen of Val231, and a conserved water molecule that extends the interaction to Asp233 and Ala267 at the surface of the enzyme (Figure 8 and 9 and Table 3). The proper spatial and electrostatic combination of P4–P5 residues interacts with the shared S4–S5 subsites of furin in a lock and key mechanism with no need for conformational rearrangements.<sup>60</sup> 3-Guanidinomethyl-Phac-RVR-amba interacts similarly at all the S1–S5 subsites of the substrate binding cleft of furin with  $K_i = 16$  pM, as observed in its cocrystal with furin (PDB: 4OMC and 5JXH).<sup>60,74</sup> The less extended 2-guanidinomethyl-Phac moiety at P5 has a weaker binding affinity ( $K_i = 196 \pm 15.2$  pM) than its meta congener.<sup>60</sup>

The 4-aminomethylphenylacetamido-Arg-Tle-Arg-4-amba 5 ( $K_i = 22.4$  pM)<sup>212</sup> furin cocrystal structure (PDB: 6EQW)<sup>214</sup> shows the relatively smaller 4-aminomethylphenylacetamido moiety with steric features similar to a lysine side chain. There is a charged H-bond with only Asp264 instead of the network of interactions with either the 4 or 3-aminomethylphenylacetamido counterparts (Figure 11). Interestingly, phenylacetamido-Cit-Val-Arg-4-amba 6 (Figure 11), an analogue of compound 4 bearing citrulline residue at P4, showed a significantly weaker binding

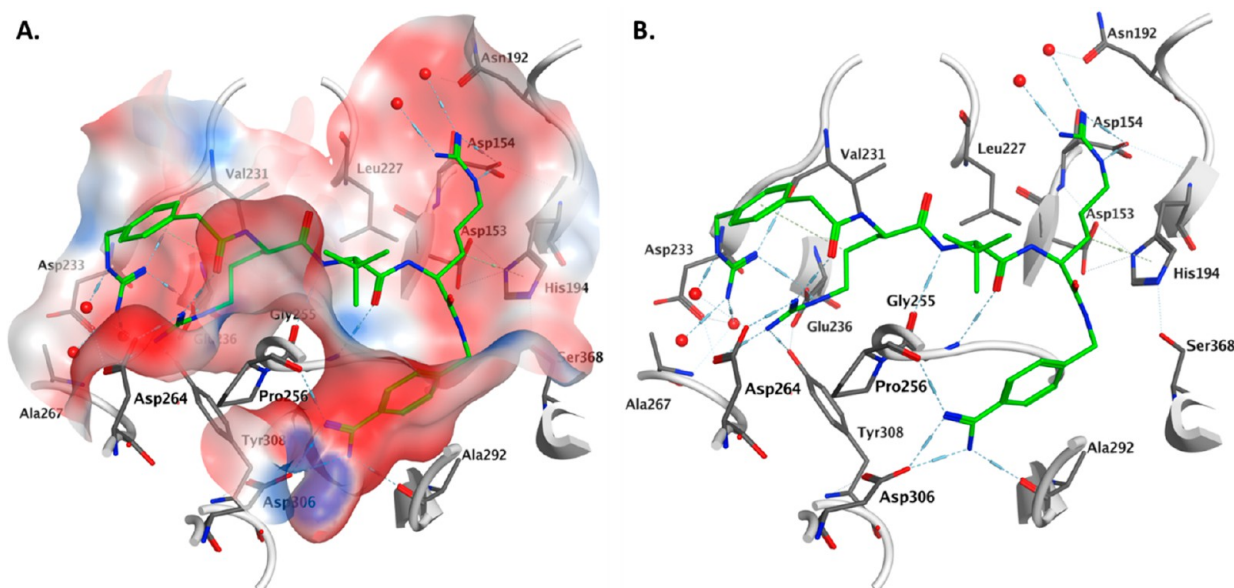


**Figure 8.** (A) Cocystal structure of 4-(guanidinomethyl)phenylacetamido-Arg-Tle-Arg-4-amba 1 at the active site of furin (PDB: 4RYD).<sup>212</sup> A partially transparent electrostatic surface is shown (red: negative, blue positive and white: neutral). (B) Stick representation model highlighting the interacting residues at the substrate binding site of furin. Water molecules interacting with the inhibitor are shown as red spheres.

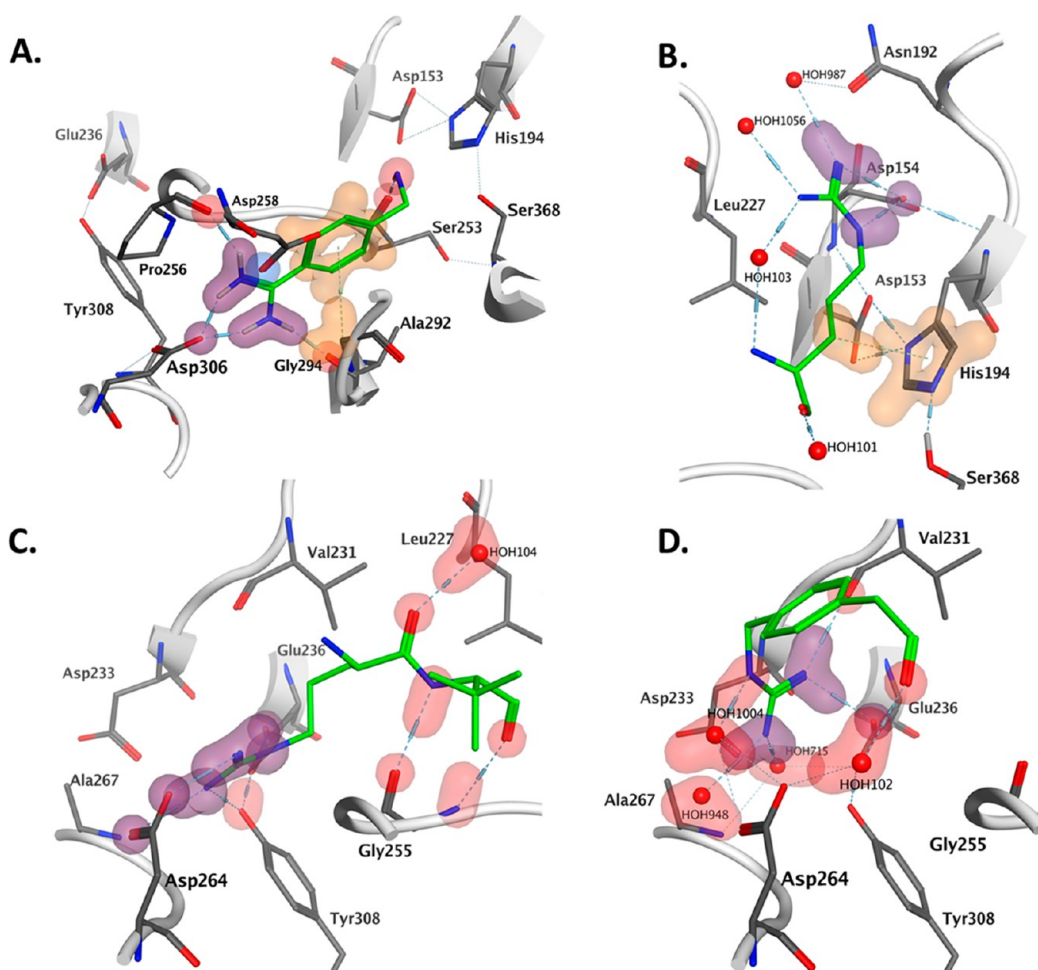


**Figure 9.** Detailed interaction maps of inhibitor **1** at each subsite (S1–S5) of the substrate binding site of furin (PDB: 4RYD).<sup>212</sup> (A) 4-amba (P1) at S1; (B) Arg (P2) at S2; (C) Tle (P3) and Arg (P4) at S3 and S4; and (D) 4-guanidino-phenylacetyl (P5) at S5. Red balloons highlight H-bonds, blue indicates ionic interaction, orange highlights arene-hydrogen interactions and magenta indicates charged H-bonds.

affinity ( $K_i = 238$  nM).<sup>202</sup> Citrulline is a noncharged analogue of arginine with a terminal urea residue instead of a guanidino group. While the steric features of urea are similar to guanidine, they differ in their H-bonding capabilities since all the amino groups in guanidine are H-bond donors, while the oxygen of urea in citrulline can only function as a H-bond acceptor. The cocrystal structure of this citrulline inhibitor (PDB: 6EQV) illustrates how the *trans* conformer of the urea moiety is differently accommodated at S4 subsite.<sup>214</sup> Similar to guanidine, the amino groups of the urea form H-bonds with Glu236, Asp264 and Tyr308; however, its oxygen atom misses a H-bond with the ionized carboxylate of Asp264 (Figure 12).<sup>214</sup> Importantly, the carbonyl group of the phenylacetyl moiety at P5 of the citrulline inhibitor occupies a different position to avoid repulsion from the urea oxygen. Consequently, an intramolecular H-bond between this carbonyl group and the backbone NH of Glu257 is lost. This alternative binding mode explains the lower affinity of the citrulline derivative.

Regarding the biological activity of this series, compound **1** (MI-1148) elicited a significant protective effect against anthrax and diphtheria toxins and strongly inhibited virus replication after infection of cells by H5N1 and H7N1, canine distemper virus, chikungunya virus, Semliki Forest virus (SFV), mumps virus, respiratory syncytial virus (RSV), and Dengue or

West Nile viruses.<sup>204,206,212,213,215</sup> Unfortunately, despite the lack of cellular toxicity up to 50  $\mu$ M in cell cultures, MI-1148 demonstrated a narrow therapeutic index in mice and inhibited other PCs, such as PC1/3, whereas PC2 was less affected.<sup>213</sup> While an intraperitoneal (i.p.) dose of 2.5 mg kg<sup>-1</sup> of MI-1148 was tolerated, three of four mice died without specific symptoms within the first hour after treatment with 5 mg kg<sup>-1</sup>, indicating acute rather than chronic toxicity.<sup>213</sup> This toxicity was suggested to correlate with the strong overall multibasic character of the inhibitor and the presence of the P1 amidine moiety.<sup>213</sup> In an effort to reduce the toxicity, the C-terminal benzamidine of compound **1** was replaced by less or nonbasic P1 residues in 7–10 (Figure 13).<sup>213</sup> However, these derivatives showed decreased potency (still in low nanomolar range) and negligible cellular efficacy.<sup>213</sup> Removal of P5 guanidino methyl of MI-1148, as in compound **3** ( $K_i = 0.17$  nM) or P1 amidine as in compound **10** (IC<sub>50</sub> = 580 nM), resulted in reduced *in vivo* toxicity, and these inhibitors were tolerated at a dose of 10 mg kg<sup>-1</sup> (i.p.). The similar toxicity of both inhibitors despite their great differences in inhibitory potency strongly suggests that the observed acute toxicity is not mediated through direct furin inhibition and would likely be the result of some unknown off-target effects.<sup>213</sup>

**Peptidomimetic Furin Inhibitors with Altered Basic Characters.** Replacement of P2 arginine in MI-1184 by the

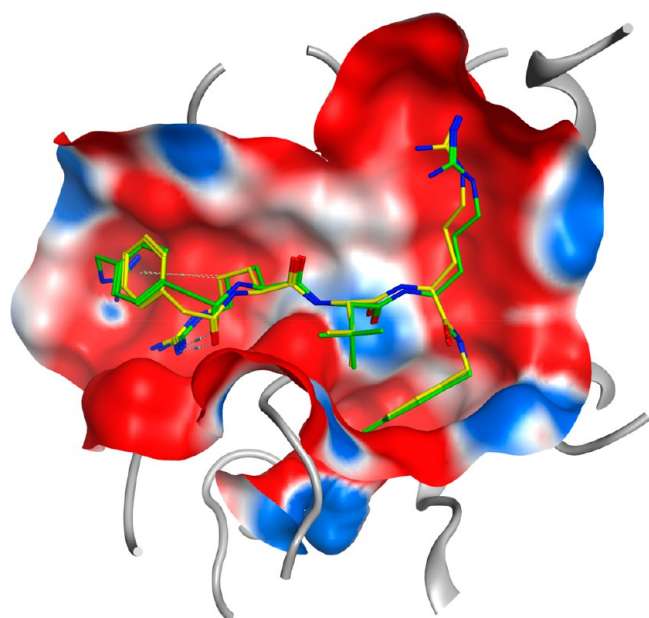


**Figure 10.** 4-(Guanidinomethyl)phenylacetyl-Arg-Tle-Arg-4-amba 1 (green) (PDB: 4RYD)<sup>165</sup> and phenylacetyl-Val-Arg-4-amba 4 (yellow) (PDB: 4OMD)<sup>51</sup> overlaid at the substrate binding site of furin.

**Table 3. Types of Interactions between the Peptidomimetic Inhibitor 1 and Furin, Their Energies, and the Distances between the Centroid of the Interacting Moieties**

interaction type <sup>a</sup>	inhibitor residue	interacting amino acid or solvent	energy (kcal/mol) <sup>b,c</sup>	distance (Å) <sup>d</sup>
IH	P1	Asp306	-29.51	2.70
H	P1	Ala292	-8.40	2.88
H	P1	Pro256	-6.00	2.94
H	P1	Ser253	-3.50	2.82
I	P1	Asp258	-2.48	3.36
A	P1	Gly294	-0.60	4.03
IH	P2	Asp154	-23.02	2.90
H	P2	HOH103	-5.70	2.97
H	P2	HOH1056	-4.20	2.80
H	P2	HOH101	-2.30	2.64
H	P2	HOH987	-1.90	3.08
A	P2	His194	-0.80	3.83
H	P3	Gly255	-8.60	2.96
IH	P4	Asp264	-23.28	3.15
IH	P4	Glu236	-10.73	2.95
H	P4	HOH104	-2.40	2.67
H	P4	Tyr308	-2.00	2.90
IH	P5	Glu236	-11.53	3.03
H	P5	Val231	-5.40	2.86
H	P5	HOH715	-4.00	2.85
H	P5	HOH948	-4.00	2.87
H	P5	HOH1004	-3.80	2.91
H	P5	HOH102	-2.00	2.85

<sup>a</sup>IH: Ionic and H-bonds; H: Hydrogen bond, I: Ionic bond; and A: Arene-hydrogen interaction. <sup>b</sup>Values were determined using MOE software package (2018) using PDB: 4RYD.<sup>212</sup> <sup>c</sup>When multiple interactions are aggregated into a single entry, this value is the sum of energy for all the represented interactions. <sup>d</sup>The distance between the centroids of the interacting atoms. When multiple interactions are aggregated into a single entry, this value is the average distance.

relatively less basic lysine in inhibitor 11 ( $K_i = 8.8$  pM, Figure 14) produced similar antiviral activity against West Nile and Dengue viruses in cell culture and no toxicity in mice up to 5 mg kg<sup>-1</sup>.<sup>213</sup> Recently, less toxic furin inhibitors exemplified by inhibitors 12 and 13 (MI-1851) were reported based on the replacement of arginine at P2 and/or P4 in inhibitor 1 by canavanine.<sup>30,205</sup> The structural modification impacted by this unnatural amino acid, with a weakly basic oxyguanidine group ( $pK_a = 7.01$ ), was hypothesized to result in a highly protonated species at pH 6.0 suitable for the inhibition of furin in the TGN. Less protonation at extracellular pH 7.4 can reduce the concentration of the completely protonated species, thus addressing the off-target interactions and improving the bioavailability. Canavanine-based inhibitors 12 and 13 are very potent furin inhibitors with  $K_i$  values <15 pM. Interestingly, inhibitor 13 showed reduced affinity for trypsin ( $K_i = 690$  nM) compared to 1, which is a relatively effective trypsin inhibitor ( $K_i = 52$  nM). Compound 13 had negligible affinity ( $K_i > 3$  μM) for the other tested trypsin-like serine proteases such as thrombin, factor Xa, and plasmin.<sup>205</sup> The crystal structures of select canavanine based inhibitors were solved, and identical side chain conformations were observed at P2 and P4 compared with the previously determined crystal structure of inhibitor 1. Compound 13 (MI-1851) displays significant antiviral activity against furin-dependent viruses, like respiratory syncytial virus, West Nile virus, and Dengue-2 virus, and exhibited a favorable pharmacokinetics (PK) profile and considerably reduced toxicity in mice and rats up to 15 mg kg<sup>-1</sup> compared to compound 1 (2.5 mg kg<sup>-1</sup>). Intravenous administration of 13 at 1 mg kg<sup>-1</sup> was tolerated with no death related to acute toxicity. SARS-CoV-2 S protein cleavage by endogenous furin in HEK293 cells was efficiently blocked in the presence of 13 but not by the broad range trypsin-like serine protease inhibitor aprotinin in HEK293 cells.<sup>30</sup> MI-1851 also was shown to inhibit SARS-CoV-2 spread at 10 μM in Calu-3 cells and was more potent than aprotinin.<sup>30</sup> SARS-CoV-2 replication in Calu-3 cells was independent of inhibition of endosomal cathepsins by E64d even at the highest dose of 50 μM.<sup>30</sup> Combining various TMPRSS2 inhibitors with furin inhibitor MI-1851 produced more potent antiviral activity against SARS-CoV-2 than an equimolar amount of any single serine protease inhibitor. Furin inhibitors with lower basic character have great potential to be developed as preclinical candidates for infectious diseases given that the inhibitors will be administered for relatively short period of time. Much testing is required to assess the toxic effects of chronic administration for other chronic conditions such as select cancers.

**Elongated and Shortened Peptidomimetic Furin Inhibitors.** Based on the notion that numerous PC substrates and inhibitors possess additional basic residues in their P5–P8 region contributing to their recognition by furin, novel elongated derivatives of the phenylacetyl-Arg-Val-Arg-4-amba 4 were synthesized.<sup>204</sup> The heptameric inhibitor phenylacetyl-Arg-Arg-Arg-Val-Arg-4-amba 14 containing three Arg amino acids as P4–P6 residues was the most potent compound in this series ( $K_i = 13.8 \pm 4.5$  pM) (Figure 15). Despite its excellent potency compared to the pentameric inhibitor 4, it was less potent than inhibitors 1 or 2 which possess a 4-guanidinomethylphenylacetyl residue as P5. The hexameric inhibitor Arg-Arg-Arg-Val-Arg-4-amba 15 ( $K_i = 33.7 \pm 1.3$  pM) lacking the phenyl acetyl moiety was about two times less potent (Figure 15). The cocrystal structure of furin in complex with



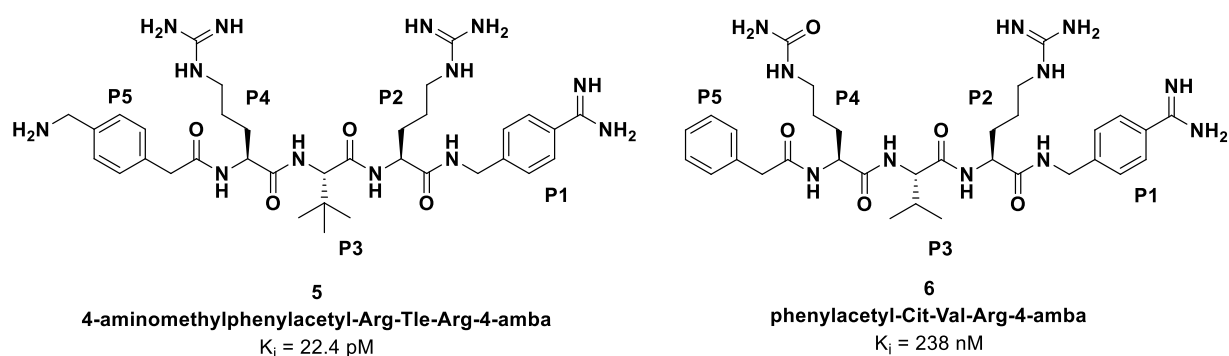


Figure 11. Structures of 4-aminomethylphenylacetyl-Arg-Tle-Arg-4-amba **5** and phenylacetyl-Cit-Val-Arg-4-amba **6**.<sup>202,212</sup>

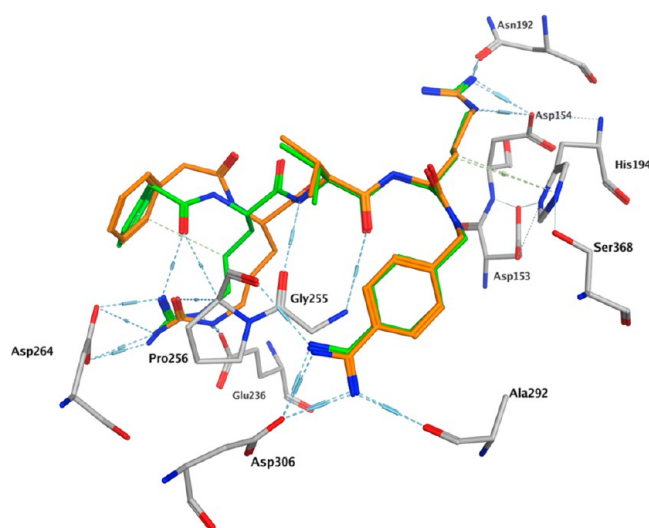
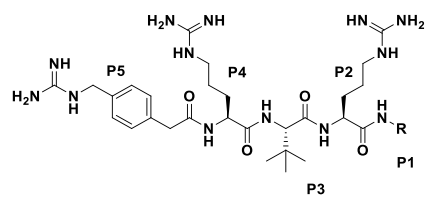


Figure 12. Substrate binding site of furin in complex with phenylacetyl-Arg-Val-Arg-4-amba **4** (green) (PDB: 4OMD)<sup>60</sup> overlaid on its complex with phenylacetyl-Cit-Val-Arg-4-amba **6** (orange) (PDB: 6EQV)<sup>214</sup>. Several amino acids are omitted for clarity.



Compound	R	$K_i$ (nM)	$IC_{50}$ (nM)	pKa
<b>1</b>		0.0055	ND	ND
<b>7</b>		$2.52 \pm 0.32$	$9.53 \pm 0.65$	9.28
<b>8</b>		$0.80 \pm 0.10$	$2.98 \pm 0.14$	6.50
<b>9</b>		$0.0223 \pm 0.0057$	$0.56 \pm 0.02$	9.46
<b>10</b>		ND	$580 \pm 20$	-

Figure 13. Structures of inhibitors **1** and **7–10**<sup>213</sup> and their  $K_i$ ,  $IC_{50}$ , and predicted  $pK_a$  values of the acetylated P1 residues.

**15** revealed molecular details of the S6 pocket (PDB: 6EQX).<sup>214</sup> Thus, the P6 arginine induced an unexpected turn-like conformation of the inhibitor backbone, which is stabilized by both intra- and intermolecular H-bonding (Figure 16).<sup>214</sup>

To prevent potential degradation of the N-terminal  $\alpha$ -amino group by aminopeptidases, the ultimate Arg at P6 was replaced by the non-natural D-Arg to produce **16** ( $K_i = 28.3 \pm 9.7 \text{ pM}$ ) (Figure 15). Further elongation with one or more D-Arg resulted in derivatives with lower potency possibly due to altered backbone conformation that would affect the side chain orientation, resulting in impaired interactions at the distal N-terminal binding pockets. In this series,  $N^\alpha$ (carbamidoyl)Arg-Arg-Arg-Val-Arg-4-amba (**17**) with  $K_i = 6.2 \text{ pM}$  shows similar potency to **1** (Figure 15).<sup>204</sup> While the elongated peptide-based inhibitors were suggested to have enhanced binding affinities and selectivity for certain PC members due to the low level of amino acid conservation beyond the S4 pocket, the increased molecular mass can negatively affect cellular permeability and PK profiles. Also, the increased overall basicity of such inhibitors maybe responsible for their cytotoxicity. Shortened (P1–P4) derivatives that lack the P5 moiety were thus prepared to decrease the molecular weight of this class of inhibitors. The best inhibitors of this series, 5-(guanidino)valeroyl-Val-Arg-4-amba **18** and its P3 *tert*-leucine analogue **19**, displayed weaker binding affinities with  $K_i$  values of 2.50 and 1.26 nM, respectively.<sup>204</sup> Unfortunately, none of these derivatives had antiviral activity against the tested SFV.

Other shortened (P1–P4) peptidomimetic furin/PC inhibitors exemplified by compounds **20–24** were patented to treat infectious diseases, cancers, and inflammatory/auto-immune disorders (Figure 17).<sup>216</sup> Compounds **20–22** featuring 4-amba or their *meta* or *ortho* fluoro derivatives at P1, 4-guanidinophenylalanine at P2, Val at P3, and acetyl lysine as P4 residues show potency in the nanomolar range. However, the hydroxyamidino derivative (amidoxime) **23** and amidino benzylsulfonyl-Val-Lys-4-amba **24** show potency only in the micromolar range.

The balance between the binding affinity, selectivity, optimal physicochemical properties, and metabolic stability of the peptide-based furin inhibitors is an important aspect to consider for selecting suitable candidates for preclinical development. Modification of an extended furin cleavage site in the immature hemagglutinin of avian influenza virus A led to the discovery of the sequence TPRARRRKKRT, showing nanomolar potency against furin ( $K_i = 23 \text{ nM}$ ).<sup>217</sup> The activity profile was later improved by removing two N-terminal residues in conjunction with C-terminal amidation and N-

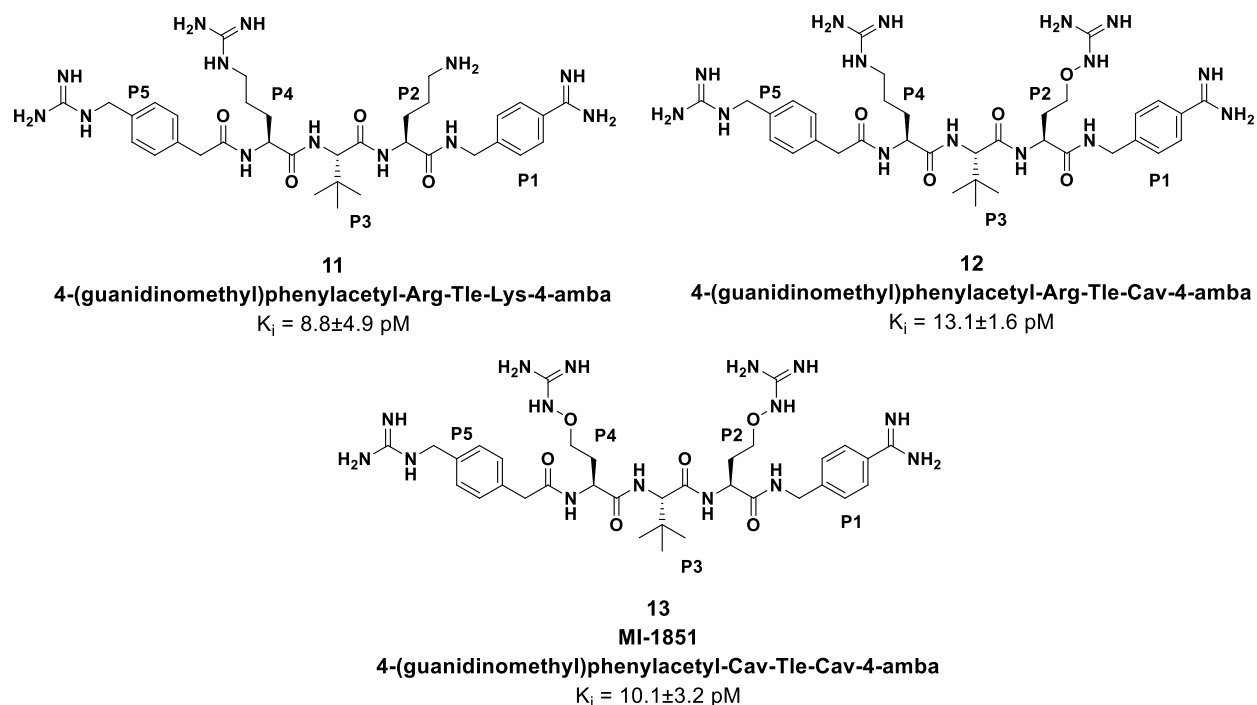


Figure 14. Structures of the less basic inhibitors 11–13.<sup>30,205,213</sup>

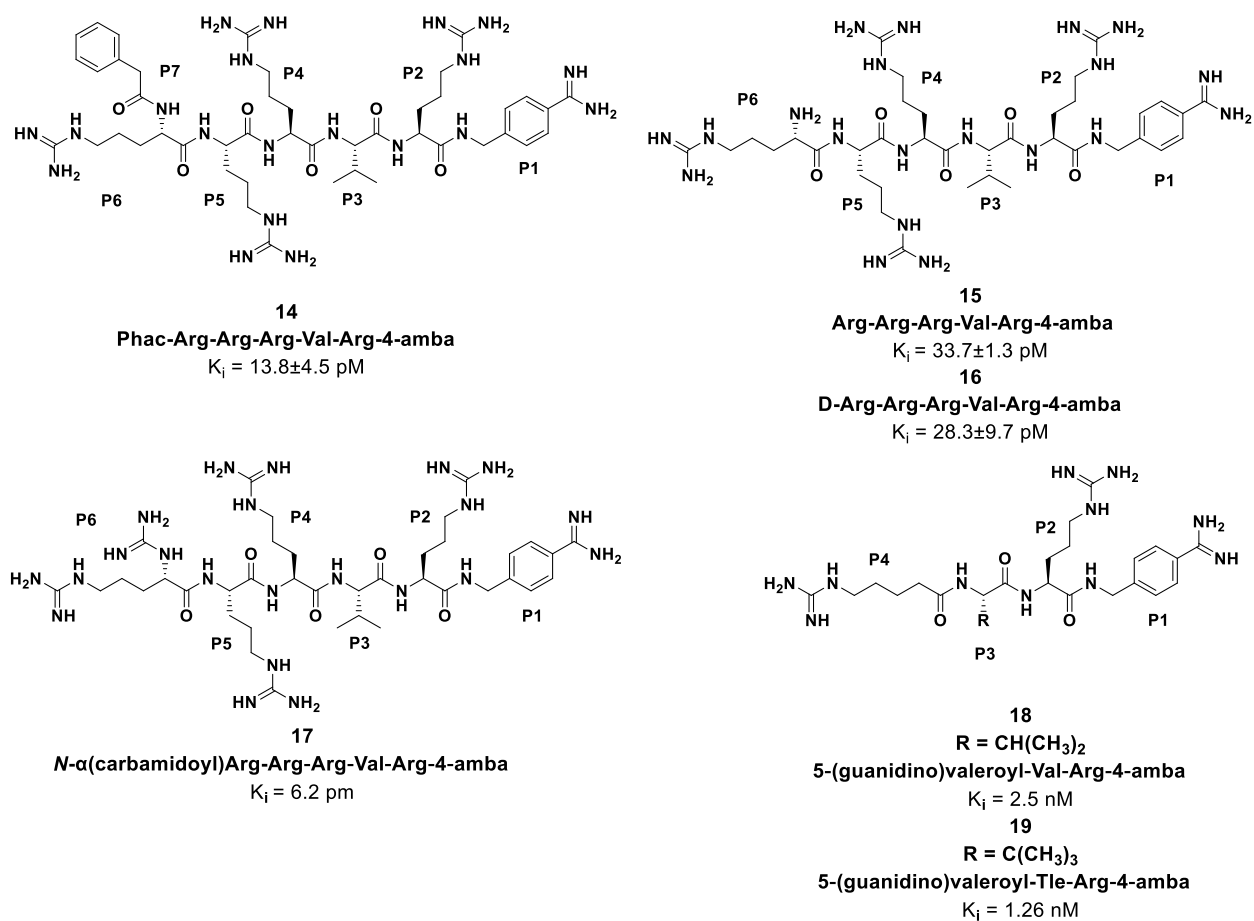
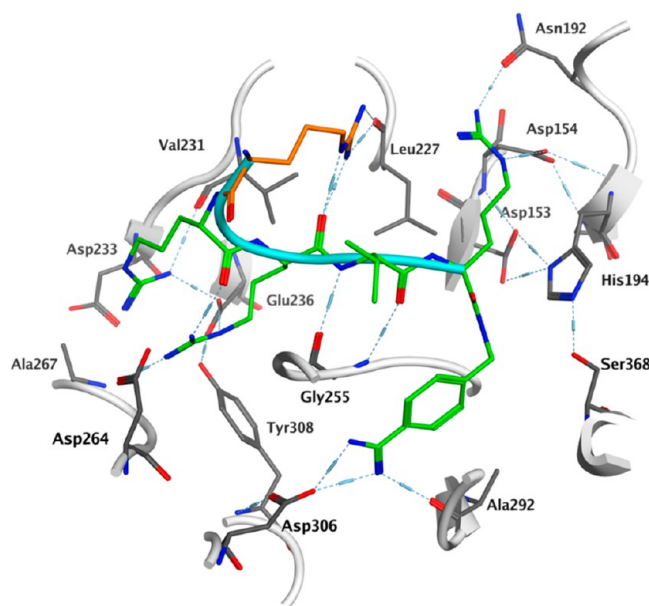


Figure 15. Structures of elongated and shortened peptide-based furin inhibitors 14–19.<sup>204</sup>

terminal acetylation to improve metabolic stability against cellular peptidases.<sup>218</sup> The optimized peptide sequence Ac-

RARRRKKRT-NH<sub>2</sub>, known as RXXT peptide 25, was able to block the processing of viral glycoproteins and anthrax toxin by



**Figure 16.** Substrate binding site of furin in complex with Arg-Arg-Arg-Val-Arg-4-amba **15** (PDB: 6EQX<sup>214</sup>). P1–P5 residues of the inhibitor are depicted in green and P6 arginine in orange. The formed turn-like structure is shown in cyan. Some receptor amino acids are hidden for clarity.

a furin-dependent mechanism in the nanomolar range ( $K_i = 19$  nM) without significant cytotoxicity but exhibited poor metabolic stability with  $t_{1/2} \approx 1.7$  h when determined using an HPLC assay.<sup>200,219</sup> More relatively stable elongated peptide-based inhibitors were reported by the same group for treating pathogenic infections by modification of the RXXT peptide **25** (Figure 18).<sup>219</sup> In this series of compounds, non-natural amino acid derivatives such as aza- $\beta^3$ -alanine, aza- $\beta^3$ -lysine, or aza- $\beta^3$ -arginine, decarboxylated arginine, and the arginine mimic 2-(4-(1-amino-4-guanidinobutyl)-1H-1,2,3-triazol-1-yl)propanoic acid were incorporated into the RXXT

peptide to give several derivatives exemplified by **26–31** (Figure 18 and Table 4).<sup>219</sup>

Many RXXT derivatives maintained nanomolar furin inhibitory potency *in vitro* (Table 4). While N-terminal variants exhibited no improved stability, RXXT variants modified at their C-terminal showed a 2–5-fold increase in half-life. The addition of the lipophilic amino-octanoyl group increased permeability of the RXXT peptide, suggesting that further modification of the furin inhibitors with lipophilic group(s) may increase their potency by balancing their physicochemical properties. The amino octanoyl derivative of **30** was among the most potent compounds as well as the P1 modified derivatives RXX[ $\Delta$ COOR]<sup>P1</sup> **28** and RXX[4-Amba]<sup>P1</sup> **29** (Table 4).<sup>219</sup> Surprisingly, the previously determined half-lives of the RXXT peptide **25** and several of its derivatives could not be reproduced using a more sensitive MS-based method where the  $t_{1/2}$  was about 4 min or even shorter.<sup>200</sup>

Positional scanning libraries of individual peptides modified at P5–P8 of the RXXT peptide **25** with natural amino acids showed that these derivatives were inhibitors rather than substrates despite the presence of the potential furin cleavage sites.<sup>200</sup> The most potent inhibitors were obtained by the incorporation of residues with hydrophobic or positively charged side chains.<sup>200</sup> The incorporation of small hydrophobic, nonpolar residues such as Ile, Val, or Pro at the P5 position resulted in analogs with improved affinity that was in agreement with previously reported data showing that inhibitors with short linear acyl groups at P5 (up to 5 carbons) exhibited potent inhibition against furin, whereas their longer chain counterparts were significantly less active.<sup>200</sup> At P6, no improvement in activity in comparison to the P5-modified peptides was observed, and only Leu or Lys was well tolerated instead of Arg at this position in the RXXT peptide.<sup>200</sup> All the P7-substituted analogs demonstrated a lower affinity toward furin, and the activity pattern was comparable to the P5 and the P6 series where inhibitors with acidic and bulky aromatic residues showed the lowest affinity toward furin.<sup>200</sup> The range of the  $K_i$  values for the P7 series

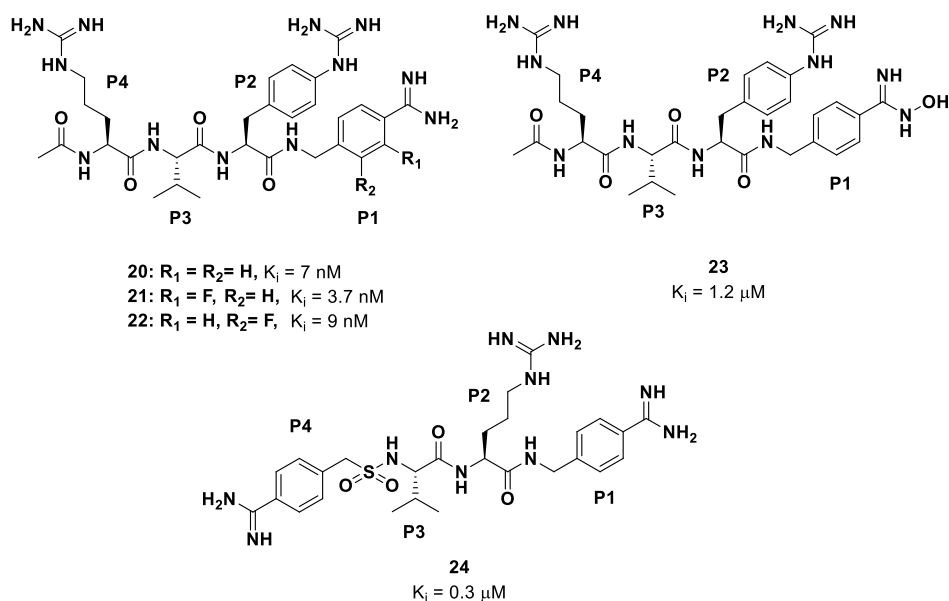


**Figure 17.** Structures of shortened (P1–P4) peptide-based furin inhibitors **20–24**.<sup>216</sup>



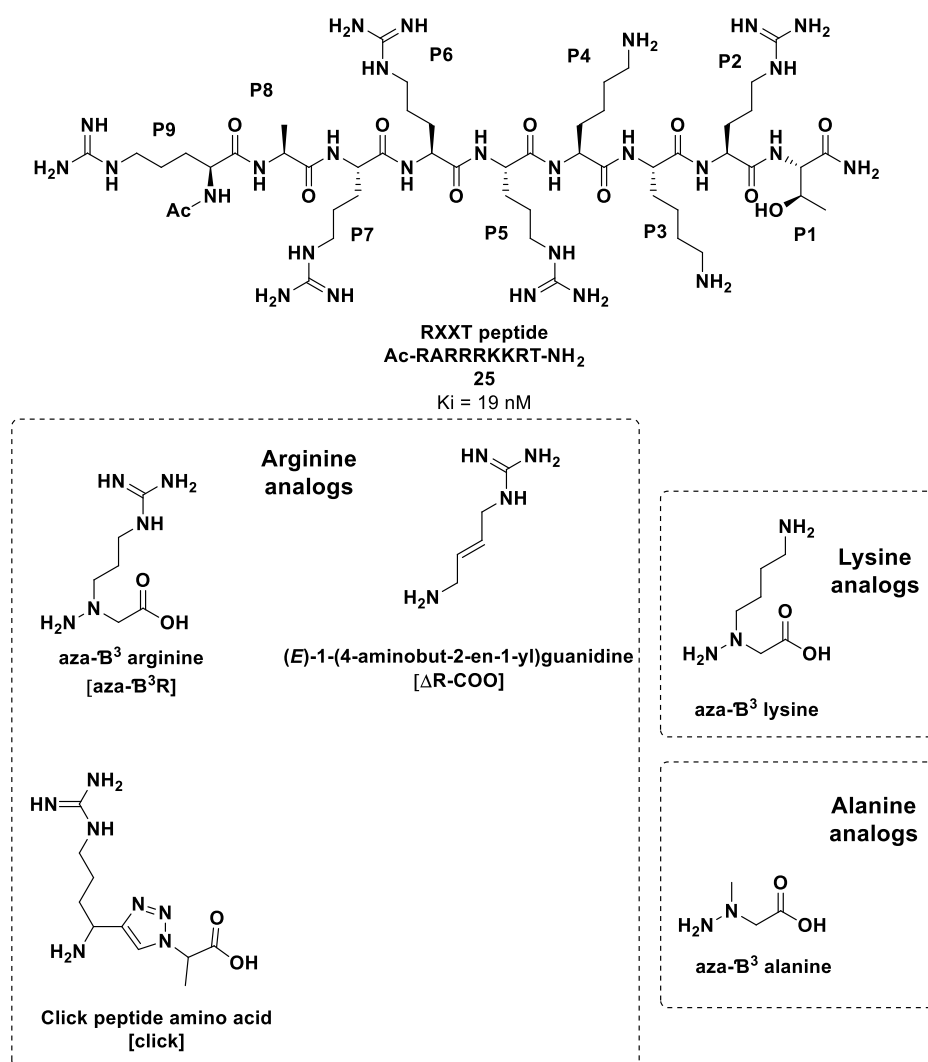


Figure 18. Structures of RXXT peptide 25 and various arginine, lysine, and alanine analogs.<sup>219</sup>

Table 4. Metabolic stability,  $K_i$ , Plasma  $t_{1/2}$  and  $IC_{50}$  Values of Furin Inhibitors 25–32<sup>219</sup>

compound	description	$K_i$ (nM)	stability (% remaining in plasma after 24 h)	plasma $t_{1/2}$ (h) <sup>a</sup>	$IC_{50}$ ( $\mu\text{M}$ )
25 RXXT peptide	Ac-RARRRKKRT-NH <sub>2</sub>	19	5	1.7 ± 0.2	>1000
26 RXXT cyclic <sup>P3–P9</sup>	[[Click]-RARRRK]KRT	16.7	28	0.7 ± 0.2	NA
27 RXXT [click] <sup>P8,P7</sup>	R-[Click]-ARRRKKRT-NH <sub>2</sub>	13	20	1.236 ± 0.007	NA
28 RXX [ΔR-COO] <sup>P1</sup>	Ac-RARRRKK[ΔRCOO]	7	NA	3.3 ± 0.2	71.0
29 RXX [4-Amba] <sup>P1</sup>	Ac-RARRRKK-[4-Amba]	3.8	NA	9.1 ± 0.2	>1000
30 RXXT [AzaB <sup>3</sup> R] <sup>P1</sup>	Ac-RARRRKK-[AzaB <sub>3</sub> R]T-NH <sub>2</sub>	28	57%	2.25 ± 0.05	314.5
31 RXXT [AzaB <sup>3</sup> R] <sup>P1,P8</sup>	Ac-[AzaB <sup>3</sup> R]-ARRRKK-[AzaB <sub>3</sub> R]-T-NH <sub>2</sub>	46	45%	2.68 ± 0.05	20.8
32 RXXT [AzaB <sup>3</sup> R] <sup>P8</sup>	Ac-R-[AzaB <sup>3</sup> R]-ARRRKKRT-NH <sub>2</sub>	12	29	1.04 ± 0.09	>1000

<sup>a</sup>The  $t_{1/2}$  values were different using a more sensitive MS-based method as reported in a recent study by the same group where the  $t_{1/2}$  of compound 25 was about 4 min.<sup>200</sup>

(15–38 nM) was significantly limited compared to analogs with either P5 (6–130 nM) or P6 substitution (14–270 nM), close to the recognition motif (P4–P1), suggesting that P7 is less important for furin binding. Substitutions of the P8 residue had little or no effect on the activity of the tested analogs, and most of the P8-modified peptides were slightly more potent.<sup>200</sup> Thus, P8 and P5 residues can be easily modified to generate more potent compounds. Specifically, small hydrophobic amino acids are preferred in the P5 position, whereas almost any residue is well-accepted at P8, indicating that the N-

terminal end of the peptide is outside of the furin catalytic pocket. For all of the screened residues (except for P8), the drop in the activity was significant once negatively charged amino acids were incorporated.<sup>200</sup> These observations were consistent with the reported crystal structures of furin in complex with various inhibitors, revealing the presence of the high negative-charge density within its active site (up to S7 subsites) and thus explaining the strong preferences for basic compounds. A series of 10–32 residue peptides whose sequence comprised of at least 10–22 arginine residues was

patented for the treatment of neuronal injury.<sup>220</sup> While the compounds were shown to have a protective effect in a glutamic acid excitatory model, no details about their exact mechanism of action was disclosed; however, inhibiting, downregulating, or affecting furin was suggested. A substantial intersect in targets that are cleaved by PCs and candidate mediators of fibrosis leads to the hypothesis that PCs inhibition is effective in inhibiting collagen matrix formation. Compound 2 (MI-0701) as an exemplary compound has been claimed to be used alone or in combination with antifibrotic agents to reduce collagen formation and procollagen propeptide.<sup>221</sup>

**Cyclic Peptidomimetic Furin Inhibitors.** Cyclic peptide-based inhibitors for furin and other basic PCs are very limited compared to their noncyclic derivatives.<sup>206</sup> Several cationic cyclic peptides originally designed as cargo molecules with cell-penetrating properties, containing four or five arginine residues in the ring segment, were found to inhibit furin with  $K_i$  values in the micromolar range.<sup>222</sup> Head-to-tail, head-to-side-chain, or side-chain-to-tail cyclization within a highly potent and selective PACE4 inhibitor, known as the multi-Leu octapeptide, Ac-LLLLRVKR-NH<sub>2</sub>, showed no improvement in terms of potency or selectivity. These inhibitors target both furin and PACE4 with inhibition constants close to 20 nM and 30 nM, respectively.<sup>223</sup> In a separate study, truncated analogues of the monocyclic sunflower trypsin inhibitor (SFTI-1) were engineered into furin inhibitors; the best monocyclic 12-mer peptide of this series contains Lys as a P1 residue and inhibits furin with a  $K_i$  of 0.49 nM.<sup>224</sup> Using a cocrystal structure of Arg-Arg-Arg-Val-Arg-4-amba (15) in complex with furin (PDB: 6EQX)<sup>214</sup>, various types of macrocyclic furin inhibitors were designed.<sup>206</sup> In type I and type II derivatives, the side chain of Lys as P3 was cyclized to the backbone NH of Arg at P5 or P6 via a glutaryl spacer. In type III inhibitors, the side chains of the P2 and P6 residues were linked where P2 Arg was replaced by Lys and P3 Val was replaced by Tle. A cyclic cell-penetrating peptide containing a Phe-2-naphthylalanyl-(Arg)<sub>x</sub> segment with 3, 4, or 5 Arg residues in the ring structure was fused with the P3 Lys side chain via a succinyl spacer in type IV. This short cyclic amphiphilic peptide motif in type IV was previously shown to bind strongly to cell membranes, followed by subsequent internalization.<sup>206</sup> Finally, simple head-to-tail cyclization of peptides with 6, 8, or 10 arginine residues was included in type V (Figure 19 and Table 5).

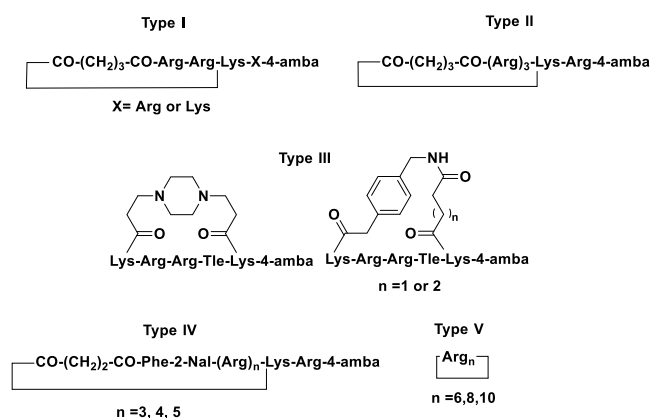
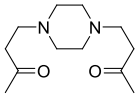
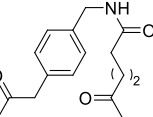


Figure 19. Chemotypes of cyclized derivatives 33–39.<sup>206</sup>

Type 1 inhibitors 33 and 34 showed classical competitive inhibition of furin with  $K_i$  values of 0.5 nM and 1 nM, respectively, but were less potent than P5–P1 inhibitor Arg-Arg-Val-Arg-4-Amba ( $K_i = 0.11$  nM) probably due to replacement of Val at P3 with Lys. Type 2 (P6–P3 cyclized inhibitor) 35 showed similar activity. The potency of inhibitor 35 (type 3) lacking the basic P2 residue was nearly identical to those of 34–36 (Table 5). The protonated piperazine moiety may partially compensate for the elimination of the basicity at the P2 side chain. Strong inhibition for most of the type 4 inhibitors was observed, where the  $K_i$  values of compounds 37–39 were <150 pM. Finally, weaker furin inhibitory potency was observed for the cyclic polyarginine derivatives (type 5) ( $K_i > 20$  nM), compared to their linear analogues with  $K_i$  values <10 nM. While most of the derivatives were relatively potent furin inhibitors *in vitro* ( $K_i$  in the low nanomolar or even subnanomolar range), negligible antiviral activity against respiratory syncytial virus in cells was detected for these cyclic derivatives. Thus, cyclization seems to have no apparent advantage in these cases, and the increased molecular weight of these derivatives may contribute to their lack of cellular activity. The cocrystal structures of seven of these cyclic derivatives in complex with furin were determined, and full ligand electron density was observed in only three complexes. For the other cases, structures could be determined only for the P6/P5–P1 segments, which directly interact with furin (Figure 20).<sup>206</sup>

**Covalent Peptidomimetic Inhibitors of Furin.** Surprisingly, furin has limited reactivity toward typical covalent inhibitors of serine proteases such as diisopropylfluorophosphate (DFP), 4-(2-aminoethyl)benzenesulfonyl fluoride (AEBSF), and phenylmethylsulfonyl fluoride (PMSF) (Figure 21).<sup>74</sup> While steric reasons were excluded based on modeling studies, a possible explanation may be related to the electronic properties of these inhibitors and/or the activation state of furin's active site. Decanoyl-Arg-Val-Lys-Arg-chloromethyl ketone (RVKR-CMK) 40 is a nonselective, irreversible, and cell-permeable competitive inhibitor of all PCs as well as other trypsin-like serine proteases.<sup>55,56</sup> The ternary complex of furin with 40 and the inhibitory camelid antibody Nb14,<sup>225</sup> at a resolution of 2.3 Å, was solved as a dimer (PDB: 5JMO) (Figure 21). No major conformational changes in the catalytic cleft nor in the active site of furin upon complex formation were observed. Similar to covalently inhibited mouse furin, a typical covalent complex between the human ortholog and the CMK inhibitor was formed. P1-Arg binds the S1 deep pocket, the methylene of the inhibitor is covalently bound to His194 nitrogen, and the oxygen of Ser368 forms a tetrahedral hemiketal with the carbonyl group of the inhibitor mimicking a transition state intermediate extending the interaction to the oxyanion hole Asn295 and Ser368 through H-bonding (Figure 21). Other interactions at P2–P4 are similar to noncovalently inhibited furin structures with the decanoyl tail at P5 extending to solvent at S5 with no appreciable interactions. Nb14 binds the P-domain of furin noncompetitively.<sup>225</sup> The interaction interface at the P-domain of furin involves residues Pro458-Asp460, Thr492-Asn496, Ala525-Asn529, and Asn558-Thr564, whereas the complementary surface of Nb14 involves Tyr32-Tyr35, Trp47-Arg53, Ser56-Asp59, Val98-Ala102 as well as Trp106.<sup>225</sup> Several tyrosine residues at the interaction interface including Tyr32, Tyr35, Tyr109 of Nb14 and Tyr560 of furin form specific H-bonds contributing to the hydrophobic character of the surface. Steric exclusion of specific substrate

Table 5. Compounds 33–39 Structures and Their  $K_i$  and Reported PDB Codes<sup>206</sup>

Compound	Structure	$K_i$ (nM)	PDB	Electron density of the linker was determined
33	c [glutaryl-Arg-Arg-Lys]-Arg-4-amba	0.504±0.097	6HZA	Yes
34	c [glutaryl-Arg-Arg-Lys]-Lys-4-amba	1.05±0.14	6HZB	Yes
35	c [glutaryl-Arg-Arg-Arg-Lys]-Arg-4-amba	0.68±0.1	6HZD	Yes
36	 Lys-Arg-Arg-Tle-Lys-4-amba	0.491±0.056	6HLE	No
37	 Lys-Arg-Arg-Tle-Lys-4-amba	1.17±0.26	6HLE	No
38	c [succinyl-Phe-2-Nal-Arg4-Lys]-Arg-4-amba	0.0538±0.0059*	6HLB	No
39	c [succinyl-Phe-2-Nal-Arg3-Lys]-Lys-4-amba	0.618±0.002	6HLD	No

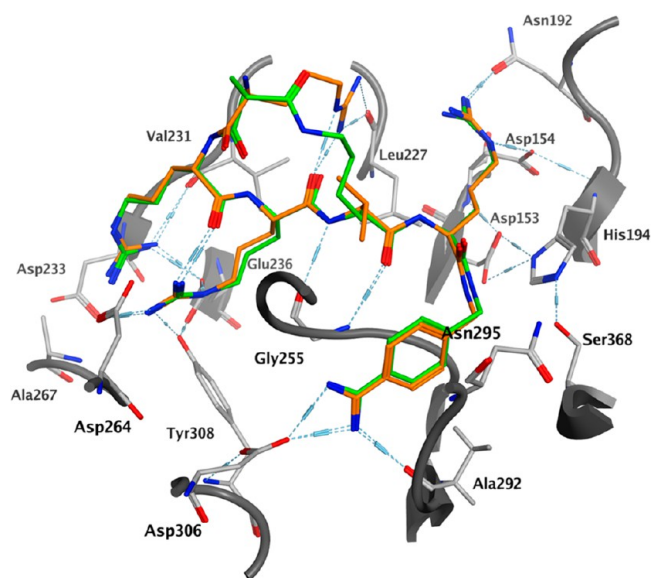


Figure 20. Arg-Arg-Arg-Val-Arg-4-amidinobenzylamide 15 (orange) in complex with furin (PDB: 6EQX)<sup>214</sup> superimposed on the cyclic inhibitor c [glutaryl-Arg-Arg-Lys]-Arg-4-amba 33 (green) in complex with furin (PDB: 6HZA)<sup>206</sup>.

conformers explained the inhibitory action of the antibody against large bulky proprotein-like but not small peptide substrates.<sup>225</sup> Antibodies or small-molecule inhibitors that selectively or preferentially inhibit the binding of the bulky viral peptide sequences maybe advantageous for inhibiting furin by avoiding nonselective targeting other PC family members.

**Nonpeptide Inhibitors.** Nonpeptide small-molecule inhibitors may overcome the liabilities associated with protein or peptide-based inhibitors such as high molecular weight, poor permeability, stability, and PK properties, and potential immunogenicity leading to toxicity. Below, we will discuss promising small-molecule furin inhibitors reported to date.

**2,5-Dideoxystreptamine Derivatives.** Guanidinated aryl derivatives of 2,5-dideoxystreptamine were first described in 2006.<sup>59</sup> These derivatives are competitive inhibitors of furin with  $K_i$  values in the nanomolar range that are comparable to the potency of protein or peptidomimetic inhibitors and considerably more potent than the diterpene natural products of the andrographolide family, their succinyl esters, and some terpyridyl copper or zinc complexes, all showing low inhibitory activity in the micromolar to millimolar range (Figure 22).<sup>59,226,227</sup>

2,5-Dideoxystreptamine derivatives display selectivity toward furin and PC5/6.<sup>59</sup> The most potent furin inhibitor bears four guanidine substituents ( $K_i = 6$  nM) (Table 6). Derivatives containing two aryl substituents were slightly more effective than those containing more aryl substituents, and monoaryl derivatives show little or no inhibition of furin ( $K_i > 100$   $\mu$ M). A guanidine moiety at the *para* position seems to be essential since its removal or shift to the *ortho* position abolished activity. Replacement of the ether group by a carbamate group ( $-NHCOO$ ) resulted in reduced potency. In contrast to polyarginine peptides, no linear correlation was evident between the number of positively charged guanidine moieties in these structures and their inhibitory activities (Table 6).<sup>59</sup>

A soaking technique with unliganded furin hexagonal crystals was attempted to determine the crystal structure of the diaryl derivatives **A3** (meso) and **A6** (racemate) with  $K_i = 6$  nM and 12 nM, respectively, and the less potent triaryl derivative **A8** (racemate) ( $K_i = 46$  nM).<sup>229</sup> The binding interactions were apparent only for **A8** as indicated by the electron density map, but not for **A3** and **A6** despite their lower  $K_i$  values.<sup>229</sup> A different binding mode for the diaryl derivatives **A3** and **A6** was suggested where their binding might involve interactions with regions disrupted by crystal packing. Another explanation was based on low binding site occupation of **A3** or **A6** within the time frame of the soaking experiments due to slow binding kinetics in the crystalline state compared to **A8**. Alternatively, **A3** and **A6** may occupy multiple binding orientations and thus be rendered invisible in



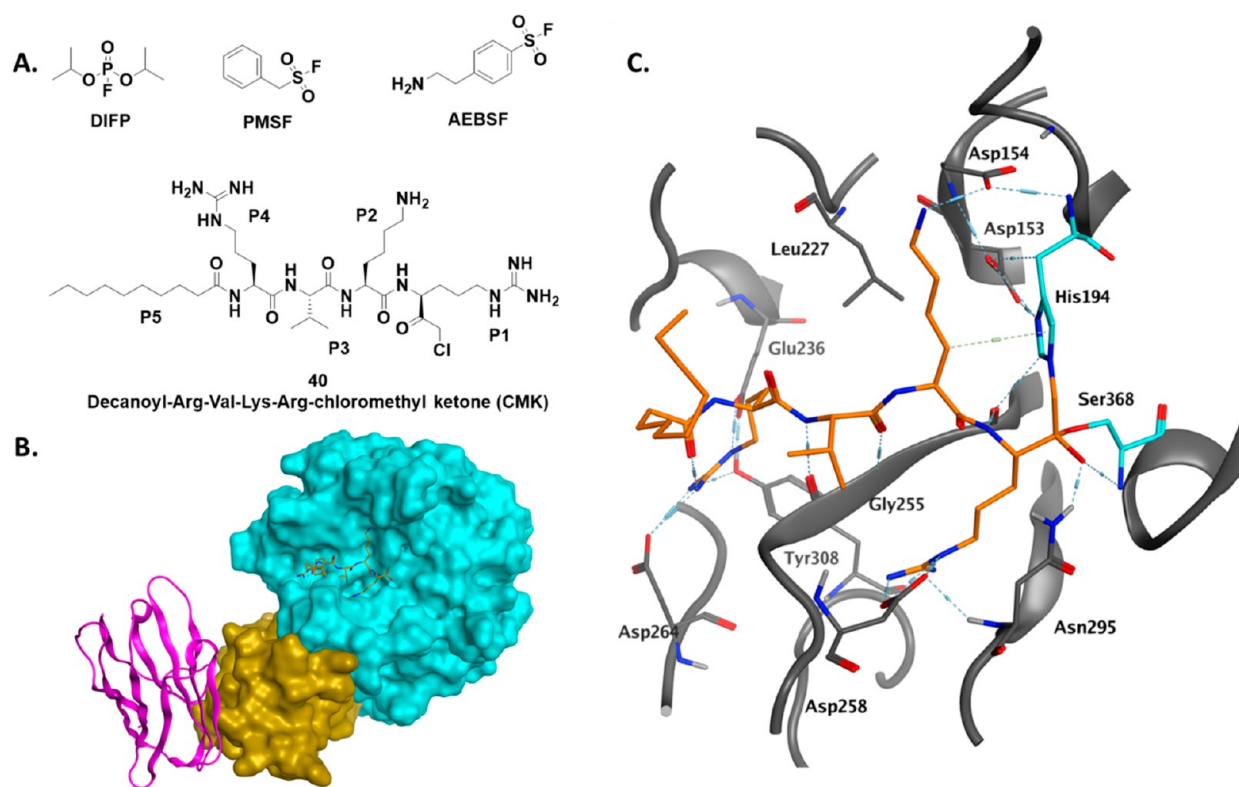


**Figure 21.** (A) Typical covalent inhibitors of serine proteases, DFP and PMSF, that are inactive against furin and the active CMK furin covalent inhibitor 40. (B) The ternary complex of furin (surface display) with the CMK inhibitor 40 (stick display) and the antibody Nb14 (cartoon display) (PDB: 5JMO)<sup>225</sup>. Catalytic domain and SP domain surfaces are shown in cyan and gold, respectively. (C) CMK covalent inhibitor 40 in the catalytic site of furin showing His194 and Ser368 (cyan) forming hemiketal with the inhibitor (orange) and two H-bonds from the side chain of Asn295 and the backbone of Ser368 NH stabilizing the oxyanion tetrahedral hemiketal intermediate.

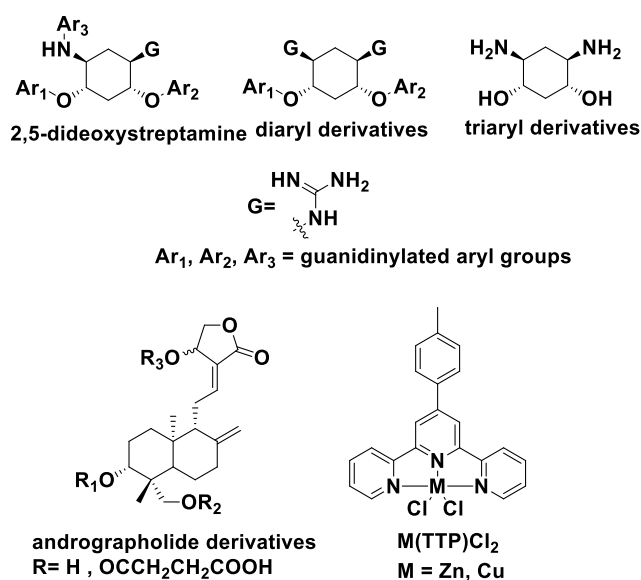
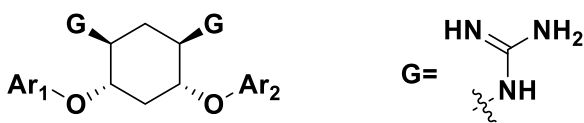


**Figure 22.** General structures of the 2,5-dideoxystreptamine derivatives, andrographolide diterpene derivative and the 4'-[p-tolyl]-2,2':6',2''-terpyridine (TTP) metal complexes.<sup>59,226,227</sup>

the electron density map.<sup>229</sup> Crystals of human furin in complex with A8 solved to 1.9 Å (PDB: 5MIM) showed two molecules of the inhibitor (referred to as A8a and A8b) binding in a well-defined manner at the “northern rim” of the catalytic cleft of furin. The first molecule A8a interferes directly with the catalytic triad, where the second molecule of the

inhibitor A8b binds further “north” (Figure 23). Interestingly, A8a is not interacting with residues at the S1 subsite. Its guanidino-phenoxy moiety forms charged H-bonds to Asp153. The guanidino group adopts a position usually occupied by His194, and consequently, His194 and Ser368 are both reoriented. Ser368, which usually engages in a H-bond to His194, was found to exist in two alternative conformations located at a loose H-bonding distance either to the side chain of the oxyanion hole Asn295 or to the backbone oxygen of Thr365. The other guanidino phenoxy group of A8a forms charged H-bonds to Glu236 and Asp264 as well as a H-bond to Tyr308 at the S4 site of furin (similar to interactions of P4 Arg in peptide-based inhibitors). The two phenyl rings and the cyclohexane core of A8a cover a surface composed of Val231, Leu227, and Trp254 at the bottom of the active site cleft, offering hydrophobic interactions. The guanidino and the guanidino phenylamino moiety on the central cyclohexane ring are both solvent exposed and are not involved in any interaction with furin. These parts are also flexible and hence are not well-defined in the electron density map. The other molecule of the inhibitor A8b is positioned on top of a planar peptide stretch (Asp228-Glu230) and mediates van der Waals interactions to this loop region. The only tight contact of A8b to furin is mediated by its guanidino-phenyl-amino group forming H-bonds to Asp228 and Asn192 at the “northern rim” of S2. While binding of the inhibitor A8b at binding site 2 was suggested to be weaker, as evident from its lower occupancy (0.6 vs 1), cooperative binding cannot be excluded. Another plausible explanation is that the second bound molecule A8b is

Table 6. Guanidino Aryl Derivatives of the Diaryl 2,5-Dideoxystreptamine Derivatives A1–A7 and Their *In Vitro* Furin Inhibition Constants and Cellular Effects<sup>a</sup>



Compd	Ar <sub>1</sub>	Ar <sub>2</sub>	Furin inhibition <i>in vitro</i> K <sub>i</sub> (μM)	% CHO or HT1080 viable cells 100 μM	% Inhibition of intracellular furin 100 μM	% Inhibition of cellular migration 100 μM	% Protection from <i>Pseudomonas</i> toxicity 100 μM	% Protection from anthrax toxicity 100 μM
A1			0.169±0.009	>90	>20	≈60	>70	>80
A2			0.089±0.022	>90	>40	≈30	>30	>80
A3			0.012±0.003	>90	no	no	>20	>90
A4			0.042±0.003	>90	no	no	≈100	≈80
A5			0.404±0.002	>80	≈10	>60	no	≈50
A6			0.006±0.002	>50	≈10	no	≈60	≈90
A7			0.069±0.004	>90	no	≈40	≈30	≈80

<sup>a</sup>K<sub>i</sub> for furin inhibition *in vitro* from Jiao et al.<sup>59</sup> Other data were collected from Ramos et al.<sup>228</sup> and represent approximate estimation from the presented graphs in that paper.

not a “real binder” and was just an artifact of the crystallographic conditions.

**Bis-guanidinophenyl Ether Derivatives.** Bis-guanidinophenyl ether derivatives B1–B6 (Table 7) in which the diguanidincyclohexane scaffold of A1–A8 was replaced by less polar linkers, such as propane, cyclohexane, or benzene, were tested in cell-based assays.<sup>228</sup> These less polar linkers coupled with the lower overall basic character of these inhibitors resulted in much lower furin inhibition *in vitro* with potency in the micromolar range; the most potent inhibitor featured a phenyl ring linker and had a K<sub>i</sub> = 0.4 μM (Table 7). Proteolytic processing of a chimeric substrate was used to assess the effects of A1–A7 and B1–B6 derivatives in the TGN, and inhibition of migration of HT1080 sarcoma cells was used to determine furin-mediated activating cleavage of matrix metalloproteinases within TGN.<sup>228</sup> Inhibition of furin activity in the endocytic pathway and on the cell surface was assessed by measurement of *Pseudomonas* exotoxin A cytotoxicity on CHO-DG44 cells and anthrax cytotoxicity on macrophage RAW264.7 cells, respectively.<sup>228</sup> Moreover, the effect of the synthesized compounds on cell viability was also studied in CHO and HT1080 cells. The findings of this study emphasized the importance of synthesizing compartment specific furin inhibitors and showed that the best correlation between the *in vitro* K<sub>i</sub> values and anti-furin cellular activity was observed for furin functioning on the cell surface.<sup>228</sup>

**Bis-amidinophenyl Ether Derivatives.** Symmetrical amidine-containing guanidinylated 2,5-dideoxystreptamines

and their nonguanidinylated cyclohexane, propane, or benzene derivatives C1–C8 were reported for the treatment of cancer (Table 8 and Figure 24).<sup>230,231</sup> The amidine moiety is less basic compared to guanidine, which may be beneficial in improving the membrane permeability of the inhibitor, but on the negative side, this may also contribute to the lower activity of this series given that furin favors more basic substrates and inhibitors. The most potent derivatives C1 showed K<sub>i</sub> values of 2–20 nM. Additional halo, methyl, or amidine groups on the aryl rings replacement of the phenyl by pyridyl or naphthyl rings resulted in decreased activity (Table 8). Replacement of the two guanidine groups on the cyclohexyl core by amino groups resulted in loss of potency (K<sub>i</sub> = 200–1000 nM).

In the bis-amidinophenyl ether compounds, a cyclohexyl derivative with two amidine substituents on the aromatic ring C7 was more potent (K<sub>i</sub> = 1–5 μM) compared to the mono amidine derivative. The activity of mono amidine derivatives was further reduced by halo or methyl substituents or replacement of the phenyl by pyridyl or naphthyl rings. Replacement of the cyclohexyl ring by smaller cyclopentyl or cyclobutyl rings resulted in reduced activity probably due to the conformational restriction of the linker, consistent with the notion that ethyl, propyl, or butyl linkers were equipotent to the cyclohexyl linker. The C8 inhibitor with phenyl linker was 10 times more potent than its cyclohexyl counterpart C7. Replacement of the ether oxygens by nitrogen seems to have no effect on activity (data not shown). A recent computational study suggested the use of diminazene C9, a bis-amidino-

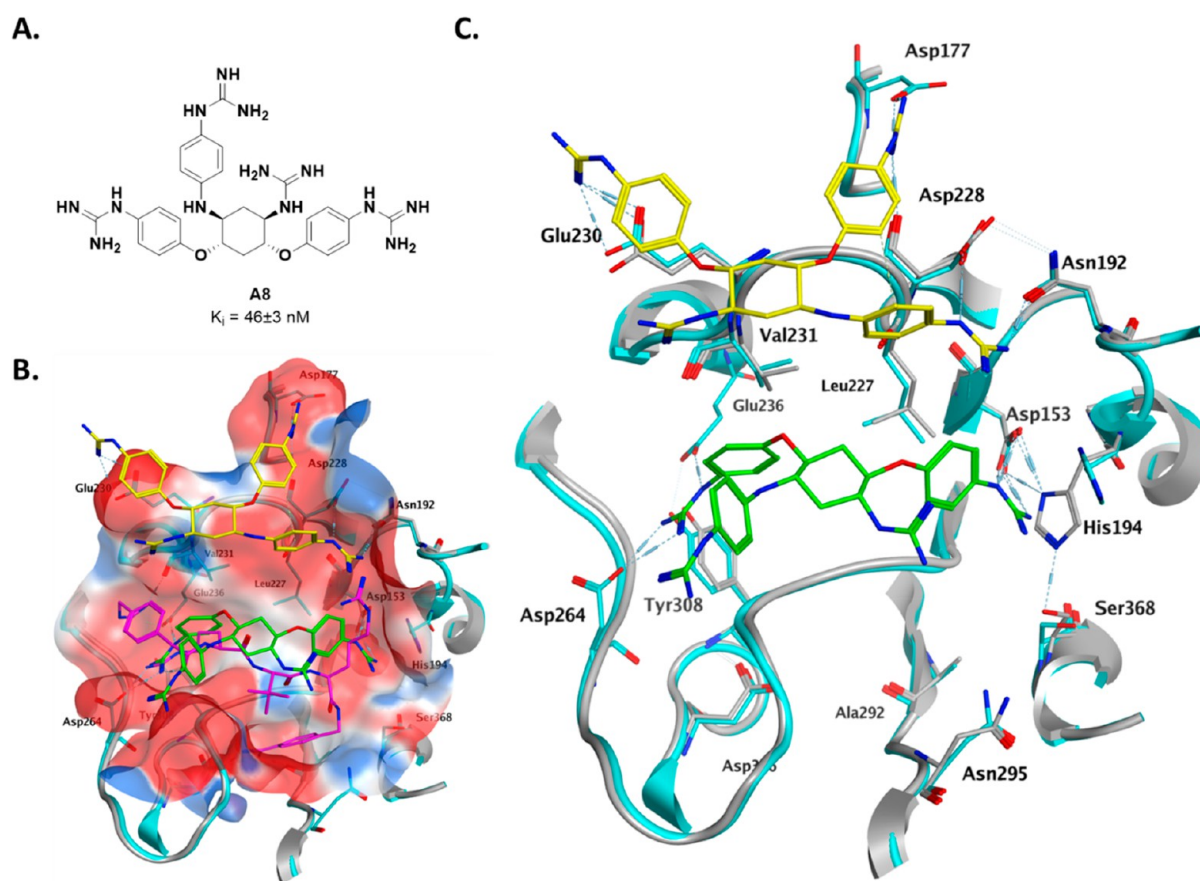


**Figure 23.** (A) Structure of the triaryl 2,5-dideoxystreptamine derivative **A8**. (B) Furin in complex with two molecules of **A8**, designated as **A8a** (green) and **A8b** (yellow) (PDB: 5MIM) superimposed on its complex with the peptide-based inhibitor **1** (magenta) (PDB: 4RYD). A partially transparent electrostatic surface around the ligands is shown. **A8** is not interacting with deep S1 subsite normally occupied by P1 residue in **1**. (C) Interactions of **A8a** and **A8b** with the key amino acid residues of furin. 5MIM structure is overlaid on the enzyme in complex with inhibitor **1** (PDB: 4RYD) to show the reorientation of His194 and Ser368.

phenyl triazine antiparasitic derivative, as a competitive inhibitor of furin ( $IC_{50}$  of  $5.4 \pm 0.1 \mu\text{M}$ ).<sup>232</sup> Diminazene was well fitted within the S1 and S2 subsites of the substrate binding pocket, adopting similar conformation to the P1 and P2 residues of *meta*-guanidinomethyl-Phac-RVR-amba in its crystal structure with furin (PDB: 5JXH) (Figure 24). Asp154, Asp258, and Asp306 in furin were predicted to form three H-bonds with amidine groups of diminazene and hydrophobic interaction with His194, Leu227, and the backbone of Trp254, and Asn295 may further stabilize its binding (Figure 24).

**Amidinohydrazones and Bis-amidinohydrazones.** Amidinohydrazone **D1** ( $K_i = 25.3 \mu\text{M}$ ) was identified through a high-throughput screening campaign (Figure 25).<sup>233</sup> The more potent bisamidinohydrazone **D2** ( $K_i = 1.8 \mu\text{M}$ ) was later identified through screening of several compounds for furin inhibition (Figure 26).<sup>209</sup> Interestingly, **D2** and several close analogues were originally described as trypanocidal agents.<sup>234</sup> While their reduced basicity was claimed to improve their PK profile compared to guanidine and amidine-derived furin inhibitors, hydrazones had several metabolic and chemical stability concerns.<sup>209</sup> Introducing basic moieties to address additional acidic binding sites of furin, as in **D3**, improved the potency of these compounds. Further modifications were later described where *p*-hydroquinone, piperazine, and adipic acid were used as linkers between the aromatic moieties **D4–D6** (Figure 25).<sup>207</sup>  $K_i$  values were in the micromolar range, and the compounds were suggested to act through a mixed inhibition

mechanism. Docking studies revealed interaction with subsites S1 and S4 (and possibly S5), but not with the S2 or S3 subsites of furin.<sup>207</sup> Moreover, the flexible adipic acid linker can reach to subsite S2 of furin, and structure extension of the inhibitor by a substituent with a positive charge was suggested to allow the inhibitors to bind to subsite S2 more efficiently increasing its affinity to furin.<sup>207</sup> The linkers in bisamidinohydrazones were hypothesized to form a sort of “arch” over the binding site, and by attaching a shorter linker at *meta*- (or *ortho*-) positions to amidinohydrazone groups, it may be possible to achieve more efficient interaction between the inhibitor and furin. A closely related series of bisamidinohydrazones were recently reported featuring a 1,3-bisphenoxypropane spacer exemplified by **D7** and **D8** (Figure 25).<sup>208</sup> These compounds were suggested to act through mixed inhibition, but their  $K_i$  values were in the micromolar range.<sup>208</sup>

**Phenylpyridinylmethylpiperidines and Piperazines.** A large series of substituted phenylpyridinylmethylpiperidines, phenylpyridinylmethyl piperazines, and their analogs were reported as furin inhibitors (Figures 26 and 27).<sup>235</sup> Compounds were screened in a cell-free furin enzyme assay as well as image-based platform to evaluate the inhibitory effect of the compounds in a cell-based assay.<sup>235</sup> Many of these compounds showed nanomolar or even picomolar inhibitory activity against furin in a cell-free assay and nanomolar to micromolar inhibition in a cell-based assay. Eighteen selected substituted phenylpyridinylmethylpiperidine derivatives (**E1–**



Table 7. Bis-guanidinophenyl Ether Inhibitors B1–B6 and Their *In Vitro* Furin Inhibition Constants and Cellular Activities<sup>a</sup>

Compound	Linker	Ar	Furin inhibition <i>in vitro</i> K <sub>i</sub> μM	% CHO or HT1080 viable cells 100 μM	% Inhibition of intracellular furin 100 μM	% Inhibition of cellular migration 100 μM	% Protection from Pseudomonas toxicity 100 μM	% Protection from anthrax toxicity 100 μM
B1			8.3	≈60	≈40	<40	no	no
B2			5.5	≈70	≈30	≈40	no	≈30
B3			1.5	>20	≈50	≈90	no	≈70
B4			2.7	>90	<20	<40	<30	≈50
B5			1.2	>90	<20	<40	≈30	≈70
B6			0.4	>60	<20	<20	<40	≈100

<sup>a</sup>Data were collected from Ramos et al.<sup>228</sup>Table 8. Amidino Aryl Derivatives of Guanidinilated 2,5-Dideoxystreptamine C1–C6<sup>230,231</sup>

Compound	Ar	Furin inhibition <i>in vitro</i> K <sub>i</sub> (nM)
C1		2-20
C2		5-25
C3		10-50
C4		20-80
C5		50-100
C6		100-300

E18) were additionally evaluated in a bleomycin-induced lung fibrosis model. Preclinical pulmonary fibrosis was induced by a single installation of bleomycin to the mouse lung to evaluate

compounds for their ability to inhibit TGF- $\beta$  secretion (TGF- $\beta$  assay) and in a collagen deposition mode, also in a mouse lung (hydroxyproline assay) (Table 9). Cellular toxicity was claimed to be determined in parallel; however, no toxicity data were included.

E2 was tested in the transepithelial electrical resistance (TEER) assay, where it showed a concentration-dependent reduction in amiloride-induced increase in transepithelial resistance ( $R_{te}$ ) when compared to controls. E2 was more effective compared to the industry standards, camostat at the same concentration and aprotinin at  $\sim 10 \mu\text{M}$ . Moreover, E2 shows a concentration-dependent attenuation of absorptive fluid transport when compared to negative controls. The higher concentration of  $3 \mu\text{M}$  attenuated total fluid volume loss and rate of fluid loss by 50%. Camostat and aprotinin only attenuated absorptive fluid transport by nearly 50% at the highest concentration of each protease inhibitor tested. E2 at  $3 \mu\text{M}$  and camostat at  $50 \mu\text{M}$  had an equivalent inhibitory effect ( $p < 0.05$ ) on the amiloride-sensitive  $R_{te} \Delta$  (while aprotinin did not) with a chronic overnight treatment. This chemotype is being developed by Boston Pharmaceuticals (BOS) for various infectious diseases.

Interestingly, a recent report disclosed two orally active derivatives namely E9 or BOS-318 and BOS-981 (structure undisclosed) and an inhalable derivative BOS-857 (structure undisclosed) that blocked S1/S2 cleavage in SARS-CoV-2, without affecting the TMPRSS2 processing.<sup>236</sup> Importantly, short-term inhibition of furin did not cause significant side effects in mice, despite the many physiological functions of furin.<sup>236</sup> BOS series of compounds appear to represent a nontoxic, small-molecule class of inhibitors that can be delivered orally or by inhalation. Therefore, further testing for their antiviral effect against acute SARS-CoV-2 infection either alone or in combination with TMPRSS2-inhibitors is

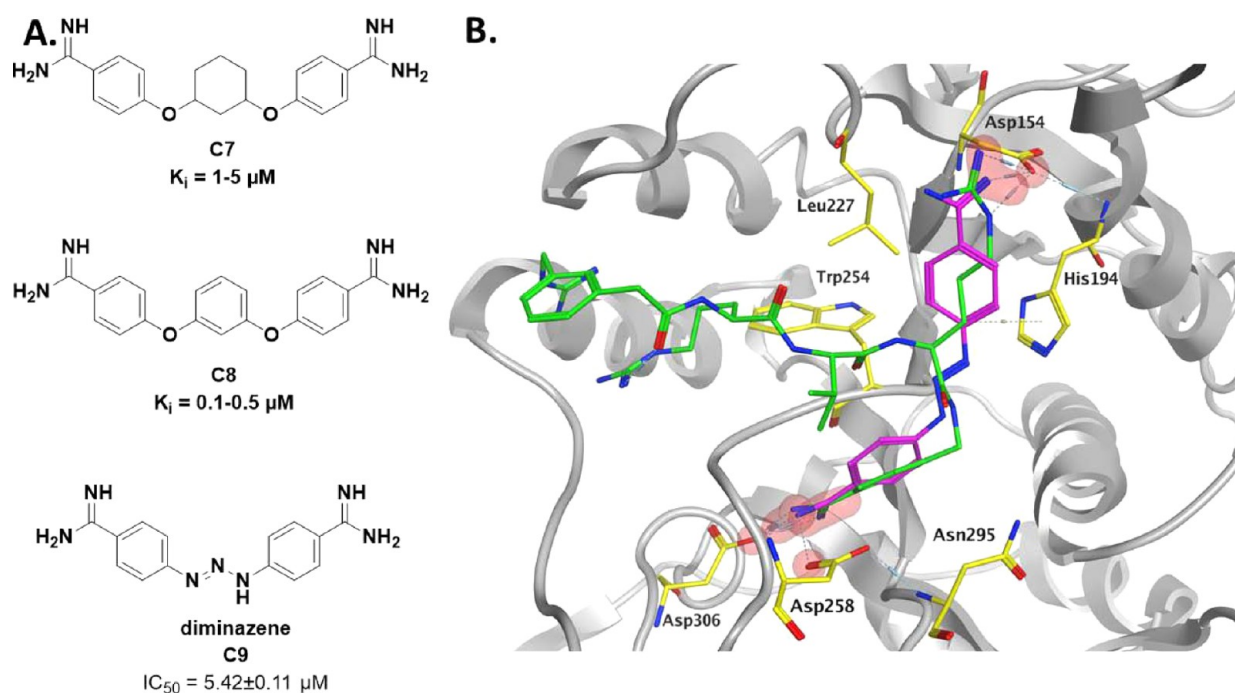


**Figure 24.** (A) Bis-amidinophenyl ether compounds C7 and C8 and diminazene C9. (B) Docking pose of diminazene C9 (magenta) at furin substrate binding site complex with meta-guanidinomethyl-Phac-RVR-amba (green) (PDB: 5JXH)<sup>74</sup>. Residues contributing to the binding of C9 are in yellow.

warranted. This novel class of furin inhibitors represents an interesting starting point for additional medicinal chemistry campaigns through ligand- and structure-based drug design approaches. The BOS compounds contain several basic moieties that would be positively charged at physiological pH. Many of these groups are relatively weakly basic as predicted from their calculated  $pK_a$  values (Table 9), which may partly explain the oral bioavailability of some analogues from this series. The basic moieties in peptide and nonpeptide furin inhibitors are important for binding to the extended canyon-shaped substrate binding groove with several negatively charged acidic residues. Surprisingly, many of the reported BOS inhibitors contain carboxylic acid functionalities. This may point to a different binding mode where the negatively charged carboxylate anion of the inhibitors interacts with some positively charged or H-bond-donor amino acids in the active site of furin. The possible electronic repulsion with the negatively charged amino acids in the substrate binding site of furin would exclude binding of the acid moiety to all the S1–S6 subsites, except S3 where no acid residues are located (Figure 5). A plausible binding mode would be the interaction of the carboxylate anion with the positively charged basic residues Arg193, Arg197, and His364 at the outer edge of the S1' subsite (Figure 28). Interestingly, in this binding mode, the dichlorophenyl moiety of this chemotype occupies the entrance of the deep S1 pocket, making interaction with Ser368 and Asp306 through the two chlorine atoms, and the central pyridine scaffold is occupying S3 subsite (Figure 28). Another possibility is the interaction of the acid in the inhibitor with Arg185 and/or Arg225 close to Asp228, where the second molecule of the 2,5-dideoxystreptamine derivative A8 is binding.

**Miscellaneous Small-Molecule Furin Inhibitors.** Sulconazole F1 (Figure 29), a broad-spectrum antifungal agent, was identified as a furin inhibitor through structure-based *in silico*

screening of about 8000 approved and investigational drugs.<sup>237</sup>

In Western blot analysis, sulconazole inhibited the cleavage of the cell surface furin substrate membrane type 1-matrix metalloproteinase (MT1-MMP) that contains two furin cleavage sites similar to those of the SARS-CoV-2 spike protein. Its small size and the lack of positively ionizable groups distinguish this compound from other small-molecules furin inhibitors. However, sulconazole was not tested in a biochemical assay for furin inhibition, and thus no  $K_i$  value was provided. A docking pose was proposed where the imidazole ring could form a H-bond with Asp154, and the 4-chlorophenyl and 2,4-dichlorophenyl moieties occupy the S1 and S3 subsites, respectively. Similarly, HIV protease inhibitors, nelfinavir F2 and tipranavir F3 (Figure 29), were suggested to inhibit furin proteolytic cleavage of hepcidin for the treatment of anemia of chronic inflammation.<sup>238</sup> A series of 1,3-oxazol-4-ylphosphonium salts containing variable electron withdrawing or electron-donating groups at C2 and C5 were recently described (Figure 29).<sup>239</sup> The synthesized compounds inactivated furin at the high micromolar range through competitive, noncompetitive, or mixed inhibition. 2-(2,4-Dichlorophenyl)-5-methylthio derivative F4 was the most active ( $K_i = 1.57 \mu\text{M}$ ).<sup>239</sup> These compounds showed antiviral activity against low-risk human papillomavirus 1 (HPV-1) ( $\text{IC}_{50} = 1.7\text{--}9.6 \mu\text{M}$ ) in a transient DNA replication assay and low cytotoxicity in HEK293 cells compared to the clinically used antiviral cidofovir.<sup>239</sup>

Finally, a fluorescent-based high-throughput biochemical screen of 220,222 compounds identified 134 active compounds as furin inhibitors (PubMed BioAssay AID: 463180 and 463182). A follow up confirmatory assay with 90 compounds confirmed the activity of 9 compounds. Dose–response curve confirmation assays identified two structurally related compounds G1 and G2 with  $\text{IC}_{50}$  of 33.8 and 31.5  $\mu\text{M}$ , respectively (Figure 30). The small size, poor drug-like properties, and

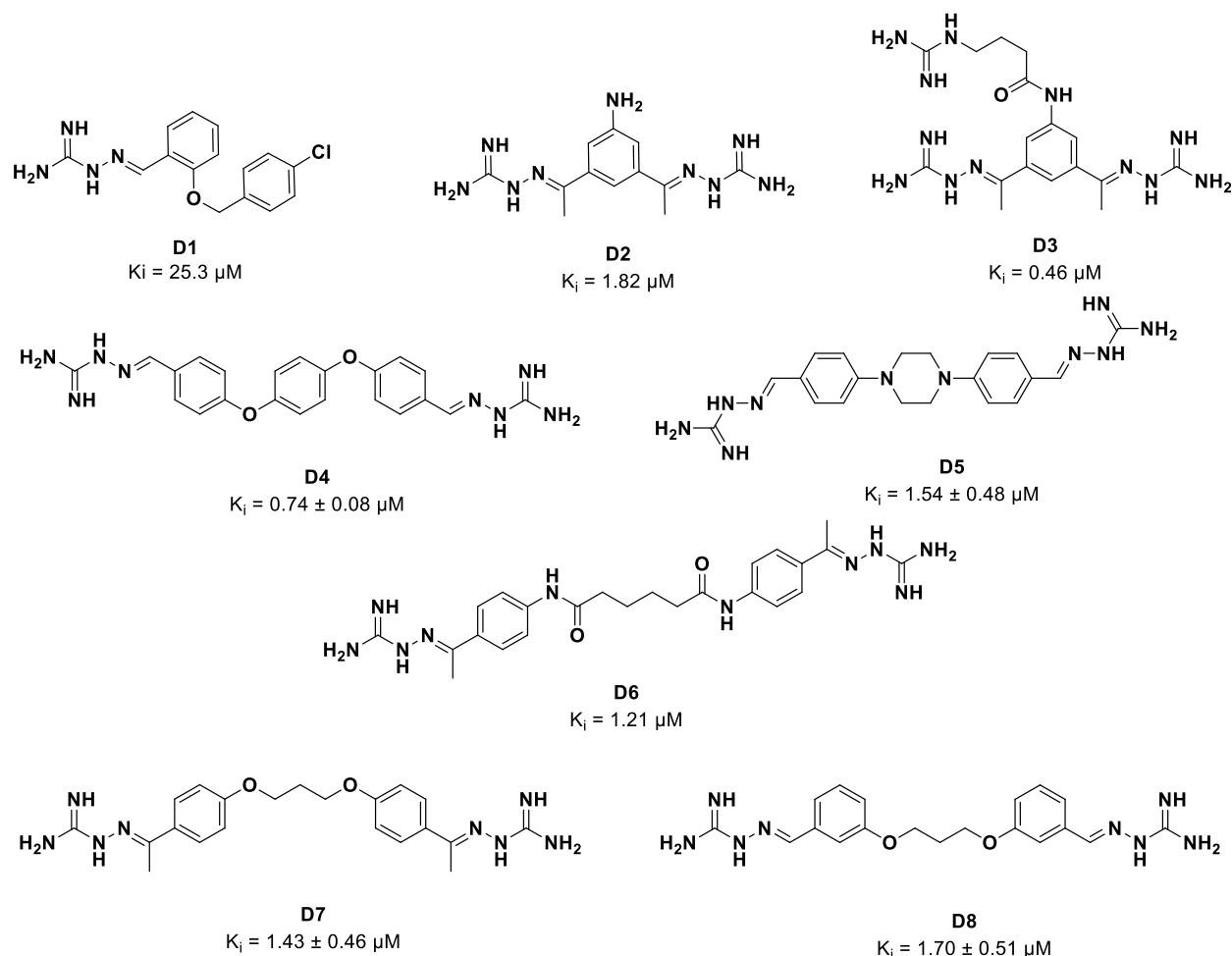


Figure 25. Structures of amidinohydrazone **D1** and bisamidinohydrazones **D2–D8**.<sup>207–209,233</sup>

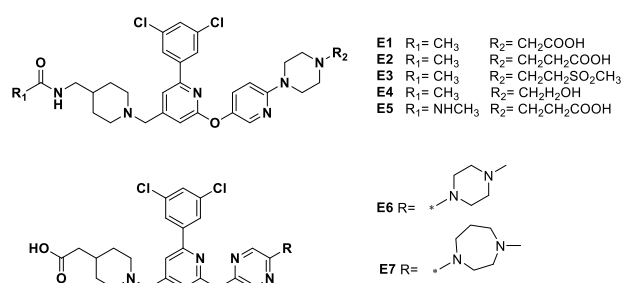


Figure 26. Structures of substituted pyridyloxy derivatives **E1–E5** and pyrazinyloxy phenylpyridinyl methylpiperidine derivatives **E6** and **E7**.<sup>235</sup>

geometrical isomerism make these compounds less interesting from a medicinal chemistry point of view. Definitely, there is still great need to identify novel potent drug-like small-molecule inhibitors of furin.

### FURIN CRYSTAL STRUCTURES

The first homology model of the catalytic domain of the human furin and its interaction with model substrates was published in 1994.<sup>55</sup> This model was based on the crystal structures of the bacterial subtilisin BPN' and thermitase in complex with the inhibitor eglin.<sup>55</sup> About 9 years later, the cocystal structure of a truncated preparation of heterogeneous

glycosylated mouse furin ectodomain produced in CHO cells in complex with the covalent inhibitor decanoyl-Arg-Val-Lys-Arg-chloromethylketone (dec-RVKR-CMK) (PDB: 1P8J) was the first solved eukaryotic PC structure.<sup>57</sup> In 2014, the first human furin cocystals in complex with two competitive noncovalent inhibitors Phac-RVR-4-amba (PDB: 4OMD) and its *meta*-guanidinomethyl derivative (PDB: 4OMC) were reported.<sup>60</sup> Currently, there is a total of 24 X-ray crystal structures in the Protein Data Bank (PDB) for the human furin sequence (Uniprot Acc.: P09958), 23 of which were determined by S. Dahms from the Than group, most of them in complex with synthetic substrate-analogue inhibitors from the Steinmetzer lab (Table 10). Analysis of these crystal structures revealed that most of them are monomeric crystals with resolution of  $\leq 2 \text{ \AA}$  and three have hexameric quaternary structures with resolution of  $>2 \text{ \AA}$  (PDB: 4RYD, 4OMC, 4OMD) and one is solved as a dimer with resolution of  $\approx 2 \text{ \AA}$  (PDB: 5JMO). Among these 24 structures, three entries represent the unliganded apo furin structure (PDB: 4Z2A,<sup>85</sup> 5JXI and 5JXG<sup>74</sup>), one structure for furin in ternary complex with an antibody and the CMK covalent inhibitor (PDB: 5JMO),<sup>225</sup> and another cocystal with the unique nonpeptide small-molecule inhibitor 2,5-dideoxystreptamine derivative **A8** (PDB: 5MIM).<sup>229</sup> The remaining 19 furin cocystals are all bound to peptidomimetic inhibitors, 12 of which are noncyclic and 7 are cyclic inhibitors with variable ring sizes. In three of the cyclic inhibitors, electron density was clear for the entire



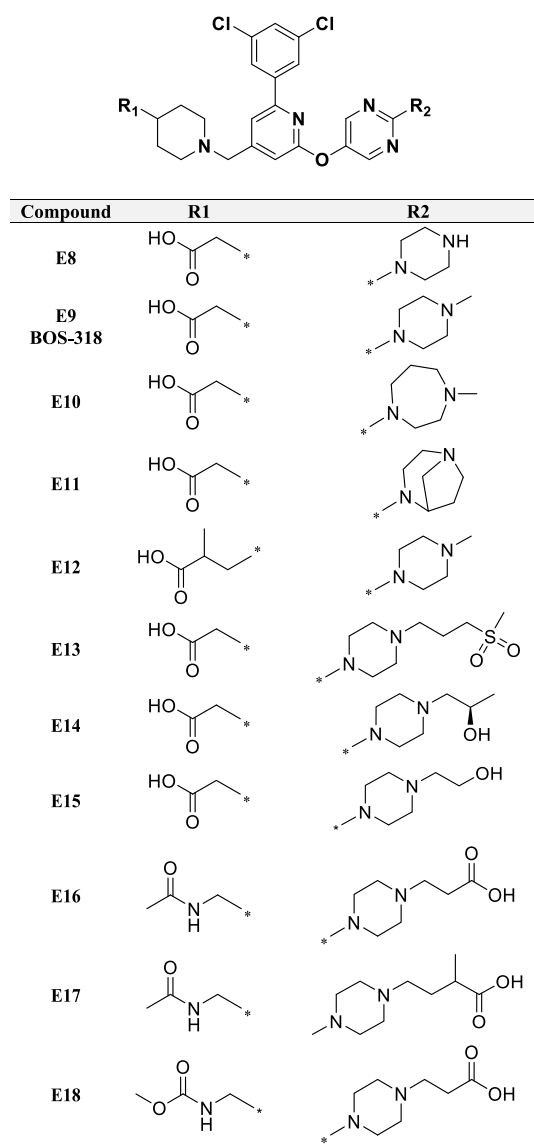


**Figure 27.** Structures of substituted pyrimidinyloxy phenylpyridinyl methylpiperidine derivatives **E8–E18**.<sup>255</sup>

inhibitor (PDB: 6HZA, 6HZB and 6HZD).<sup>206</sup> In the other cases, the structures could be determined only for the P6/P5–P1 segments directly interacting with furin, probably due to the high flexibility of their solvent exposed segments. The 4-amidino methyl benzamide (4-amba) represents exclusively the P1 residue in all the 19 peptidomimetic-based inhibitors where Arg is featured as the P2 residue in almost all the noncyclic inhibitors and Arg or Lys in the cyclic ones. P3 is valine in the noncyclic derivatives except in 4-guanidinomethyl-Phac-R-Tle-R-4-amba **1** (PDB: 4RYD) and the four recently solved canavanine containing inhibitors where it is the bulkier Tle. The basic lysine represents P3 in the cyclic derivatives except in PDB: 6HZC and 6HLE. P4 is almost exclusively Arg except in PDB: 6EQV where the basic guanidine moiety of arginine was replaced by the nonbasic urea to give citrulline or in the recently reported crystal structures featuring canavanine (PDB: 6YD3, 6YD4, and 6YD2). For P5, basic arginine was found in most of the structures, except for 4-aminomethyl or 3 or 4-guanidinomethyl substituted phenylacetyl (Phac) in 9 structures and the nonbasic Phac in 2 structures and the

decanoyl in the CMK-based covalent inhibitor in (PDB: 5JMO). P6 was featured in all the cyclic structures and in only one noncyclic structure (6EQX). P6 is mostly Arg, except in three cocrystal structures. Finally, P7 is found in only one cyclic structure (PDB: 6HLB).

We aligned all the crystal structures and generated a pairwise RMSD matrix with an average of 0.294 Å for the  $\alpha$  carbons of the common 465 residues (Supplemental Figure 3). While almost all the structures had an interstructure RMSD of <0.5, only the unliganded crystal (PDB: 4Z2A) showed an RMSD > 0.5. It is worth mentioning that all the 24 crystal structures represent the glycosylated soluble form of the wild-type furin with the exception of the 1.89 Å crystal of the unglycosylated apo-furin (PDB: 4Z2A) that contains a glycosylation site double-mutant N387D and N440D.<sup>85</sup> Nevertheless, the PDB: 4Z2A crystal structure superimposes well with the recently reported apo, glycosylated structure (PDB: 5JXG). Several residues located on the surface displayed an RMSD > 1.0 Å. This includes Tyr110 at the N-terminal and residues 125–127, 188, 189, and 405 in the catalytic domain and 440 and 558 in the P domain. While these differences are likely to be due to crystal packing, the catalytic triad residue His194 showed obvious rotameric differences (rotation by about 120°) similar to those seen in a furin cocrystal with the 2,5-dideoxystreptamine derivative (PDB: 5MIM).<sup>85</sup> Previous X-ray crystallography and molecular modeling studies suggested activation of furin by a substrate-induced mechanism and highlighted the role of calcium in furin's catalytic activity.<sup>74</sup> Comparison of unliganded (PDB: 5JXG) and inhibitor-bound furin (PDB: 5JXH) revealed subtle conformational differences at or around the catalytic residues His194, Ser368, the oxyanion hole Asn295, Na<sup>+</sup> binding site (Thr309 and Ser316), as well as alignment template residues in direct contact with the inhibitor (Ser253-Pro256) (Figure 31 and Supplemental Figure 4). In the unliganded structure of furin (PDB: 5JXG), the side chain of Ser368 is rotated 180° away from the S1 pocket disrupting the essential H-bond to His194, altering the interaction geometry of the catalytic triad and thus disabling substrate processing. In the ligand bound state, the side chain of Ser368 is properly positioned for nucleophilic attack at the scissile peptide bond. The H-bond between Ser253-OH and the backbone O of Ser368 appears to facilitate the reorientation of Ser368 in liganded furin (Figure 31).<sup>74</sup> The rotameric state of Asn295 seems to be identical in the unliganded and the ligand-bound forms as long as Ca<sup>2+</sup>(II) is bound (Figure 31). Asn295 consequently influences the active-site geometry, explaining the strict calcium dependence of furin and other PCs.

A specific conformation of the aligned template residues (Ser253-Pro256) needs to be adopted in the ligand bound state of furin to enable its characteristic  $\beta$ -sheet-like interaction pattern at Gly255 and recognition of P1 side chain (Figure 31).<sup>74</sup> This will avoid steric clashes between ligand and the enzyme at P1 and P4. In the unliganded furin structure, the catalytic residues and the substrate-binding region adopt an inactive conformation referred to as “off state”.<sup>74</sup> Upon binding of the substrates or canonical inhibitors, the enzyme switches to a catalytically active “on state” conformation.<sup>74</sup> Removal of Ca<sup>2+</sup> at the binding site II by EDTA changes the rotamer state of the oxyanion hole Asn295 (PDB: 5JXI and 5JXJ) (Figure 32).<sup>74</sup> Moreover, in the unliganded Ca removed structure, the sodium ion is in the preferred octahedral coordination state by the backbone oxygens of Thr309, Ser311, and Thr314, the hydroxyls of Thr314 and Ser316, as well as a water molecule.<sup>74</sup>

**Table 9.** pIC<sub>50</sub> and pX<sub>50</sub> of E1–E18 against Furin in Cell-Free and Cell-Based *In Vitro* and Their Effects on Mouse Lung TGF-β and Hydroxyproline Content in the Bleomycin-Induced Lung Fibrosis Mouse Model<sup>235</sup>

compound	furin enzyme pIC <sub>50</sub>	cell-based furin inhibition pXC <sub>50</sub>	dose (mg/kg), route, frequency	% inhibition of total TGF-β in lung <sup>a</sup>	% inhibition of hydroxyproline in lung <sup>a</sup>	calculated pK <sub>a</sub> <sup>b</sup>
E1	8.7	6.9	10, IP, twice	43*	16	8.21
E2	9.6	7.6	10, IP, twice	69*	67*	7.51
E3	8.3	7.6	30, oral, once	41*	45*	8.53
E4	9.1	8.5	10, IP, once	60*	56*	7.39
E5	9.1	7.6	10, IP, once	67*	39*	7.51
E6	8.7	7.3	10, oral, once	22	4	7.97
E7	8.8	7.7	30, oral, once	26*	21*	8.36
E8	8.6	7.6	10, oral, once	-11	6	7.79
E9 BOS-318	9.1	7.8	10, oral, once	66*	46*	7.81
E10	9.0	8.2	30, oral, once	34*	36*	8.31
E11	8.9	7.7	30, oral, once	36*	34*	7.49
E12	9.1	8.0	10, oral, once	81*	54*	7.82
E13	8.6	7.6	10, oral, once	40*	-1	7.03
E14	9.2	7.7	10, oral, once	23*	16*	7.32
E15	8.9	7.6	10, oral, once	31*	11	7.17
E16	9.8	8.0	10, IP, twice	86*	60*	7.24
E17	9.3	8.3	10, oral, once	75*	62*	7.61
E18	9.8	7.5	30, oral, once	7	-14	7.23

<sup>a</sup>% Inhibition is reported relative to levels induced by bleomycin in vehicle treated animals (\**p* < 0.05 (*t* test)). <sup>b</sup>Calculated using MOE software.

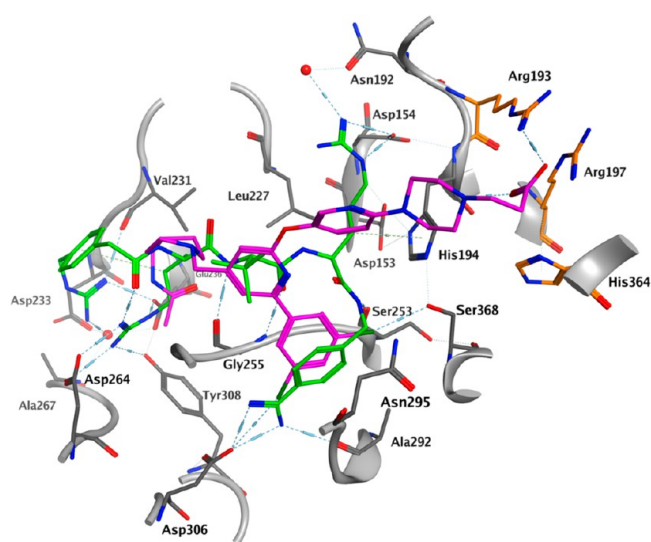


**Figure 28.** Docking pose of E2 (magenta) at furin substrate binding site in complex with 1 (green) (PDB: 4RYD)<sup>212</sup>. The acid moiety of E2 is interacting with basic amino acids Arg193, Arg197, and His364 (orange) at the outer edge of the S1' subsite.

The coordination changes to a tetragonal-pyramidal geometry upon ligand binding, whereupon the side-chain rotations of Ser316 and Thr309 result in breakage of the coordinate bond to the sodium ion and loss of the H-bond between these residues.<sup>74</sup> This suggests a switch from a lower (unliganded) to a higher (liganded) energy state. All these crystal structures provide an excellent opportunity for both structure and ligand-based drug discovery campaigns.

### FURIN INHIBITORS IN CLINICAL TRIALS

Despite evidence of *in vivo* efficacy and safety in preclinical studies, no small-molecule furin inhibitor is currently in clinical development (Table S1). Furin knockdown for the generation of an autologous cancer vaccine, where cancer cells sampled from a patient's tumor are genetically modified and re injected,

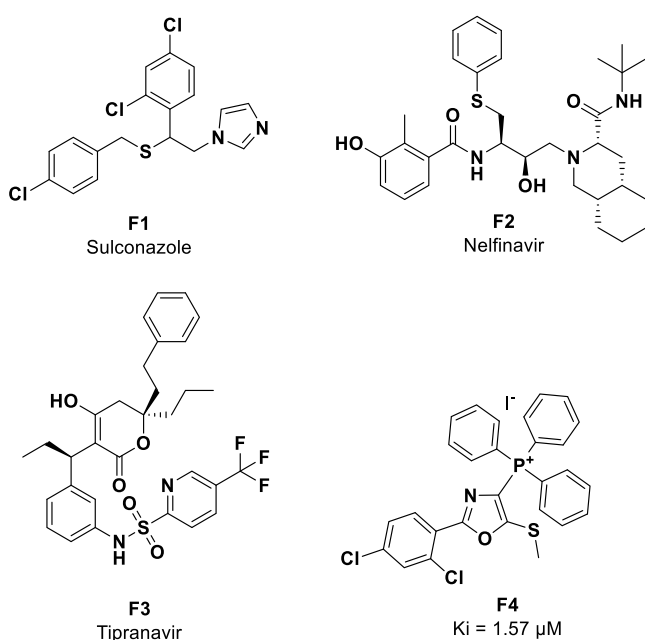


**Figure 29.** Structures of F1–F4.<sup>237–239</sup>

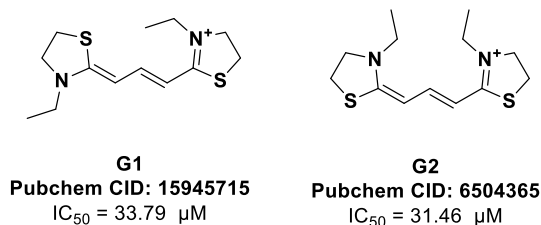


**Figure 30.** Structures of furin inhibitors identified in high-throughput screening assays.

represents the most advanced application (8 clinical trials out of 17 related to furin). Using a bifunctional shRNA, furin knockdown, and GM-CSF augmented (FANG) cancer vaccine

Table 10. Select Properties of Human Furin Crystal Structures in the Protein Data Bank

PDB ID	resolution	state	4° structure	ligand	remarks	refs
6YD7	1.8	cocrystal	monomer	4-guanidinomethyl-phenylacetyl-Arg-Tle-Canv-4-amba	less basic canavanine as P2 and/or P4 residue	205
6YD3	2.0	cocrystal	monomer	4-guanidinomethyl-phenylacetyl-Canv-Tle-Arg-4-amba		
6YD4	1.7	cocrystal	monomer	4-guanidinomethyl-phenylacetyl-Canv-Tle-Canv-4-amba		
6YD2	1.8	cocrystal	monomer	4-aminomethyl-phenylacetyl-Canv-Tle-Arg-4-amba		
4Z2A	1.89	unglycosylated apo	monomer	none	the only nonglycosylated structure his194 is rotated	85
6HZA	1.9	cocrystal	monomer	c[glutaryl-Arg-Arg-Lys]-Arg-4-amba	the structure was determined for the whole inhibitor; the cyclization linker is solvent exposed	206
6HZB	1.9	cocrystal	monomer	c[glutaryl-Arg-Arg-Lys]-Lys-4-amba		
6HZD	1.9	cocrystal	monomer	c[glutaryl-Arg-Arg-Arg-Lys]-Arg-4-amba		
6HZC	1.9	cocrystal	monomer	c[glutaryl-BVK-Lys-Arg-Arg-Tle-Lys]-4-Amba	ligand structure could be determined only for the P6/P5-P1 segment	
6HLB	2.0	cocrystal	monomer	c[succinyl-Phe-2-Nal-(Arg)4-Lys]-Arg-4-amba		
6HLD	2.1	cocrystal	monomer	c[succinyl-Phe-2-Nal-(Arg)3-Lys]-Lys-4-amba		
6HLE	1.994	cocrystal	monomer	P6-P2-cyclized peptide H-Lys-Arg-Arg-Tle-Lys-4-amba		
6EQV	1.895	cocrystal	monomer	Phac-Cit-Val-Arg-4-amba	the significance of the H-bond network at S4	214
6EQW	1.994	cocrystal	monomer	4-aminomethyl-phenylacetyl-Arg-Val-Arg-Amba	importance of extended basic groups at P5	
6EQX	1.994	cocrystal	monomer	Arg-Arg-Arg-Val-Arg-Amba	elongated inhibitor adopted turn-like structure	
5MIM	1.9	cocrystal	monomer	2,5-dideoxystreptamine derived small-molecule inhibitor	the only nonpeptide based crystallized inhibitor; His194 is rotated	229
SJMO	1.998	cocrystal	dimer	antibody Nb14 and chloromethyl ketone covalent inhibitor	furin antibody is binding away from the substrate binding site; the covalent inhibitor binds the catalytic triad	225
SJXG	1.8	unliganded apo	monomer	none	role of Ca <sup>2+</sup> in furin's catalytic activity; activation by substrate induced mechanism	74
SJXH	2	cocrystal	monomer	3-guanidinomethyl-Phac-Arg-Val-Arg-4-amba		
SJXI	2	unliganded apo (EDTA)	monomer	none		
SJXJ	2	cocrystal (EDTA)	monomer	3-guanidinomethyl-Phac-Arg-Val-Arg-4-amba		
4RYD	2.15	cocrystal	hexamer	4-guanidinomethyl-Phac-Arg-Tle-Arg-4-amba	the most potent furin inhibitor to date	212
4OMC	2	cocrystal	hexamer	3-guanidinomethyl-Phac-Arg-Val-Arg-4-amba	importance of basic groups at P5	60
4OMD	2.1	cocrystal	hexamer	Phac-Arg-Val-Arg-4-amba		

was thought to induce an antitumoral response.<sup>210</sup> GM-CSF expression enhances the recruitment of dendritic cells and further primes T-cells to raise an antitumoral response.<sup>210</sup> Overexpression of TGF- $\beta$  by cancer cells appears to mediate immunosuppressive properties and counteracts the GM-CSF-mediated response.<sup>210</sup> Safety of FANG vaccine was demonstrated in a Phase I clinical trial (NCT01061840), and both short-term immune response and long-term follow-up suggest a favorable safety profile and higher survival rate, almost doubling the survival median. Several Phase II clinical trials of the FANG vaccine to fully assess vaccine efficacy and safety, notably in melanoma, colorectal, and gynecological cancers, are ongoing.<sup>240</sup> A Phase III trial (NCT03495921) was initiated in 2018 to evaluate the autologous vaccine in Ewing sarcoma and connective and soft tissue neoplasms. Other furin-related clinical trials involve measurement of the level of antibodies to recombinant furin to assess the safety of several therapeutic interventions in hematological disorders including recombinant von Willebrand Factor (r-VWF) or r-FIX in von Willebrand Disease and Hemophilia B (Supplemental Table

1). Clinical trial NCT04550338 describes the repurposing of tranexamic acid as an antiviral agent against SARS-CoV-2 based on its inhibitory effect on the formation of the endogenous protease plasmin. Plasmin was proposed to act on SARS-CoV-2 by cleaving the furin cleavage site in the S protein portion of the virus, resulting in increased infectivity and virulence.

## SUMMARY AND FUTURE PERSPECTIVES

Since its discovery, isolation, and characterization in the 1980s, furin has become an attractive target for the treatment of various infectious and non-infectious diseases and conditions given its regulatory function on numerous bacterial and viral as well as mammalian targets. The discovery of a furin cleavage site in the spike protein of SARS-CoV-2 virus peaked interest in research on this enzyme due to its potential role in the infectivity and virulence of the virus in the ongoing pandemic. The availability of several peptide and nonpeptide inhibitors served to implicate its role in blocking the activation of bacterial toxins, the maturation of viral proteins, and the



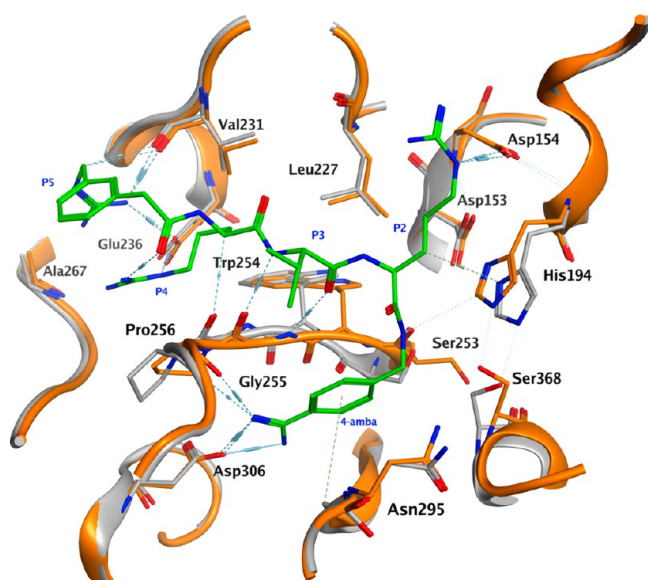


**Figure 31.** 3D alignment of unliganded (PDB: 5JXG,<sup>74</sup> gray) and liganded furin (5JXH,<sup>74</sup> orange). Residues are shown in stick rendering. The ligand is shown in green.

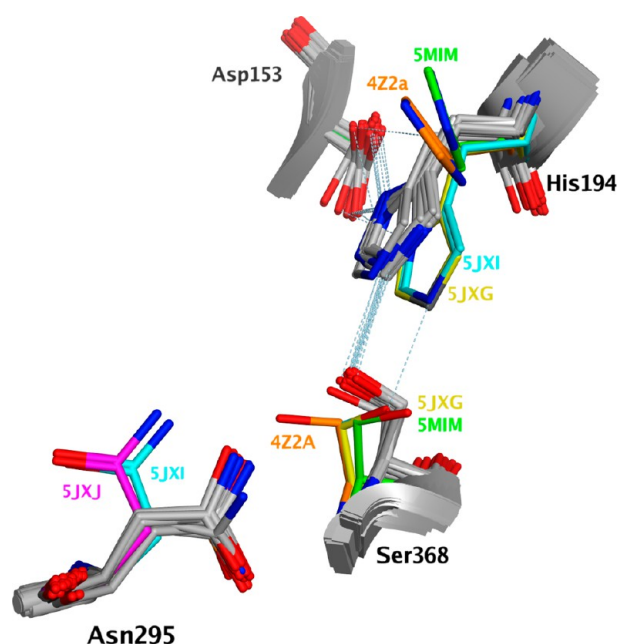


**Figure 32.** Alignment of the residues of the catalytic triad (Asp153, His194, and Ser368) and the oxyanion hole (Asn295) from 24 crystal structures of human furin. The residues are in gray except for 5JXG: unliganded furin (gold), 5JXI: unliganded furin in the presence of EDTA (cyan), 5JXJ: furin in complex with 3-guanidinomethyl-Phac-RVR-4-amba in the presence of EDTA (magenta), 5MIM: furin in complex with 2,5-dideoxystreptamine derivative A8 (green), and 4Z2A: unglycosylated unliganded furin (orange). Hydrogen atoms were removed for clarity.

suppression of tumor growth *in vitro*. Despite promising results in animal models, only a limited number of clinical trials in humans have been initiated and were based exclusively on furin knockdown using autologous vaccines for cancer treatment. Challenges related to the ubiquitous expression of furin and its redundancy with other related PC family members call for more efforts to achieve selective inhibition of this enzyme to

limit unwanted side effects especially with long-term use. Nevertheless, short-term systemic treatment with furin inhibitors in model systems seem well tolerated. Local applications for bacterial and viral infections may also represent a more feasible and safe option. The difficulty associated with developing peptide-based furin inhibitors into clinical candidates make nonpeptide small-molecule inhibitors more attractive due to their favorable drug likeness profiles. The availability of more than 20 high quality X-ray crystal structures opens the door wide for vast opportunities in the development of clinical candidates by providing useful information about the pharmacophoric and structural requirements of potential inhibitors for various structure and ligand-based drug discovery campaigns. The recent discovery of nonpeptide drug-like small-molecule chemotypes exemplified by the BOS compounds represents an interesting starting point and encourages the quest for more novel inhibitors. A deeper understanding of the contribution of individual PC family members in proteolytic protein processing and the study of the possibility of developing resistance to proteolytic cleavage by furin in cancer cells or pathogens would pave the way for the successful clinical use of furin inhibitors and might also suggest additional targets or indications for therapeutic intervention. Collectively, while the route to a successful therapeutic application of furin inhibitors may not be that straightforward, it is certainly a promising approach that deserves to be further pursued.

## ■ ASSOCIATED CONTENT

### Supporting Information

The Supporting Information is available free of charge at <https://pubs.acs.org/doi/10.1021/acs.jmedchem.1c00518>.

A list of proprotein convertase family members, gene expression of furin, death rates of COVID-19 patients with preexisting comorbidities, clinical trials related to furin, and pairwise alignment matrix for the backbone  $\alpha$  carbon atoms of the 465 common residues of 24 crystal structures of furin (PDF)

## ■ AUTHOR INFORMATION

### Corresponding Author

Nouri Neamati – Department of Medicinal Chemistry, College of Pharmacy, Rogel Cancer Center, University of Michigan, Ann Arbor, Michigan 48109, United States; [orcid.org/0000-0003-3291-7131](https://orcid.org/0000-0003-3291-7131); Email: [neamati@umich.edu](mailto:neamati@umich.edu)

### Authors

Essam Eldin A. Osman – Department of Medicinal Chemistry, College of Pharmacy, Rogel Cancer Center, University of Michigan, Ann Arbor, Michigan 48109, United States; Department of Pharmaceutical Chemistry, Faculty of Pharmacy, Cairo University, Cairo 11562, Egypt; [orcid.org/0000-0002-0768-9862](https://orcid.org/0000-0002-0768-9862)

Alnawaz Rehemtulla – Department of Radiation Oncology, University of Michigan, Ann Arbor, Michigan 48109, United States

Complete contact information is available at:

<https://pubs.acs.org/10.1021/acs.jmedchem.1c00518>

### Notes

The authors declare no competing financial interest.

## Biographies

**Essam Eldin A. Osman** obtained his B.Sc. degree in Pharmaceutical Sciences from Faculty of Pharmacy, Cairo University in 2000. He received his Ph.D. in Pharmaceutical Chemistry under the supervision of Prof. Samir El Moghazy. He was appointed as an Assistant Professor in 2014 at the Department of Pharmaceutical Chemistry, Faculty of Pharmacy, Cairo University and was promoted to an Associate Professor in 2020. Since 2018, he has been working as a visiting assistant research scientist in Prof. Nouri Neamati's laboratory at the College of Pharmacy, University of Michigan, Ann Arbor. His research interests mainly focus on the design, and synthesis of novel small-molecule cancer therapeutics.

**Alnawaz Rehemtulla** is a Ruth Tuttle Freeman Professor in the Department of Radiation Oncology at the University of Michigan Medical School. He obtained his Ph.D. from the University of Calgary, followed by a fellowship at the Scripps Research Institute in La Jolla, and then joined the Genetics Institute in Cambridge, MA, as staff scientist. He has been at the University of Michigan for two decades, where his research effort has been in radiation biology and the development of imaging technologies for studies in cell and mouse models.

**Nouri Neamati** is a John G. Searle Professor of Medicinal Chemistry at the College of Pharmacy, University of Michigan. He obtained his Ph.D. in Biomedical Sciences from the University of Texas Graduate School of Biomedical Sciences and MD Anderson Cancer Center, Houston, Texas, in 1995. From 1995 to 2000, he was a postdoctoral and a research fellow at the National Institutes of Health. In September 2000, he joined the University of Southern California, School of Pharmacy, and rose through the ranks to full Professor in 2011. In 2013, he moved to the Department of Medicinal Chemistry, University of Michigan. He has published >270 peer-reviewed manuscripts, 20 book chapters, and over 40 patents in different areas of drug design and discovery.

## ACKNOWLEDGMENTS

We are grateful to Dr. Peter L. Toogood for critical reading of the manuscript and providing valuable suggestions.

## ABBREVIATIONS USED

A, active domain; ACE2, angiotensin converting enzyme 2; ADAM, a disintegrin and metalloproteinase; AEBSEF, 4-(2-aminoethyl)benzenesulfonyl fluoride; Aoc, aminooctanoyl; ARDS, acute respiratory distress syndrome; ATR, anthrax toxin receptor; B, binding domain; BMP-1, bone morphogenetic protein 1; BMP-6, bone morphogenetic protein 6; BMP-9, bone morphogenetic protein 9; BOS, Boston Pharmaceuticals; COVID-19, corona virus disease 2019; CKII, casein kinase II; CRD, cysteine-rich domain; DDP4, dipeptidyl-peptidase 4; DFP, diisopropylfluorophosphate; DT, diphtheria toxins; EDTA, ethylenediaminetetraacetic acid; EF, edema factor; ENaC- $\alpha$ , epithelial sodium channel alpha; ER, endoplasmic reticulum; FCS, furin cleavage site; FP, fusion peptide; FRET, fluorescent resonance energy transfer; FUR, FES upstream region; Furin DB, Furin database; GalNAc, N-acetylgalactosamine; gp120, glycoprotein 120; gp160, glycoprotein 160; gp41, glycoprotein 41; HAMP, hepcidin antimicrobial peptide; HAT, human airway trypsin-like protease; HIV-1, human immunodeficiency virus-1; hAOs, human airway organoids; IBS, Illustrator for Biological Sequences; IC, intracellular domain; ICU, intensive care unit; IFITM, interferon-induced transmembrane; IL-6, inter-

leukin 6; i.p., intraperitoneal; LF, lethal factor; MERS-CoV, Middle-East respiratory syndrome coronavirus; MMPs, matrix metalloproteinases; MLV, murine leukemia virus; MOE, molecular operating environment; MT1-MMP, membrane type 1-matrix metalloproteinase; NTD, N-terminal domain; PA, protective antigen; PA20, 20 kDa PA; PA63, 63 kDa PA; PACE, paired basic amino acid residue-cleaving enzyme; PC, proprotein convertase; PCSK3, proprotein convertase subtilisin/kexin 3; PCSK9, proprotein convertase subtilisin/kexin type 9 serine protease; PDB, protein data bank; PEA, *Pseudomonas* exotoxin A; PK, pharmacokinetics; PLpro, papain-like protease; PMSF, phenylmethylsulfonyl fluoride; RAAS, renin-angiotensin-aldosterone system; RBD, receptor binding domain; RdRp, RNA-dependent RNA polymerase; RMSD, root-mean-square deviation; RSV, respiratory syncytial virus;  $R_{te}$ , transepithelial resistance; RVKR-CMK, Arg-Val-Lys-Arg-chloromethyl ketone; S, spike protein; SARS-CoV, severe acute respiratory syndrome corona virus; SARS-CoV-2, severe acute respiratory syndrome corona virus 2; SFTI-1, sunflower trypsin inhibitor-1; SFV, Semliki Forest virus; siRNA, small interfering RNA; ST, shiga toxin; ST-1, shiga-like toxin-1; S1P, site-1 protease; TGF- $\beta$ , transforming growth factor- $\beta$ ; TGN, trans-Golgi network; TIMPs, tissue inhibitors of metalloproteinases; Tle, tert-leucine; TM, transmembrane domain; TMPRSS2, surface serine protease; TTP, 4'-[p-tolyl]-2,2':6',2''-terpyridine; VSV, vesicular stomatitis virus; 3CLpro, 3-chymotrypsin-like protease; 4-amba, 4-amidino-benzylamide; PLpro, papain-like protease

## REFERENCES

- (1) Andersen, K. G.; Rambaut, A.; Lipkin, W. I.; Holmes, E. C.; Garry, R. F. The proximal origin of SARS-CoV-2. *Nat. Med.* **2020**, *26* (4), 450–452.
- (2) Wu, F.; Zhao, S.; Yu, B.; Chen, Y. M.; Wang, W.; Song, Z. G.; Hu, Y.; Tao, Z. W.; Tian, J. H.; Pei, Y. Y.; Yuan, M. L.; Zhang, Y. L.; Dai, F. H.; Liu, Y.; Wang, Q. M.; Zheng, J. J.; Xu, L.; Holmes, E. C.; Zhang, Y. Z. A new coronavirus associated with human respiratory disease in China. *Nature* **2020**, *579* (7798), 265–269.
- (3) Coronaviridae Study Group of the International Committee on Taxonomy of Viruses. The species Severe acute respiratory syndrome-related coronavirus: classifying 2019-nCoV and naming it SARS-CoV-2. *Nat. Microbiol.* **2020**, *5* (4), 536–544.
- (4) Chan, J. F.; Kok, K. H.; Zhu, Z.; Chu, H.; To, K. K.; Yuan, S.; Yuen, K. Y. Genomic characterization of the 2019 novel human-pathogenic coronavirus isolated from a patient with atypical pneumonia after visiting Wuhan. *Emerg. Microbes Infect.* **2020**, *9* (1), 221–236.
- (5) Al-Omari, A.; Rabaan, A. A.; Salih, S.; Al-Tawfiq, J. A.; Memish, Z. A. MERS coronavirus outbreak: Implications for emerging viral infections. *Diagn. Microbiol. Infect. Dis.* **2019**, *93* (3), 265–285.
- (6) Anderson, R. M.; Fraser, C.; Ghani, A. C.; Donnelly, C. A.; Riley, S.; Ferguson, N. M.; Leung, G. M.; Lam, T. H.; Hedley, A. J. Epidemiology, transmission dynamics and control of SARS: the 2002–2003 epidemic. *Philos. Trans. R. Soc., B* **2004**, *359* (1447), 1091–1105.
- (7) Johns Hopkins Coronavirus Resource Center. <https://coronavirus.jhu.edu/map.html> (accessed on 2021-07-11).
- (8) Dhama, K.; Patel, S. K.; Sharun, K.; Pathak, M.; Tiwari, R.; Yattoo, M. I.; Malik, Y. S.; Sah, R.; Rabaan, A. A.; Panwar, P. K.; Singh, K. P.; Michalak, I.; Chaicumpa, W.; Martinez-Pulgarin, D. F.; Bonilla-Aldana, D. K.; Rodriguez-Morales, A. J. SARS-CoV-2 jumping the species barrier: Zoonotic lessons from SARS, MERS and recent advances to combat this pandemic virus. *Travel Med. Infect. Dis.* **2020**, *37*, 101830.
- (9) Cui, J.; Li, F.; Shi, Z. L. Origin and evolution of pathogenic coronaviruses. *Nat. Rev. Microbiol.* **2019**, *17* (3), 181–192.

- (10) Zhang, T.; Wu, Q.; Zhang, Z. Probable pangolin origin of SARS-CoV-2 associated with the COVID-19 outbreak. *Curr. Biol.* **2020**, *30* (7), 1346–1351.
- (11) Li, W.; Shi, Z.; Yu, M.; Ren, W.; Smith, C.; Epstein, J. H.; Wang, H.; Cramer, G.; Hu, Z.; Zhang, H.; Zhang, J.; McEachern, J.; Field, H.; Daszak, P.; Eaton, B. T.; Zhang, S.; Wang, L. F. Bats are natural reservoirs of SARS-like coronaviruses. *Science* **2005**, *310* (5748), 676–679.
- (12) Osman, E. E. A.; Toogood, P. L.; Neamati, N. COVID-19: Living through another pandemic. *ACS Infect. Dis.* **2020**, *6* (7), 1548–1552.
- (13) Yang, X.; Yu, Y.; Xu, J.; Shu, H.; Xia, J.; Liu, H.; Wu, Y.; Zhang, L.; Yu, Z.; Fang, M.; Yu, T.; Wang, Y.; Pan, S.; Zou, X.; Yuan, S.; Shang, Y. Clinical course and outcomes of critically ill patients with SARS-CoV-2 pneumonia in Wuhan, China: a single-centered, retrospective, observational study. *Lancet Respir. Med.* **2020**, *8* (5), 475–481.
- (14) Zhou, F.; Yu, T.; Du, R.; Fan, G.; Liu, Y.; Liu, Z.; Xiang, J.; Wang, Y.; Song, B.; Gu, X.; Guan, L.; Wei, Y.; Li, H.; Wu, X.; Xu, J.; Tu, S.; Zhang, Y.; Chen, H.; Cao, B. Clinical course and risk factors for mortality of adult inpatients with COVID-19 in Wuhan, China: a retrospective cohort study. *Lancet* **2020**, *395* (10229), 1054–1062.
- (15) Giannis, D.; Ziogas, I. A.; Gianni, P. Coagulation disorders in coronavirus infected patients: COVID-19, SARS-CoV-1, MERS-CoV and lessons from the past. *J. Clin. Virol.* **2020**, *127*, 104362.
- (16) Han, H.; Yang, L.; Liu, R.; Liu, F.; Wu, K. L.; Li, J.; Liu, X. H.; Zhu, C. L. Prominent changes in blood coagulation of patients with SARS-CoV-2 infection. *Clin. Chem. Lab. Med.* **2020**, *58* (7), 1116–1120.
- (17) Forni, G.; Mantovani, A. COVID-19 vaccines: where we stand and challenges ahead. *Cell Death Differ.* **2021**, *28* (2), 626–639.
- (18) Shang, J.; Wan, Y.; Luo, C.; Ye, G.; Geng, Q.; Auerbach, A.; Li, F. Cell entry mechanisms of SARS-CoV-2. *Proc. Natl. Acad. Sci. U. S. A.* **2020**, *117* (21), 11727–11734.
- (19) Hoffmann, M.; Kleine-Weber, H.; Schroeder, S.; Kruger, N.; Herrler, T.; Erichsen, S.; Schiergens, T. S.; Herrler, G.; Wu, N. H.; Nitsche, A.; Muller, M. A.; Drosten, C.; Pohlmann, S. SARS-CoV-2 cell entry depends on ACE2 and TMPRSS2 and is blocked by a clinically proven protease inhibitor. *Cell* **2020**, *181* (2), 271–280.
- (20) Li, F. Structure, function, and evolution of coronavirus spike proteins. *Annu. Rev. Virol.* **2016**, *3* (1), 237–261.
- (21) Shang, J.; Ye, G.; Shi, K.; Wan, Y.; Luo, C.; Aihara, H.; Geng, Q.; Auerbach, A.; Li, F. Structural basis of receptor recognition by SARS-CoV-2. *Nature* **2020**, *581* (7807), 221–224.
- (22) Tang, T.; Bidon, M.; Jaimes, J. A.; Whittaker, G. R.; Daniel, S. Coronavirus membrane fusion mechanism offers a potential target for antiviral development. *Antiviral Res.* **2020**, *178*, 104792.
- (23) Walls, A. C.; Park, Y. J.; Tortorici, M. A.; Wall, A.; McGuire, A. T.; Veesler, D. Structure, function, and antigenicity of the SARS-CoV-2 spike glycoprotein. *Cell* **2020**, *181* (2), 281–292.
- (24) Hoffmann, M.; Hofmann-Winkler, H.; Pöhlmann, S. Priming Time: How Cellular Proteases Arm Coronavirus Spike Proteins. *Activation of Viruses by Host Proteases*; Böttcher-Friebertshäuser, E., Garten, W., Klenk, H. D., Eds.; Springer International Publishing AG: Cham, 2018; pp 71–98.
- (25) Coutard, B.; Valle, C.; de Lamballerie, X.; Canard, B.; Seidah, N. G.; Decroly, E. The spike glycoprotein of the new coronavirus 2019-nCoV contains a furin-like cleavage site absent in CoV of the same clade. *Antiviral Res.* **2020**, *176*, 104742.
- (26) Hoffmann, M.; Kleine-Weber, H.; Pohlmann, S. A multibasic cleavage site in the spike protein of SARS-CoV-2 is essential for infection of human lung cells. *Mol. Cell* **2020**, *78* (4), 779–784.
- (27) Millet, J. K.; Whittaker, G. R. Host cell entry of Middle East respiratory syndrome coronavirus after two-step, furin-mediated activation of the spike protein. *Proc. Natl. Acad. Sci. U. S. A.* **2014**, *111* (42), 15214–15219.
- (28) Heald-Sargent, T.; Gallagher, T. Ready, set, fuse! The coronavirus spike protein and acquisition of fusion competence. *Viruses* **2012**, *4* (4), 557–580.
- (29) Belouzard, S.; Millet, J. K.; Licitra, B. N.; Whittaker, G. R. Mechanisms of coronavirus cell entry mediated by the viral spike protein. *Viruses* **2012**, *4* (6), 1011–1033.
- (30) Bestle, D.; Heindl, M. R.; Limburg, H.; Van Lam van, T.; Pilgram, O.; Moulton, H.; Stein, D. A.; Hards, K.; Eickmann, M.; Dolnik, O.; Rohde, C.; Klenk, H.-D.; Garten, W.; Steinmetzer, T.; Böttcher-Friebertshäuser, E. TMPRSS2 and furin are both essential for proteolytic activation of SARS-CoV-2 in human airway cells. *Life Sci. Alliance* **2020**, *3* (9), e202000786.
- (31) Bugge, T. H.; Antalis, T. M.; Wu, Q. Type II transmembrane serine proteases. *J. Biol. Chem.* **2009**, *284* (35), 23177–23181.
- (32) Kim, T. S.; Heinlein, C.; Hackman, R. C.; Nelson, P. S. Phenotypic analysis of mice lacking the Tmprss2-encoded protease. *Mol. Cell. Biol.* **2006**, *26* (3), 965–975.
- (33) Böttcher, E.; Matrosovich, T.; Beyerle, M.; Klenk, H. D.; Garten, W.; Matrosovich, M. Proteolytic activation of influenza viruses by serine proteases TMPRSS2 and HAT from human airway epithelium. *J. Virol.* **2006**, *80* (19), 9896–9898.
- (34) Thomas, G. Furin at the cutting edge: from protein traffic to embryogenesis and disease. *Nat. Rev. Mol. Cell Biol.* **2002**, *3* (10), 753–766.
- (35) Shiryayev, S. A.; Remacle, A. G.; Ratnikov, B. I.; Nelson, N. A.; Savinov, A. Y.; Wei, G.; Bottini, M.; Rega, M. F.; Parent, A.; Desjardins, R.; Fugere, M.; Day, R.; Sabet, M.; Pellicchia, M.; Liddington, R. C.; Smith, J. W.; Mustelin, T.; Guiney, D. G.; Lebl, M.; Strongin, A. Y. Targeting host cell furin proprotein convertases as a therapeutic strategy against bacterial toxins and viral pathogens. *J. Biol. Chem.* **2007**, *282* (29), 20847–20853.
- (36) Molloy, S. S.; Bresnahan, P. A.; Leppla, S. H.; Klimpel, K. R.; Thomas, G. Human furin is a calcium-dependent serine endoprotease that recognizes the sequence Arg-X-X-Arg and efficiently cleaves anthrax toxin protective antigen. *J. Biol. Chem.* **1992**, *267* (23), 16396–16402.
- (37) Peacock, T. P.; Goldhill, D. H.; Zhou, J.; Baillon, L.; Frise, R.; Swann, O. C.; Kugathasan, R.; Penn, R.; Brown, J. C.; Sanchez-David, R. Y.; Braga, L.; Williamson, M. K.; Hassard, J. A.; Staller, E.; Hanley, B.; Osborn, M.; Giacca, M.; Davidson, A. D.; Matthews, D. A.; Barclay, W. S. The furin cleavage site in the SARS-CoV-2 spike protein is required for transmission in ferrets. *Nat. Microbiol.* **2021**, *6* (7), 899–909.
- (38) Davidson, A. D.; Williamson, M. K.; Lewis, S.; Shoemark, D.; Carroll, M. W.; Heesom, K. J.; Zambon, M.; Ellis, J.; Lewis, P. A.; Hiscox, J. A.; Matthews, D. A. Characterisation of the transcriptome and proteome of SARS-CoV-2 reveals a cell passage induced in-frame deletion of the furin-like cleavage site from the spike glycoprotein. *Genome Med.* **2020**, *12* (1), 68.
- (39) Liu, Z.; Zheng, H.; Lin, H.; Li, M.; Yuan, R.; Peng, J.; Xiong, Q.; Sun, J.; Li, B.; Wu, J.; Yi, L.; Peng, X.; Zhang, H.; Zhang, W.; Hulswit, R. J. G.; Loman, N.; Rambaut, A.; Ke, C.; Bowden, T. A.; Pybus, O. G.; Lu, J. Identification of common deletions in the spike protein of Severe Acute Respiratory Syndrome Coronavirus 2. *J. Virol.* **2020**, *94* (17), 1–9.
- (40) Wrobel, A. G.; Benton, D. J.; Xu, P.; Roustan, C.; Martin, S. R.; Rosenthal, P. B.; Skehel, J. J.; Gamblin, S. J. SARS-CoV-2 and bat RaTG13 spike glycoprotein structures inform on virus evolution and furin-cleavage effects. *Nat. Struct. Mol. Biol.* **2020**, *27* (8), 763–767.
- (41) Hoffmann, M.; Mosbauer, K.; Hofmann-Winkler, H.; Kaul, A.; Kleine-Weber, H.; Kruger, N.; Gassen, N. C.; Muller, M. A.; Drosten, C.; Pohlmann, S. Chloroquine does not inhibit infection of human lung cells with SARS-CoV-2. *Nature* **2020**, *585* (7826), 588–590.
- (42) Winstone, H.; Lista, M. J.; Reid, A. C.; Bouton, C.; Pickering, S.; Galao, R. P.; Kerridge, C.; Doores, K. J.; Swanson, C. M.; Neil, S. J. D. The polybasic cleavage site in SARS-CoV-2 spike modulates viral sensitivity to type I interferon and IFITM2. *J. Virol.* **2021**, *95* (9), 1–16.
- (43) Daly, J. L.; Simonetti, B.; Klein, K.; Chen, K. E.; Williamson, M. K.; Anton-Plagaro, C.; Shoemark, D. K.; Simon-Gracia, L.; Bauer, M.; Hollandi, R.; Greber, U. F.; Horvath, P.; Sessions, R. B.; Helenius, A.; Hiscox, J. A.; Teesalu, T.; Matthews, D. A.; Davidson, A. D.; Collins,



- B. M.; Cullen, P. J.; Yamauchi, Y. Neuropilin-1 is a host factor for SARS-CoV-2 infection. *Science* **2020**, *370* (6518), 861–865.
- (44) Lau, S. Y.; Wang, P.; Mok, B. W.; Zhang, A. J.; Chu, H.; Lee, A. C.; Deng, S.; Chen, P.; Chan, K. H.; Song, W.; Chen, Z.; To, K. K.; Chan, J. F.; Yuen, K. Y.; Chen, H. Attenuated SARS-CoV-2 variants with deletions at the S1/S2 junction. *Emerg. Microbes Infect.* **2020**, *9* (1), 837–842.
- (45) Kong, Y.; Joshi, H. J.; Schjoldager, K. T.; Madsen, T. D.; Gerken, T. A.; Vester-Christensen, M. B.; Wandall, H. H.; Bennett, E. P.; Levery, S. B.; Vakhrushev, S. Y.; Clausen, H. Probing polypeptide GalNAc-transferase isoform substrate specificities by in vitro analysis. *Glycobiology* **2015**, *25* (1), 55–65.
- (46) Zhai, X.; Sun, J.; Yan, Z.; Zhang, J.; Zhao, J.; Zhao, Z.; Gao, Q.; He, W. T.; Veit, M.; Su, S. Comparison of Severe Acute Respiratory Syndrome Coronavirus 2 spike protein binding to ACE2 receptors from human, pets, farm animals, and putative intermediate hosts. *J. Virol.* **2020**, *94* (15), 1–13.
- (47) Gram Schjoldager, K. T.-B.; Vester-Christensen, M. B.; Goth, C. K.; Petersen, T. N.; Brunak, S.; Bennett, E. P.; Levery, S. B.; Clausen, H. A systematic study of site-specific GalNAc-type O-glycosylation modulating proprotein convertase processing. *J. Biol. Chem.* **2011**, *286* (46), 40122–40132.
- (48) Roebroek, A. J.; Schalken, J. A.; Leunissen, J. A.; Onnekink, C.; Bloemers, H. P.; Van de Ven, W. J. Evolutionary conserved close linkage of the *c-fes/fps* proto-oncogene and genetic sequences encoding a receptor-like protein. *EMBO J.* **1986**, *5* (9), 2197–2202.
- (49) Hatsuzawa, K.; Hosaka, M.; Nakagawa, T.; Nagase, M.; Shoda, A.; Murakami, K.; Nakayama, K. Structure and expression of mouse furin, a yeast Kex2-related protease. Lack of processing of coexpressed prorenin in GH4C1 cells. *J. Biol. Chem.* **1990**, *265* (36), 22075–22078.
- (50) Hatsuzawa, K.; Nagahama, M.; Takahashi, S.; Takada, K.; Murakami, K.; Nakayama, K. Purification and characterization of furin, a Kex2-like processing endoprotease, produced in Chinese hamster ovary cells. *J. Biol. Chem.* **1992**, *267* (23), 16094–16099.
- (51) van Duijnhoven, H. L.; Creemers, J. W.; Kranenborg, M. G.; Timmer, E. D.; Groeneveld, A.; van den Ouweland, A. M.; Roebroek, A. J.; van de Ven, W. J. Development and characterization of a panel of monoclonal antibodies against the novel subtilisin-like proprotein processing enzyme furin. *Hybridoma* **1992**, *11* (1), 71–86.
- (52) Tsuneoka, M.; Nakayama, K.; Hatsuzawa, K.; Komada, M.; Kitamura, N.; Mekada, E. Evidence for involvement of furin in cleavage and activation of diphtheria toxin. *J. Biol. Chem.* **1993**, *268* (35), 26461–26465.
- (53) Anderson, E. D.; Thomas, L.; Hayflick, J. S.; Thomas, G. Inhibition of HIV-1 gp160-dependent membrane fusion by a furin-directed alpha 1-antitrypsin variant. *J. Biol. Chem.* **1993**, *268* (33), 24887–24891.
- (54) Hallenberger, S.; Bosch, V.; Angliker, H.; Shaw, E.; Klenk, H. D.; Garten, W. Inhibition of furin-mediated cleavage activation of HIV-1 glycoprotein gp160. *Nature* **1992**, *360* (6402), 358–361.
- (55) Siezen, R. J.; Creemers, J. W. M.; Ven, W. J. M. Homology modelling of the catalytic domain of human furin. A model for the eukaryotic subtilisin-like proprotein convertases. *Eur. J. Biochem.* **1994**, *222* (2), 255–266.
- (56) Garten, W.; Hallenberger, S.; Ortmann, D.; Schafer, W.; Vey, M.; Angliker, H.; Shaw, E.; Klenk, H. D. Processing of viral glycoproteins by the subtilisin-like endoprotease furin and its inhibition by specific peptidylchloroalkylketones. *Biochimie* **1994**, *76* (3–4), 217–225.
- (57) Henrich, S.; Cameron, A.; Bourenkov, G. P.; Kiefersauer, R.; Huber, R.; Lindberg, I.; Bode, W.; Than, M. E. The crystal structure of the proprotein processing proteinase furin explains its stringent specificity. *Nat. Struct. Mol. Biol.* **2003**, *10* (7), 520–526.
- (58) Scamuffa, N.; Calvo, F.; Chretien, M.; Seidah, N. G.; Khatib, A. M. Proprotein convertases: lessons from knockouts. *FASEB J.* **2006**, *20* (12), 1954–1963.
- (59) Jiao, G. S.; Cregar, L.; Wang, J.; Millis, S. Z.; Tang, C.; O'Malley, S.; Johnson, A. T.; Sareth, S.; Larson, J.; Thomas, G. Synthetic small molecule furin inhibitors derived from 2,5-dideoxystreptamine. *Proc. Natl. Acad. Sci. U. S. A.* **2006**, *103* (52), 19707–19712.
- (60) Dahms, S. O.; Harges, K.; Becker, G. L.; Steinmetzer, T.; Brandstetter, H.; Than, M. E. X-ray structures of human furin in complex with competitive inhibitors. *ACS Chem. Biol.* **2014**, *9* (5), 1113–1118.
- (61) Wise, R. J.; Barr, P. J.; Wong, P. A.; Kiefer, M. C.; Brake, A. J.; Kaufman, R. J. Expression of a human proprotein processing enzyme: correct cleavage of the von Willebrand factor precursor at a paired basic amino acid site. *Proc. Natl. Acad. Sci. U. S. A.* **1990**, *87* (23), 9378–9382.
- (62) Van de Ven, W. J.; Creemers, J. W.; Roebroek, A. J. Furin: the prototype mammalian subtilisin-like proprotein-processing enzyme. Endoproteolytic cleavage at paired basic residues of proproteins of the eukaryotic secretory pathway. *Enzyme* **2017**, *45* (5–6), 257–270.
- (63) van de Ven, W. J.; Voorberg, J.; Fontijn, R.; Pannekoek, H.; van den Ouweland, A. M.; van Duijnhoven, H. L.; Roebroek, A. J.; Siezen, R. J. Furin is a subtilisin-like proprotein processing enzyme in higher eukaryotes. *Mol. Biol. Rep.* **1990**, *14* (4), 265–275.
- (64) Seidah, N. G.; Sadr, M. S.; Chretien, M.; Mbikay, M. The multifaceted proprotein convertases: their unique, redundant, complementary, and opposite functions. *J. Biol. Chem.* **2013**, *288* (30), 21473–21481.
- (65) Bresnahan, P. A.; Leduc, R.; Thomas, L.; Thorner, J.; Gibson, H. L.; Brake, A. J.; Barr, P. J.; Thomas, G. Human fur gene encodes a yeast KEX2-like endoprotease that cleaves pro-beta-NGF in vivo. *J. Cell Biol.* **1990**, *111* (6), 2851–28519.
- (66) Klein-Szanto, A. J.; Bassi, D. E. Proprotein convertase inhibition: Paralyzing the cell's master switches. *Biochem. Pharmacol.* **2017**, *140*, 8–15.
- (67) Nakayama, K. Furin: a mammalian subtilisin/Kex2p-like endoprotease involved in processing of a wide variety of precursor proteins. *Biochem. J.* **1997**, *327* (3), 625–635.
- (68) Molloy, S. S.; Anderson, E. D.; Jean, F.; Thomas, G. Bi-cycling the furin pathway: from TGN localization to pathogen activation and embryogenesis. *Trends Cell Biol.* **1999**, *9* (1), 28–35.
- (69) Garten, W. Characterization of Proprotein Convertases and Their Involvement in Virus Propagation. In *Activation of Viruses by Host Proteases*; Böttcher-Friebertshäuser, E., Garten, W., Klenk, H. D., Eds.; Springer International Publishing AG: Cham, 2018; pp 205–248.
- (70) Steinmetzer, T.; Harges, K. The Antiviral Potential of Host Protease Inhibitors. In *Activation of Viruses by Host Proteases*; Böttcher-Friebertshäuser, E., Garten, W., Klenk, H. D., Eds. Springer International Publishing: Cham, 2018; pp 279–325.
- (71) Seidah, N. G.; Prat, A. The biology and therapeutic targeting of the proprotein convertases. *Nat. Rev. Drug Discovery* **2012**, *11* (5), 367–383.
- (72) Arstenstein, A. W.; Opal, S. M. Proprotein convertases in health and disease. *N. Engl. J. Med.* **2011**, *365* (26), 2507–2518.
- (73) Molloy, S. S.; Thomas, G. Furin. In *Co- and Posttranslational Proteolysis of Proteins*; Dalbey, R. E., Sigman, D. S., Eds.; Academic Press: San Diego, CA, 2002; Vol. 22, pp 199–235.
- (74) Dahms, S. O.; Arciniega, M.; Steinmetzer, T.; Huber, R.; Than, M. E. Structure of the unliganded form of the proprotein convertase furin suggests activation by a substrate-induced mechanism. *Proc. Natl. Acad. Sci. U. S. A.* **2016**, *113* (40), 11196–11201.
- (75) Zhou, A.; Martin, S.; Lipkind, G.; LaMendola, J.; Steiner, D. F. Regulatory roles of the P domain of the subtilisin-like prohormone convertases. *J. Biol. Chem.* **1998**, *273* (18), 11107–11114.
- (76) Lipkind, G. M.; Zhou, A.; Steiner, D. F. A model for the structure of the P domains in the subtilisin-like prohormone convertases. *Proc. Natl. Acad. Sci. U. S. A.* **1998**, *95* (13), 7310–7315.
- (77) Nour, N.; Mayer, G.; Mort, J. S.; Salvat, A.; Mbikay, M.; Morrison, C. J.; Overall, C. M.; Seidah, N. G. The cysteine-rich domain of the secreted proprotein convertases PCSA and PACE4 functions as a cell surface anchor and interacts with tissue inhibitors of metalloproteinases. *Mol. Biol. Cell* **2005**, *16* (11), 5215–5226.

- (78) Arpino, V.; Brock, M.; Gill, S. E. The role of TIMPs in regulation of extracellular matrix proteolysis. *Matrix Biol.* **2015**, *44–46*, 247–254.
- (79) Lapiere, M.; Siegfried, G.; Scamuffa, N.; Bontemps, Y.; Calvo, F.; Seidah, N. G.; Khatib, A. M. Opposing function of the proprotein convertases furin and PACE4 on breast cancer cells' malignant phenotypes: role of tissue inhibitors of metalloproteinase-1. *Cancer Res.* **2007**, *67* (19), 9030–9034.
- (80) Stawowy, P.; Meyborg, H.; Stibenz, D.; Stawowy, N. B. P.; Roser, M.; Thanabalasingam, U.; Veinot, J. P.; Chretien, M.; Seidah, N. G.; Fleck, E.; Graf, K. Furin-like proprotein convertases are central regulators of the membrane type matrix metalloproteinase-pro-matrix metalloproteinase-2 proteolytic cascade in atherosclerosis. *Circulation* **2005**, *111* (21), 2820–2827.
- (81) Anderson, E. D.; Molloy, S. S.; Jean, F.; Fei, H.; Shimamura, S.; Thomas, G. The ordered and compartment-specific autoproteolytic removal of the furin intramolecular chaperone is required for enzyme activation. *J. Biol. Chem.* **2002**, *277* (15), 12879–12890.
- (82) Liu, W.; Xie, Y.; Ma, J.; Luo, X.; Nie, P.; Zuo, Z.; Lahrmann, U.; Zhao, Q.; Zheng, Y.; Zhao, Y.; Xue, Y.; Ren, J. IBS: an illustrator for the presentation and visualization of biological sequences. *Bioinformatics* **2015**, *31* (20), 3359–3361.
- (83) Susic, J.; Lynd, J.; Susic, H. Disulfide bonds in the catalytic domain of furin are necessary for compartment-specific folding events. *FASEB J.* **2006**, *20* (5), LB66.
- (84) Jones, B. G.; Thomas, L.; Molloy, S. S.; Thulin, C. D.; Fry, M. D.; Walsh, K. A.; Thomas, G. Intracellular trafficking of furin is modulated by the phosphorylation state of a casein kinase II site in its cytoplasmic tail. *EMBO J.* **1995**, *14* (23), 5869–5883.
- (85) Pearce, K. H.; Overton, L. K.; Gampe, R. T.; Barrett, G. B.; Taylor, J. D.; McKee, D. D.; Campobasso, N.; Nolte, R. T.; Reid, R. A. BacMam production and crystal structure of nonglycosylated apo human furin at 1.89 Å resolution. *Acta Crystallogr., Sect. F: Struct. Biol. Commun.* **2019**, *75* (4), 239–245.
- (86) Kacprzak, M. M.; Peinado, J. R.; Than, M. E.; Appel, J.; Henrich, S.; Lipkind, G.; Houghten, R. A.; Bode, W.; Lindberg, I. Inhibition of furin by polyarginine-containing peptides: nanomolar inhibition by nona-D-arginine. *J. Biol. Chem.* **2004**, *279* (35), 36788–36794.
- (87) Roebroek, A. J.; Taylor, N. A.; Louagie, E.; Pauli, I.; Smeijers, L.; Snellinx, A.; Lauwers, A.; Van de Ven, W. J.; Hartmann, D.; Creemers, J. W. Limited redundancy of the proprotein convertase furin in mouse liver. *J. Biol. Chem.* **2004**, *279* (51), 53442–53450.
- (88) Kim, W.; Essalmani, R.; Szumska, D.; Creemers, J. W.; Roebroek, A. J.; D'Orleans-Juste, P.; Bhattacharya, S.; Seidah, N. G.; Prat, A. Loss of endothelial furin leads to cardiac malformation and early postnatal death. *Mol. Cell. Biol.* **2012**, *32* (17), 3382–3391.
- (89) Pesu, M.; Watford, W. T.; Wei, L.; Xu, L.; Fuss, I.; Strober, W.; Andersson, J.; Shevach, E. M.; Quezado, M.; Bouladoux, N.; Roebroek, A.; Belkaid, Y.; Creemers, J.; O'Shea, J. J. T-cell-expressed proprotein convertase furin is essential for maintenance of peripheral immune tolerance. *Nature* **2008**, *455* (7210), 246–250.
- (90) Anderson, E. D.; VanSlyke, J. K.; Thulin, C. D.; Jean, F.; Thomas, G. Activation of the furin endoprotease is a multiple-step process: requirements for acidification and internal propeptide cleavage. *EMBO J.* **1997**, *16* (7), 1508–1518.
- (91) Izaguirre, G. The proteolytic regulation of virus cell entry by furin and other proprotein convertases. *Viruses* **2019**, *11* (9), 837–855.
- (92) Braun, E.; Sauter, D. Furin-mediated protein processing in infectious diseases and cancer. *Clin. Transl. Immunol.* **2019**, *8* (8), e1073.
- (93) Checkley, M. A.; Luttgge, B. G.; Freed, E. O. HIV-1 envelope glycoprotein biosynthesis, trafficking, and incorporation. *J. Mol. Biol.* **2011**, *410* (4), 582–608.
- (94) Becker, G. L.; Lu, Y.; Harges, K.; Strehlow, B.; Levesque, C.; Lindberg, I.; Sandvig, K.; Bakowsky, U.; Day, R.; Garten, W.; Steinmetzer, T. Highly potent inhibitors of proprotein convertase furin as potential drugs for treatment of infectious diseases. *J. Biol. Chem.* **2012**, *287* (26), 21992–22003.
- (95) Imran, M.; Saleemi, M. K.; Chen, Z.; Wang, X.; Zhou, D.; Li, Y.; Zhao, Z.; Zheng, B.; Li, Q.; Cao, S.; Ye, J. Decanoyl-Arg-Val-Lys-Arg-chloromethylketone: An antiviral compound that acts against flaviviruses through the inhibition of furin-mediated prM cleavage. *Viruses* **2019**, *11* (11), 1011.
- (96) Rana, J.; Slon Campos, J. L.; Poggianella, M.; Burrone, O. R. Dengue virus capsid anchor modulates the efficiency of polyprotein processing and assembly of viral particles. *J. Gen. Virol.* **2019**, *100* (12), 1663–1673.
- (97) Ozden, S.; Lucas-Hourani, M.; Ceccaldi, P. E.; Basak, A.; Valentine, M.; Benjannet, S.; Hamelin, J.; Jacob, Y.; Mamchaoui, K.; Mouly, V.; Despres, P.; Gessain, A.; Butler-Browne, G.; Chretien, M.; Tangy, F.; Vidalain, P. O.; Seidah, N. G. Inhibition of Chikungunya virus infection in cultured human muscle cells by furin inhibitors: impairment of the maturation of the E2 surface glycoprotein. *J. Biol. Chem.* **2008**, *283* (32), 21899–21908.
- (98) Volchkov, V. E.; Feldmann, H.; Volchkova, V. A.; Klenk, H. D. Processing of the Ebola virus glycoprotein by the proprotein convertase furin. *Proc. Natl. Acad. Sci. U. S. A.* **1998**, *95* (10), 5762–5767.
- (99) Feldmann, H.; Volchkov, V. E.; Volchkova, V. A.; Klenk, H. D. The glycoproteins of Marburg and Ebola virus and their potential roles in pathogenesis. *Arch. Virol. Suppl.* **1999**, *15*, 159–169.
- (100) Watanabe, M.; Hirano, A.; Stenglein, S.; Nelson, J.; Thomas, G.; Wong, T. C. Engineered serine protease inhibitor prevents furin-catalyzed activation of the fusion glycoprotein and production of infectious measles virus. *J. Virol.* **1995**, *69* (5), 3206–3210.
- (101) Neumann, G.; Geisbert, T. W.; Ebihara, H.; Geisbert, J. B.; Daddario-DiCaprio, K. M.; Feldmann, H.; Kawaoka, Y. Proteolytic processing of the Ebola virus glycoprotein is not critical for Ebola virus replication in nonhuman primates. *J. Virol.* **2007**, *81* (6), 2995–2998.
- (102) Neumann, G.; Feldmann, H.; Watanabe, S.; Lukashevich, I.; Kawaoka, Y. Reverse genetics demonstrates that proteolytic processing of the Ebola virus glycoprotein is not essential for replication in cell culture. *J. Virol.* **2002**, *76* (1), 406–410.
- (103) Mykityn, A. Z.; Breugem, T. I.; Riesebosch, S.; Schipper, D.; van den Doel, P. B.; Rottier, R. J.; Lamers, M. M.; Haagmans, B. L. SARS-CoV-2 entry into human airway organoids is serine protease-mediated and facilitated by the multibasic cleavage site. *eLife* **2021**, *10*, e64508.
- (104) Johnson, B. A.; Xie, X.; Bailey, A. L.; Kalveram, B.; Lokugamage, K. G.; Muruato, A.; Zou, J.; Zhang, X.; Juelich, T.; Smith, J. K.; Zhang, L.; Bopp, N.; Schindewolf, C.; Vu, M.; Vanderheiden, A.; Winkler, E. S.; Swetnam, D.; Plante, J. A. M.; Aguilar, P.; Plante, K. S.; Popov, V.; Lee, B.; Weaver, S. C.; Suthar, M. S.; Routh, A. L.; Ren, P.; Ku, Z.; An, Z.; Debbink, K.; Diamond, M. S.; Shi, P. Y.; Freiberg, A. N.; Menachery, V. D. Loss of furin cleavage site attenuates SARS-CoV-2 pathogenesis. *Nature* **2021**, *591* (7849), 293–299.
- (105) Papa, G.; Mallery, D. L.; Albecka, A.; Welch, L. G.; Cattin-Ortola, J.; Luptak, J.; Paul, D.; McMahon, H. T.; Goodfellow, I. G.; Carter, A.; Munro, S.; James, L. C. Furin cleavage of SARS-CoV-2 Spike promotes but is not essential for infection and cell-cell fusion. *PLoS Pathog.* **2021**, *17* (1), e1009246.
- (106) Xia, S.; Lan, Q.; Su, S.; Wang, X.; Xu, W.; Liu, Z.; Zhu, Y.; Wang, Q.; Lu, L.; Jiang, S. The role of furin cleavage site in SARS-CoV-2 spike protein-mediated membrane fusion in the presence or absence of trypsin. *Signal Transduct. Target. Ther.* **2020**, *5* (1), 92.
- (107) Xing, Y.; Li, X.; Gao, X.; Dong, Q. Natural polymorphisms are present in the furin cleavage site of the SARS-CoV-2 spike glycoprotein. *Front. Genet.* **2020**, *11*, 783.
- (108) Tang, T.; Jaimes, J. A.; Bidon, M. K.; Straus, M. R.; Daniel, S.; Whittaker, G. R. Proteolytic activation of SARS-CoV-2 spike at the S1/S2 boundary: Potential role of proteases beyond furin. *ACS Infect. Dis.* **2021**, *7* (2), 264–272.

- (109) Gunst, J. D.; Staerke, N. B.; Pahun, M. H.; Kristensen, L. H.; Bodilsen, J.; Lohse, N.; Dalgard, L. S.; Bronnum, D.; Frobert, O.; Honge, B.; Johansen, I. S.; Monrad, L.; Erikstrup, C.; Rosendal, R.; Vilstrup, E.; Mariager, T.; Bove, D. G.; Offersen, R.; Shakar, S.; Cajander, S.; Jorgensen, N. P.; Sritharan, S. S.; Breining, P.; Jespersen, S.; Mortensen, K. L.; Jensen, M. L.; Kolte, L.; Frattari, G. S.; Larsen, C. S.; Storgaard, M.; Nielsen, L. P.; Tolstrup, M.; Saedder, E. A.; Ostergaard, L. J.; Ngo, H. T. T.; Jensen, M. H.; Hojen, J. F.; Kjolby, M.; Sogaard, O. S. Efficacy of the TMPRSS2 inhibitor camostat mesilate in patients hospitalized with Covid-19-a double-blind randomized controlled trial. *EClinicalMedicine* **2021**, *35*, 100849.
- (110) Anand, P.; Puranik, A.; Aravamudan, M.; Venkatakrishnan, A. J.; Soundararajan, V. SARS-CoV-2 strategically mimics proteolytic activation of human ENaC. *eLife* **2020**, *9*, e58603.
- (111) Elbe, S.; Buckland-Merrett, G. Data, disease and diplomacy: GISAID's innovative contribution to global health. *Glob. Chall.* **2017**, *1* (1), 33–46.
- (112) Vallet, V.; Chraïbi, A.; Gaeggeler, H. P.; Horisberger, J. D.; Rossier, B. C. An epithelial serine protease activates the amiloride-sensitive sodium channel. *Nature* **1997**, *389* (6651), 607–610.
- (113) Rossier, B. C.; Stutts, M. J. Activation of the epithelial sodium channel (ENaC) by serine proteases. *Annu. Rev. Physiol.* **2009**, *71*, 361–379.
- (114) Musante, I.; Scudieri, P.; Venturini, A.; Guidone, D.; Caci, E.; Castellani, S.; Conese, M.; Galiotta, L. J. V. Peripheral localization of the epithelial sodium channel in the apical membrane of bronchial epithelial cells. *Exp. Physiol.* **2019**, *104* (6), 866–875.
- (115) Lu, M.; Echeverri, F.; Kalabat, D.; Laita, B.; Dahan, D. S.; Smith, R. D.; Xu, H.; Staszewski, L.; Yamamoto, J.; Ling, J.; Hwang, N.; Kimmich, R.; Li, P.; Patron, E.; Keung, W.; Patron, A.; Moyer, B. D. Small molecule activator of the human epithelial sodium channel. *J. Biol. Chem.* **2008**, *283* (18), 11981–11994.
- (116) George, P. M.; Wells, A. U.; Jenkins, R. G. Pulmonary fibrosis and COVID-19: the potential role for antifibrotic therapy. *Lancet Respir. Med.* **2020**, *8* (8), 807–815.
- (117) Scelfo, C.; Fontana, M.; Casalini, E.; Menzella, F.; Piro, R.; Zerbini, A.; Spaggiari, L.; Ghidorsi, L.; Ghidoni, G.; Facciolongo, N. C. A dangerous consequence of the recent pandemic: Early lung fibrosis following COVID-19 pneumonia - Case reports. *Ther. Clin. Risk Manage.* **2020**, *16*, 1039–1046.
- (118) Li, S. W.; Yang, T. C.; Wan, L.; Lin, Y. J.; Tsai, F. J.; Lai, C. C.; Lin, C. W. Correlation between TGF- $\beta$ 1 expression and proteomic profiling induced by severe acute respiratory syndrome coronavirus papain-like protease. *Proteomics* **2012**, *12* (21), 3193–3205.
- (119) Li, S. W.; Wang, C. Y.; Jou, Y. J.; Yang, T. C.; Huang, S. H.; Wan, L.; Lin, Y. J.; Lin, C. W. SARS coronavirus papain-like protease induces Egr-1-dependent up-regulation of TGF- $\beta$ 1 via ROS/p38 MAPK/STAT3 pathway. *Sci. Rep.* **2016**, *6* (1), 25754.
- (120) Zhao, X.; Nicholls, J. M.; Chen, Y. G. Severe acute respiratory syndrome-associated coronavirus nucleocapsid protein interacts with Smad3 and modulates transforming growth factor-beta signaling. *J. Biol. Chem.* **2008**, *283* (6), 3272–3280.
- (121) Molteni, A.; Wolfe, L. F.; Ward, W. F.; Ts'ao, C. H.; Molteni, L. B.; Veno, P.; Fish, B. L.; Taylor, J. M.; Quintanilla, N.; Herndon, B.; Moulder, J. E. Effect of an angiotensin II receptor blocker and two angiotensin converting enzyme inhibitors on transforming growth factor-beta (TGF-beta) and alpha-actomyosin (alpha SMA), important mediators of radiation-induced pneumopathy and lung fibrosis. *Curr. Pharm. Des.* **2007**, *13* (13), 1307–1316.
- (122) Ortega-Paz, L.; Capodanno, D.; Montalescot, G.; Angiolillo, D. J. Coronavirus Disease 2019-associated thrombosis and coagulopathy: Review of the pathophysiological characteristics and implications for antithrombotic management. *J. Am. Heart Assoc.* **2021**, *10* (3), e019650.
- (123) Bolondi, G.; Russo, E.; Gamberini, E.; Circelli, A.; Meca, M. C. C.; Brogi, E.; Viola, L.; Bissoni, L.; Poletti, V.; Agnoletti, V. Iron metabolism and lymphocyte characterisation during Covid-19 infection in ICU patients: an observational cohort study. *World J. Emerg. Surg.* **2020**, *15*, 41.
- (124) Taneri, P. E.; Gomez-Ochoa, S. A.; Llanaj, E.; Raguindin, P. F.; Rojas, L. Z.; Roa-Diaz, Z. M.; Salvador, D., Jr.; Groothof, D.; Minder, B.; Kopp-Heim, D.; Hautz, W. E.; Eisenga, M. F.; Franco, O. H.; Glisic, M.; Muka, T. Anemia and iron metabolism in COVID-19: a systematic review and meta-analysis. *Eur. J. Epidemiol.* **2020**, *35* (8), 763–773.
- (125) Shah, A.; Frost, J. N.; Aaron, L.; Donovan, K.; Drakesmith, H.; McKechnie, S. R.; Stanworth, S. J. Systemic hypoferrremia and severity of hypoxemic respiratory failure in COVID-19. *Crit. Care* **2020**, *24* (1), 320.
- (126) Hippchen, T.; Altamura, S.; Muckenthaler, M. U.; Merle, U. Hypoferrremia is associated with increased hospitalization and oxygen demand in COVID-19 patients. *Hemasphere* **2020**, *4* (6), e492.
- (127) Wang, C. Y.; Babbitt, J. L. Hepcidin regulation in the anemia of inflammation. *Curr. Opin. Hematol.* **2016**, *23* (3), 189–197.
- (128) Steinbicker, A. U.; Sachidanandan, C.; Vonner, A. J.; Yusuf, R. Z.; Deng, D. Y.; Lai, C. S.; Rauwerdink, K. M.; Winn, J. C.; Saez, B.; Cook, C. M.; Szekely, B. A.; Roy, C. N.; Seehra, J. S.; Cuny, G. D.; Scadden, D. T.; Peterson, R. T.; Bloch, K. D.; Yu, P. B. Inhibition of bone morphogenetic protein signaling attenuates anemia associated with inflammation. *Blood* **2011**, *117* (18), 4915–4923.
- (129) Wrighting, D. M.; Andrews, N. C. Interleukin-6 induces hepcidin expression through STAT3. *Blood* **2006**, *108* (9), 3204–3209.
- (130) Nemeth, E.; Ganz, T. The role of hepcidin in iron metabolism. *Acta Haematol.* **2009**, *122* (2–3), 78–86.
- (131) Ganz, T. Hepcidin and iron regulation, 10 years later. *Blood* **2011**, *117* (17), 4425–4433.
- (132) Valore, E. V.; Ganz, T. Posttranslational processing of hepcidin in human hepatocytes is mediated by the prohormone convertase furin. *Blood Cells, Mol. Dis.* **2008**, *40* (1), 132–138.
- (133) Poli, M.; Asperti, M.; Ruzzenenti, P.; Regoni, M.; Arosio, P. Hepcidin antagonists for potential treatments of disorders with hepcidin excess. *Front. Pharmacol.* **2014**, *5* (86), 86.
- (134) Nai, A.; Lore, N. I.; Pagani, A.; De Lorenzo, R.; Di Modica, S.; Saliu, F.; Cirillo, D. M.; Rovere-Querini, P.; Manfredi, A. A.; Silvestri, L. Hepcidin levels predict Covid-19 severity and mortality in a cohort of hospitalized Italian patients. *Am. J. Hematol.* **2021**, *96* (1), E32–E35.
- (135) Xia, J. J.; Wang, F.; Jiang, X. N.; Jiang, T. T.; Shen, L. J.; Liu, Y.; You, D. L.; Ding, Y.; Ju, X. F.; Wang, L.; Wu, X.; Hu, S. Y. Serum iron levels are an independent predictor of in-hospital mortality of critically ill patients: a retrospective, single-institution study. *J. Int. Med.* **2019**, *47* (1), 66–75.
- (136) Zhou, Y.; Yang, Q.; Chi, J.; Dong, B.; Lv, W.; Shen, L.; Wang, Y. Comorbidities and the risk of severe or fatal outcomes associated with coronavirus disease 2019: A systematic review and meta-analysis. *Int. J. Infect. Dis.* **2020**, *99*, 47–56.
- (137) Sanyaolu, A.; Okorie, C.; Marinkovic, A.; Patidar, R.; Younis, K.; Desai, P.; Hosein, Z.; Padda, I.; Mangat, J.; Altaf, M. Comorbidity and its impact on patients with COVID-19. *SN Compr. Clin. Med.* **2020**, *2*, 1069–1076.
- (138) Mbikay, M.; Sirois, F.; Yao, J.; Seidah, N. G.; Chretien, M. Comparative analysis of expression of the proprotein convertases furin, PACE4, PC1 and PC2 in human lung tumours. *Br. J. Cancer* **1997**, *75* (10), 1509–1514.
- (139) Cheng, M.; Watson, P. H.; Paterson, J. A.; Seidah, N.; Chretien, M.; Shiu, R. P. Pro-protein convertase gene expression in human breast cancer. *Int. J. Cancer* **1997**, *71* (6), 966–971.
- (140) Bassi, D. E.; Mahloogi, H.; Al-Saleem, L.; Lopez De Cicco, R.; Ridge, J. A.; Klein-Szanto, A. J. Elevated furin expression in aggressive human head and neck tumors and tumor cell lines. *Mol. Carcinog.* **2001**, *31* (4), 224–232.
- (141) Khatib, A. M.; Siegfried, G.; Chretien, M.; Metrakos, P.; Seidah, N. G. Proprotein convertases in tumor progression and malignancy: novel targets in cancer therapy. *Am. J. Pathol.* **2002**, *160* (6), 1921–1935.
- (142) Jaaks, P.; Bernasconi, M. The proprotein convertase furin in tumour progression. *Int. J. Cancer* **2017**, *141* (4), 654–663.



- (143) Harris, N. C.; Achen, M. G. The proteolytic activation of angiogenic and lymphangiogenic growth factors in cancer—its potential relevance for therapeutics and diagnostics. *Curr. Med. Chem.* **2014**, *21* (16), 1821–1842.
- (144) Wang, Y. K.; Tang, J. N.; Han, L.; Liu, X. D.; Shen, Y. L.; Zhang, C. Y.; Liu, X. B. Elevated FURIN levels in predicting mortality and cardiovascular events in patients with acute myocardial infarction. *Metab., Clin. Exp.* **2020**, *111*, 154323.
- (145) Ren, K.; Jiang, T.; Zheng, X. L.; Zhao, G. J. Proprotein convertase furin/PCSK3 and atherosclerosis: New insights and potential therapeutic targets. *Atherosclerosis* **2017**, *262*, 163–170.
- (146) Joffe, J.; Ait-Oufella, H. Targeting the immune response in atherosclerosis: It's time for clinical trials! *Arch. Cardiovasc. Dis.* **2017**, *110* (12), 643–645.
- (147) Turpeinen, H.; Raitoharju, E.; Oksanen, A.; Oksala, N.; Levula, M.; Lyytikäinen, L. P.; Jarvinen, O.; Creemers, J. W.; Kahonen, M.; Laaksonen, R.; Pelto-Huikko, M.; Lehtimäki, T.; Pesu, M. Proprotein convertases in human atherosclerotic plaques: the overexpression of FURIN and its substrate cytokines BAFF and APRIL. *Atherosclerosis* **2011**, *219* (2), 799–806.
- (148) Yakala, G. K.; Cabrera-Fuentes, H. A.; Crespo-Avilan, G. E.; Rattanasopa, C.; Burlacu, A.; George, B. L.; Anand, K.; Mayan, D. C.; Corliano, M.; Hernandez-Resendiz, S.; Wu, Z.; Schwerk, A. M. K.; Tan, A. L. J.; Trigueros-Motos, L.; Chevre, R.; Chua, T.; Kleemann, R.; Liehn, E. A.; Hausenloy, D. J.; Ghosh, S.; Singaraja, R. R. FURIN inhibition reduces vascular remodeling and atherosclerotic lesion progression in mice. *Arterioscler. Thromb. Vasc. Biol.* **2019**, *39* (3), 387–401.
- (149) Fernandez, C.; Rysa, J.; Almgren, P.; Nilsson, J.; Engstrom, G.; Orho-Melander, M.; Ruskoaho, H.; Melander, O. Plasma levels of the proprotein convertase furin and incidence of diabetes and mortality. *J. Intern. Med.* **2018**, *284* (4), 377–387.
- (150) Klimpel, K. R.; Molloy, S. S.; Thomas, G.; Leppla, S. H. Anthrax toxin protective antigen is activated by a cell surface protease with the sequence specificity and catalytic properties of furin. *Proc. Natl. Acad. Sci. U. S. A.* **1992**, *89* (21), 10277–10281.
- (151) Mock, M.; Fouet, A. Anthrax. *Annu. Rev. Microbiol.* **2001**, *55*, 647–671.
- (152) Bradley, K. A.; Mogridge, J.; Mourez, M.; Collier, R. J.; Young, J. A. Identification of the cellular receptor for anthrax toxin. *Nature* **2001**, *414* (6860), 225–229.
- (153) Beauregard, K. E.; Collier, R. J.; Swanson, J. A. Proteolytic activation of receptor-bound anthrax protective antigen on macrophages promotes its internalization. *Cell. Microbiol.* **2000**, *2* (3), 251–258.
- (154) Gordon, V. M.; Klimpel, K. R.; Arora, N.; Henderson, M. A.; Leppla, S. H. Proteolytic activation of bacterial toxins by eukaryotic cells is performed by furin and by additional cellular proteases. *Infect. Immun.* **1995**, *63* (1), 82–87.
- (155) Kurmanova, A.; Llorente, A.; Poleskaya, A.; Garred, O.; Olsnes, S.; Kozlov, J.; Sandvig, K. Structural requirements for furin-induced cleavage and activation of Shiga toxin. *Biochem. Biophys. Res. Commun.* **2007**, *357* (1), 144–149.
- (156) Schiavo, G.; van der Goot, F. G. The bacterial toxin toolkit. *Nat. Rev. Mol. Cell Biol.* **2001**, *2* (7), 530–537.
- (157) Garred, O.; van Deurs, B.; Sandvig, K. Furin-induced cleavage and activation of Shiga toxin. *J. Biol. Chem.* **1995**, *270* (18), 10817–10821.
- (158) Jean, F.; Stella, K.; Thomas, L.; Liu, G.; Xiang, Y.; Reason, A. J.; Thomas, G. alpha1-Antitrypsin Portland, a bioengineered serpin highly selective for furin: application as an antipathogenic agent. *Proc. Natl. Acad. Sci. U. S. A.* **1998**, *95* (13), 7293–7298.
- (159) Inocencio, N. M.; Moehring, J. M.; Moehring, T. J. Furin activates Pseudomonas exotoxin A by specific cleavage in vivo and in vitro. *J. Biol. Chem.* **1994**, *269* (50), 31831–31835.
- (160) Abrami, L.; Fivaz, M.; Decroly, E.; Seidah, N. G.; Jean, F.; Thomas, G.; Leppla, S. H.; Buckley, J. T.; van der Goot, F. G. The pore-forming toxin proaerolysin is activated by furin. *J. Biol. Chem.* **1998**, *273* (49), 32656–32661.
- (161) Gordon, V. M.; Benz, R.; Fujii, K.; Leppla, S. H.; Tweten, R. K. Clostridium septicum alpha-toxin is proteolytically activated by furin. *Infect. Immun.* **1997**, *65* (10), 4130–4134.
- (162) Tian, S.; Huang, Q.; Fang, Y.; Wu, J. FurinDB: A database of 20-residue furin cleavage site motifs, substrates and their associated drugs. *Int. J. Mol. Sci.* **2011**, *12* (2), 1060–1065.
- (163) Kang, T.; Zhao, Y. G.; Pei, D.; Sucic, J. F.; Sang, Q. X. Intracellular activation of human adamalysin 19/disintegrin and metalloproteinase 19 by furin occurs via one of the two consecutive recognition sites. *J. Biol. Chem.* **2002**, *277* (28), 25583–25591.
- (164) Kuno, K.; Terashima, Y.; Matsushima, K. ADAMTS-1 is an active metalloproteinase associated with the extracellular matrix. *J. Biol. Chem.* **1999**, *274* (26), 18821–18826.
- (165) Leighton, M.; Kadler, K. E. Paired basic/Furin-like proprotein convertase cleavage of Pro-BMP-1 in the trans-Golgi network. *J. Biol. Chem.* **2003**, *278* (20), 18478–18484.
- (166) Banyard, J.; Bao, L.; Zetter, B. R. Type XXIII collagen, a new transmembrane collagen identified in metastatic tumor cells. *J. Biol. Chem.* **2003**, *278* (23), 20989–20994.
- (167) Raghunath, M.; Putnam, E. A.; Ritty, T.; Hamstra, D.; Park, E. S.; Tschodrich-Rotter, M.; Peters, R.; Rehemtulla, A.; Milewicz, D. M. Carboxy-terminal conversion of profibrillin to fibrillin at a basic site by PACE/furin-like activity required for incorporation in the matrix. *J. Cell Sci.* **1999**, *112*, 1093–1100.
- (168) Lehmann, M.; Rigot, V.; Seidah, N. G.; Marvaldi, J.; Lissitzky, J. C. Lack of integrin alpha-chain endoproteolytic cleavage in furin-deficient human colon adenocarcinoma cells LoVo. *Biochem. J.* **1996**, *317* (3), 803–809.
- (169) Bergeron, E.; Basak, A.; Decroly, E.; Seidah, N. G. Processing of alpha4 integrin by the proprotein convertases: histidine at position P6 regulates cleavage. *Biochem. J.* **2003**, *373* (2), 475–484.
- (170) Lissitzky, J. C.; Luis, J.; Munzer, J. S.; Benjannet, S.; Parat, F.; Chretien, M.; Marvaldi, J.; Seidah, N. G. Endoproteolytic processing of integrin pro-alpha subunits involves the redundant function of furin and proprotein convertase (PC) 5A, but not paired basic amino acid converting enzyme (PACE) 4, PCSB or PC7. *Biochem. J.* **2000**, *346* (1), 133–138.
- (171) Denault, J. B.; Claing, A.; D'Orleans-Juste, P.; Sawamura, T.; Kido, T.; Masaki, T.; Leduc, R. Processing of proendothelin-1 by human furin convertase. *FEBS Lett.* **1995**, *362* (3), 276–280.
- (172) Blais, V.; Fugere, M.; Denault, J. B.; Klarskov, K.; Day, R.; Leduc, R. Processing of proendothelin-1 by members of the subtilisin-like pro-protein convertase family. *FEBS Lett.* **2002**, *524* (1–3), 43–48.
- (173) Dey, A.; Norrbom, C.; Zhu, X.; Stein, J.; Zhang, C.; Ueda, K.; Steiner, D. F. Furin and prohormone convertase 1/3 are major convertases in the processing of mouse pro-growth hormone-releasing hormone. *Endocrinology* **2004**, *145* (4), 1961–1971.
- (174) Duguay, S. J.; Milewski, W. M.; Young, B. D.; Nakayama, K.; Steiner, D. F. Processing of wild-type and mutant proinsulin-like growth factor-1A by subtilisin-related proprotein convertases. *J. Biol. Chem.* **1997**, *272* (10), 6663–6670.
- (175) Wu, C.; Wu, F.; Pan, J.; Morser, J.; Wu, Q. Furin-mediated processing of Pro-C-type natriuretic peptide. *J. Biol. Chem.* **2003**, *278* (28), 25847–25852.
- (176) Sawada, Y.; Suda, M.; Yokoyama, H.; Kanda, T.; Sakamaki, T.; Tanaka, S.; Nagai, R.; Abe, S.; Takeuchi, T. Stretch-induced hypertrophic growth of cardiocytes and processing of brain-type natriuretic peptide are controlled by proprotein-processing endoprotease furin. *J. Biol. Chem.* **1997**, *272* (33), 20545–20554.
- (177) Siegfried, G.; Khatib, A. M.; Benjannet, S.; Chretien, M.; Seidah, N. G. The proteolytic processing of pro-platelet-derived growth factor-A at RRKR(86) by members of the proprotein convertase family is functionally correlated to platelet-derived growth factor-A-induced functions and tumorigenicity. *Cancer Res.* **2003**, *63* (7), 1458–1463.
- (178) Leitlein, J.; Aulwurm, S.; Waltereit, R.; Naumann, U.; Wagenknecht, B.; Garten, W.; Weller, M.; Platten, M. Processing of immunosuppressive pro-TGF-beta 1,2 by human glioblastoma cells

- involves cytoplasmic and secreted furin-like proteases. *J. Immunol.* **2001**, *166* (12), 7238–7243.
- (179) Dubois, C. M.; Laprise, M. H.; Blanchette, F.; Gentry, L. E.; Leduc, R. Processing of transforming growth factor beta 1 precursor by human furin convertase. *J. Biol. Chem.* **1995**, *270* (18), 10618–10624.
- (180) Hendy, G. N.; Bennett, H. P.; Gibbs, B. F.; Lazure, C.; Day, R.; Seidah, N. G. Parathyroid hormone is preferentially cleaved to parathyroid hormone by the prohormone convertase furin. A mass spectrometric study. *J. Biol. Chem.* **1995**, *270* (16), 9517–9525.
- (181) McColl, B. K.; Paavonen, K.; Karnezis, T.; Harris, N. C.; Davydova, N.; Rothacker, J.; Nice, E. C.; Harder, K. W.; Roufail, S.; Hibbs, M. L.; Rogers, P. A.; Alitalo, K.; Stacker, S. A.; Achen, M. G. Proprotein convertases promote processing of VEGF-D, a critical step for binding the angiogenic receptor VEGFR-2. *FASEB J.* **2007**, *21* (4), 1088–1098.
- (182) Siegfried, G.; Basak, A.; Cromlish, J. A.; Benjannet, S.; Marcinkiewicz, J.; Chretien, M.; Seidah, N. G.; Khatib, A. M. The secretory proprotein convertases furin, PC5, and PC7 activate VEGF-C to induce tumorigenesis. *J. Clin. Invest.* **2003**, *111* (11), 1723–1732.
- (183) Misumi, Y.; Oda, K.; Fujiwara, T.; Takami, N.; Tashiro, K.; Ikehara, Y. Functional expression of furin demonstrating its intracellular localization and endoprotease activity for processing of proalbumin and complement pro-C3. *J. Biol. Chem.* **1991**, *266* (25), 16954–16959.
- (184) Wasley, L. C.; Rehemtulla, A.; Bristol, J. A.; Kaufman, R. J. PACE/furin can process the vitamin K-dependent pro-factor IX precursor within the secretory pathway. *J. Biol. Chem.* **1993**, *268* (12), 8458–8465.
- (185) Bendetowicz, A. V.; Morris, J. A.; Wise, R. J.; Gilbert, G. E.; Kaufman, R. J. Binding of factor VIII to von willebrand factor is enabled by cleavage of the von Willebrand factor propeptide and enhanced by formation of disulfide-linked multimers. *Blood* **1998**, *92* (2), 529–538.
- (186) Bravo, D. A.; Gleason, J. B.; Sanchez, R. I.; Roth, R. A.; Fuller, R. S. Accurate and efficient cleavage of the human insulin proreceptor by the human proprotein-processing protease furin. Characterization and kinetic parameters using the purified, secreted soluble protease expressed by a recombinant baculovirus. *J. Biol. Chem.* **1994**, *269* (41), 25830–25837.
- (187) Komada, M.; Hatsuzawa, K.; Shibamoto, S.; Ito, F.; Nakayama, K.; Kitamura, N. Proteolytic processing of the hepatocyte growth factor/scatter factor receptor by furin. *FEBS Lett.* **1993**, *328* (1–2), 25–29.
- (188) Logeat, F.; Bessia, C.; Brou, C.; LeBail, O.; Jarriault, S.; Seidah, N. G.; Israel, A. The Notch1 receptor is cleaved constitutively by a furin-like convertase. *Proc. Natl. Acad. Sci. U. S. A.* **1998**, *95* (14), 8108–8112.
- (189) Willnow, T. E.; Moehring, J. M.; Inocencio, N. M.; Moehring, T. J.; Herz, J. The low-density-lipoprotein receptor-related protein (LRP) is processed by furin in vivo and in vitro. *Biochem. J.* **1996**, *313* (1), 71–76.
- (190) Jaaks, P.; D'Alessandro, V.; Grob, N.; Buel, S.; Hajdin, K.; Schafer, B. W.; Bernasconi, M. The proprotein convertase furin contributes to rhabdomyosarcoma malignancy by promoting vascularization, migration and invasion. *PLoS One* **2016**, *11* (8), e0161396.
- (191) Jaaks, P.; Meier, G.; Alijaj, N.; Brack, E.; Bode, P.; Koscielniak, E.; Wachtel, M.; Schafer, B. W.; Bernasconi, M. The proprotein convertase furin is required to maintain viability of alveolar rhabdomyosarcoma cells. *Oncotarget* **2016**, *7* (47), 76743–76755.
- (192) Li, Y.; Chu, J.; Li, J.; Feng, W.; Yang, F.; Wang, Y.; Zhang, Y.; Sun, C.; Yang, M.; Vasilatos, S. N.; Huang, Y.; Fu, Z.; Yin, Y. Cancer/testis antigen-Plac1 promotes invasion and metastasis of breast cancer through Furin/NICD/PTEN signaling pathway. *Mol. Oncol.* **2018**, *12* (8), 1233–1248.
- (193) Remacle, A. G.; Shiryayev, S. A.; Oh, E. S.; Cieplak, P.; Srinivasan, A.; Wei, G.; Liddington, R. C.; Ratnikov, B. I.; Parent, A.; Desjardins, R.; Day, R.; Smith, J. W.; Lebl, M.; Strongin, A. Y. Substrate cleavage analysis of furin and related proprotein convertases. A comparative study. *J. Biol. Chem.* **2008**, *283* (30), 20897–20906.
- (194) Izidoro, M. A.; Gouvea, I. E.; Santos, J. A.; Assis, D. M.; Oliveira, V.; Judice, W. A.; Juliano, M. A.; Lindberg, I.; Juliano, L. A study of human furin specificity using synthetic peptides derived from natural substrates, and effects of potassium ions. *Arch. Biochem. Biophys.* **2009**, *487* (2), 105–114.
- (195) Shiryayev, S. A.; Chernov, A. V.; Golubkov, V. S.; Thomsen, E. R.; Chudin, E.; Chee, M. S.; Kozlov, I. A.; Strongin, A. Y.; Cieplak, P. High-resolution analysis and functional mapping of cleavage sites and substrate proteins of furin in the human proteome. *PLoS One* **2013**, *8* (1), e54290.
- (196) Rungrotmongkol, T.; Decha, P.; Sompornpisut, P.; Malaisree, M.; Intharathap, P.; Nunthaboot, N.; Udommaneethanakit, T.; Aruksakunwong, O.; Hannongbua, S. Combined QM/MM mechanistic study of the acylation process in furin complexed with the H5N1 avian influenza virus hemagglutinin's cleavage site. *Proteins: Struct. Funct. Genet.* **2009**, *76* (1), 62–71.
- (197) Klein, T.; Eckhard, U.; Dufour, A.; Solis, N.; Overall, C. M. Proteolytic cleavage-mechanisms, function, and "Omic" approaches for a near-ubiquitous posttranslational modification. *Chem. Rev.* **2018**, *118* (3), 1137–1168.
- (198) Hofer, F.; Kraml, J.; Kahler, U.; Kamenik, A. S.; Liedl, K. R. Catalytic Site  $pK_a$  values of aspartic, cysteine, and serine proteases: Constant pH MD simulations. *J. Chem. Inf. Model.* **2020**, *60* (6), 3030–3042.
- (199) Zhu, J.; Declercq, J.; Roucourt, B.; Ghassabeh, G. H.; Meulemans, S.; Kinne, J.; David, G.; Vermorken, A. J.; Van de Ven, W. J.; Lindberg, I.; Muyldermans, S.; Creemers, J. W. Generation and characterization of non-competitive furin-inhibiting nanobodies. *Biochem. J.* **2012**, *448* (1), 73–82.
- (200) Lewandowska-Goch, M. A.; Kwiatkowska, A.; Lepek, T.; Ly, K.; Navals, P.; Gagnon, H.; Dory, Y. L.; Prahl, A.; Day, R. Design and structure-activity relationship of a potent furin inhibitor derived from influenza hemagglutinin. *ACS Med. Chem. Lett.* **2021**, *12* (3), 365–372.
- (201) Cameron, A.; Appel, J.; Houghten, R. A.; Lindberg, I. Polyarginines are potent furin inhibitors. *J. Biol. Chem.* **2000**, *275* (47), 36741–36749.
- (202) Becker, G. L.; Harges, K.; Steinmetzer, T. New substrate analogue furin inhibitors derived from 4-amidinobenzylamide. *Bioorg. Med. Chem. Lett.* **2011**, *21* (16), 4695–4697.
- (203) Becker, G. L.; Sielaff, F.; Than, M. E.; Lindberg, I.; Routhier, S.; Day, R.; Lu, Y.; Garten, W.; Steinmetzer, T. Potent inhibitors of furin and furin-like proprotein convertases containing decarboxylated P1 arginine mimetics. *J. Med. Chem.* **2010**, *53* (3), 1067–1075.
- (204) Harges, K.; Ivanova, T.; Thaa, B.; McInerney, G. M.; Klok, T. I.; Sandvig, K.; Kunzel, S.; Lindberg, I.; Steinmetzer, T. Elongated and shortened peptidomimetic inhibitors of the proprotein convertase furin. *ChemMedChem* **2017**, *12* (8), 613–620.
- (205) Lam van, T. V.; Heindl, M. R.; Schlutt, C.; Bottcher-Friebertshauer, E.; Bartschlag, R.; Klebe, G.; Brandstetter, H.; Dahms, S. O.; Steinmetzer, T. The basicity makes the difference: Improved canavanine-derived inhibitors of the proprotein convertase furin. *ACS Med. Chem. Lett.* **2021**, *12* (3), 426–432.
- (206) Van Lam van, T.; Ivanova, T.; Harges, K.; Heindl, M. R.; Morty, R. E.; Bottcher-Friebertshauer, E.; Lindberg, I.; Than, M. E.; Dahms, S. O.; Steinmetzer, T. Design, synthesis, and characterization of macrocyclic inhibitors of the proprotein convertase furin. *ChemMedChem* **2019**, *14* (6), 673–685.
- (207) Kibirev, V.; Osadchuk, T.; Kozachenko, O.; Kholodovych, V.; Fedoryak, O.; Brovarets, V. Synthesis, biological evaluation and docking of novel bisamidinohydrazones as non-peptide inhibitors of furin. *Ukr. Biochem. J.* **2015**, *87*, 55–63.
- (208) Osadchuk, T.; Semyroz, A.; Shybyryn, O.; Kibirev, V. Synthesis and investigation of the derivatives of amidinohydrazone-lated aromatic compounds as furin inhibitors. *Ukr. Biochem. J.* **2017**, *89* (6), 3–12.

- (209) Sielaff, F.; Than, M. E.; Bevec, D.; Lindberg, I.; Steinmetzer, T. New furin inhibitors based on weakly basic amidinohydrazones. *Bioorg. Med. Chem. Lett.* **2011**, *21* (2), 836–840.
- (210) Couture, F.; Kwiatkowska, A.; Dory, Y. L.; Day, R. Therapeutic uses of furin and its inhibitors: a patent review. *Expert Opin. Ther. Pat.* **2015**, *25* (4), 379–396.
- (211) Osadchuk, T. V.; Shybyryn, O. V.; Kibirev, V. K. Chemical structure and properties of low-molecular furin inhibitors. *Ukr. Biochem. J.* **2016**, *88* (6), 5–25.
- (212) Harges, K.; Becker, G. L.; Lu, Y.; Dahms, S. O.; Kohler, S.; Beyer, W.; Sandvig, K.; Yamamoto, H.; Lindberg, I.; Walz, L.; von Messling, V.; Than, M. E.; Garten, W.; Steinmetzer, T. Novel furin inhibitors with potent anti-infectious activity. *ChemMedChem* **2015**, *10* (7), 1218–1231.
- (213) Ivanova, T.; Harges, K.; Kallis, S.; Dahms, S. O.; Than, M. E.; Kunzel, S.; Bottcher-Friebertshausen, E.; Lindberg, I.; Jiao, G. S.; Bartenschlager, R.; Steinmetzer, T. Optimization of substrate-analogue furin inhibitors. *ChemMedChem* **2017**, *12* (23), 1953–1968.
- (214) Dahms, S. O.; Harges, K.; Steinmetzer, T.; Than, M. E. X-ray structures of the proprotein convertase furin bound with substrate analogue inhibitors reveal substrate specificity determinants beyond the S4 pocket. *Biochemistry* **2018**, *57* (6), 925–934.
- (215) Kruger, N.; Sauder, C.; Huttel, S.; Papies, J.; Voigt, K.; Herrler, G.; Harges, K.; Steinmetzer, T.; Orvell, C.; Drexler, J. F.; Drost, C.; Rubin, S.; Muller, M. A.; Hoffmann, M. Entry, replication, immune evasion, and neurotoxicity of synthetically engineered bat-borne Mumps virus. *Cell Rep.* **2018**, *25* (2), 312–320.
- (216) Strongin, A.; Pellicchia, M.; Barile, E. Inhibitors of furin and other pro-protein convertases. US9266828B2, February 23, 2016.
- (217) Remacle, A. G.; Gawlik, K.; Golubkov, V. S.; Cadwell, G. W.; Liddington, R. C.; Cieplak, P.; Millis, S. Z.; Desjardins, R.; Routhier, S.; Yuan, X. W.; Neugebauer, W. A.; Day, R.; Strongin, A. Y. Selective and potent furin inhibitors protect cells from anthrax without significant toxicity. *Int. J. Biochem. Cell Biol.* **2010**, *42* (6), 987–995.
- (218) Gagnon, H.; Beauchemin, S.; Kwiatkowska, A.; Couture, F.; D'Anjou, F.; Levesque, C.; Dufour, F.; Desbiens, A. R.; Vaillancourt, R.; Bernard, S.; Desjardins, R.; Malouin, F.; Dory, Y. L.; Day, R. Optimization of furin inhibitors to protect against the activation of influenza hemagglutinin H5 and Shiga toxin. *J. Med. Chem.* **2014**, *57* (1), 29–41.
- (219) Day, R.; Neugebauer, W.; Dory, Y. Stable peptide-based furin inhibitors. US20150141324A1, May 21, 2015.
- (220) Meloni, B. Neuroprotective peptides. WO2015061856A1, May 7, 2015.
- (221) Bhattacharya, S. Treatment of fibrotic disorders. WO2017141032A1, August 24, 2017.
- (222) Ramos-Molina, B.; Lick, A. N.; Nasrolahi Shirazi, A.; Oh, D.; Tiwari, R.; El-Sayed, N. S.; Parang, K.; Lindberg, I. Cationic cell-penetrating peptides are potent furin inhibitors. *PLoS One* **2015**, *10* (6), e0130417.
- (223) Lepek, T.; Kwiatkowska, A.; Couture, F.; Ly, K.; Desjardins, R.; Dory, Y.; Prahl, A.; Day, R. Macrocyclization of a potent PACE4 inhibitor: Benefits and limitations. *Eur. J. Cell Biol.* **2017**, *96* (5), 476–485.
- (224) Fittler, H.; Depp, A.; Avrutina, O.; Dahms, S. O.; Than, M. E.; Empting, M.; Kolmar, H. Engineering a constrained peptidic scaffold towards potent and selective furin inhibitors. *ChemBioChem* **2015**, *16* (17), 2441–2444.
- (225) Dahms, S. O.; Creemers, J. W.; Schaub, Y.; Bourenkov, G. P.; Zogg, T.; Brandstetter, H.; Than, M. E. The structure of a furin-antibody complex explains non-competitive inhibition by steric exclusion of substrate conformers. *Sci. Rep.* **2016**, *6* (1), 34303.
- (226) Podsiadlo, P.; Komiyama, T.; Fuller, R. S.; Blum, O. Furin inhibition by compounds of copper and zinc. *J. Biol. Chem.* **2004**, *279* (35), 36219–36227.
- (227) Basak, A.; Cooper, S.; Roberge, A. G.; Banik, U. K.; Chretien, M.; Seidah, N. G. Inhibition of proprotein convertases-1, -7 and furin by diterpenes of *Andrographis paniculata* and their succinoyl esters. *Biochem. J.* **1999**, *338* (1), 107–113.
- (228) Ramos-Molina, B.; Lick, A. N.; Blanco, E. H.; Posada-Salgado, J. A.; Martinez-Mayorga, K.; Johnson, A. T.; Jiao, G. S.; Lindberg, I. Identification of potent and compartment-selective small molecule furin inhibitors using cell-based assays. *Biochem. Pharmacol.* **2015**, *96* (2), 107–118.
- (229) Dahms, S. O.; Jiao, G. S.; Than, M. E. Structural studies revealed active site distortions of human furin by a small molecule inhibitor. *ACS Chem. Biol.* **2017**, *12* (5), 1211–1216.
- (230) Jiao Guansheng, Z. C. A kind of symmetrical compound and its application containing amidino groups. CN109160888A, January 8, 2019.
- (231) Jiao Guansheng, Z. C. A kind of 2,5-double deoxidation strepto-amine derivative and its application. CN109111376A, January 1, 2019.
- (232) Wu, C.; Zheng, M.; Yang, Y.; Gu, X.; Yang, K.; Li, M.; Liu, Y.; Zhang, Q.; Zhang, P.; Wang, Y.; Wang, Q.; Xu, Y.; Zhou, Y.; Zhang, Y.; Chen, L.; Li, H. Furin: A potential therapeutic target for COVID-19. *iScience* **2020**, *23* (10), 101642.
- (233) Komiyama, T.; Coppola, J. M.; Larsen, M. J.; van Dort, M. E.; Ross, B. D.; Day, R.; Rehemtulla, A.; Fuller, R. S. Inhibition of furin/proprotein convertase-catalyzed surface and intracellular processing by small molecules. *J. Biol. Chem.* **2009**, *284* (23), 15729–15738.
- (234) Ulrich, P.; Cerami, A. Trypanocidal 1,3-arylene diketone bis(guanylylhydrazone)s. Structure-activity relationships among substituted and heterocyclic analogues. *J. Med. Chem.* **1984**, *27* (1), 35–40.
- (235) Axten, J. M.; Cheung, M.; Demartino, M. P.; Guan, H. A.; Hu, Y.; Miller, A. B.; Qin, D.; Wu, C.; Zhang, Z.; Lin, X. Furin inhibitors. WO2019215341A1, November 11, 2019.
- (236) Essalmani, R.; Jain, J.; Susan-Resiga, D.; Andréo, U.; Evagelidis, A.; Derbali, R. M.; Huynh, D. N.; Dallaire, F.; Laporte, M.; Delpal, A.; Sutto-Ortiz, P.; Coutard, B.; Mapa, C.; Wilcoxon, K.; Decroly, É.; Pham, T. N.; Cohen, É. A.; Seidah, N. G. Furin cleaves SARS-CoV-2 spike-glycoprotein at S1/S2 and S2' for viral fusion/entry: indirect role of TMPRSS2. *bioRxiv*, December 20, 2020, ver. 1. DOI: 10.1101/2020.12.18.423106.
- (237) Khatib, A.-M.; Mercedes, M.; Montesinos, T.; Soulet, F.; Evrard, S.; Siegfried, G.; Villoutreix, B. Use of sulconazole as a furin inhibitor. WO2020127059A1, June 25, 2020.
- (238) Watt, R. K.; Hancock, C.; Gross, A. Method and compositions for the treatment of anemia through the inhibition of furin. WO2017147078A1, August 31, 2017.
- (239) Kachaeva, M. V.; Pilyo, S. G.; Kornienko, A. M.; Prokopenko, V. M.; Zhirnov, V. V.; Prichard, M. N.; Keith, K. A.; Yang, G.; Wang, H.-K.; Banerjee, N. S.; et al. In vitro activity of novel 1, 3-oxazole derivatives against human papillomavirus. *Ibnosina J. Med. Biomed Sci.* **2017**, *9* (4), 111–118.
- (240) Oh, J.; Barve, M. A.; Tewari, D.; Chan, J. K.; Grosen, E.; Rocconi, R. P.; Stevens, E. E.; DeMars, L. R.; Ghamande, S. A.; Coleman, R. L.; Manning, L.; Wallraven, G.; Senzer, N. N.; Birkhofer, M.; Nemunaitis, J. J. Clinical trial in progress: A phase 3 study of maintenance bi-shRNA-furin/GM-CSF-expressing autologous tumor cell vaccine in women with stage IIIb-IV high-grade epithelial ovarian cancer. *J. Clin. Oncol.* **2017**, *35*, TP5604.